CHARLES UNIVERSITY IN PRAGUE
FACULTY OF MATHEMATICS AND PHYSICS

DOCTORAL THESIS

2012 ELISSEOS VERVENIOTIS

CHARLES UNIVERSITY IN PRAGUE
FACULTY OF MATHEMATICS AND PHYSICS

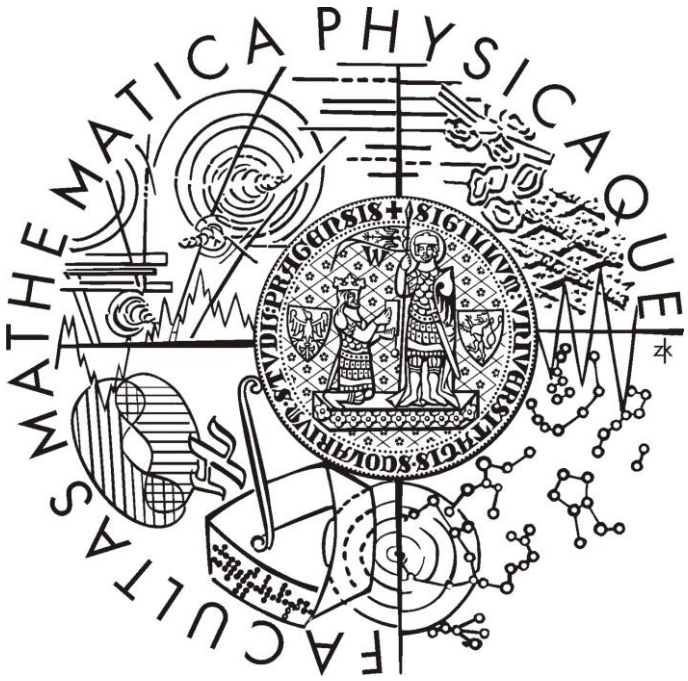

DOCTORAL THESIS

Structuring and study of electronic and chemical properties of semiconductor surfaces

Elisseos Verveniotis

Prague, 2012

Thesis submitted to Charles University as partial fulfilment for the degree of Doctor of Philosophy

Structuring and study of electronic and chemical properties of semiconductor surfaces

Supervisor:

Dr. Bohuslav Rezek

Institute of Physics, Academy of Science of the Czech Republic,

Cukrovarnická 10, 16253, Prague

Consultant:

Dr. Ivan Ošťádal

Department of plasma and surface physics, Faculty of Mathematics and Physics, Charles University, V Holešovičkách 2, 18200, Prague

Research was conducted at:

Institute of Physics, Academy of Science of the Czech Republic, Department of Thin Films and Nanostructures, Cukrovarnická 10, 16253, Prague

Opponents:

Dr. Petr Klapetek

Czech metrology institute,

Okružní 31, 63800, Brno

Dr. Miroslav Bartošík

Institute of physical engineering, Brno University of technology,

Technická 2896/2, 61669, Brno

Acknowledgements

I would like to thank my supervisor, Dr. Bohuslav Rezek for giving me the opportunity to participate in his projects. His immeasurable help, support and patience during the last four years made the completion of this thesis possible. He actively and efficiently tutored me in all aspects of my studies tirelessly, with a positive attitude and always with a smile.

I also feel the need to thank my colleagues in the Institute of Physics for all the research-related help and for making me feel at home from day one: Dr. Antonin Fejfar for providing necessary literature and allowing me to participate in the doctoral project, Dr. Alexander Kromka for consultation regarding CVD diamond, Mr. Oleg Babchenko, Ing. Marián Varga and Dr. Jiří Potměšil for diamond deposition, Dr. Jiří Stuchlík for silicon deposition, Dr. Jan Čermák for introduction to the SPM and optical lithography equipment, Dr. Emil Šípek for technical support with the nanocrystallization circuitry, Dr. Martin Ledinský and Dr. Tibor Ižák for Raman measurements, Dr. Aliaksei Vetushka for technical assistance with C-AFM and macroscopic electrical measurements, Dr. Egor Ukraintsev for AFM troubleshooting, Dr. Kateřina Kůsová for wet chemical etching, Dr. Karel Hruška, Dr. Zdeněk Výborný and Ing. Vlastimil Jurka for SEM and ellipsometry, Dr. Jitka Libertinová for SEM, Dr. Martin Ondráček for help with solid state theory, Ing. Martin Müller for profilometry and thermal evaporation, Dr. Zdeněk Remeš for FTIR and Mrs. Zdeňka Poláčková for diamond oxidation. Prof. Václáv Holý is acknowledged for his kind help with details of solid state physics and for including me in the special doctoral support project of Charles University. Special thanks go to Prof. Jan Kočka, the head of the Thin Films and Nanostructures department for his excellent ideas and insight concerning my work.

This work was financially supported by the research projects AV0Z10100521, KAN400100701 (AVČR), LC06040 (MŠMT), LC510 (MŠMT), P204/10/0212 (GAČR), P108/12/0996 (GAČR), P108/12/G108 (GAČR), doctoral projects 202/09/H041, SVV-2010-261307 and SVV-2011-263307, and the Fellowship J.E. Purkyně (AVČR). This work also occurred in frame of the LNSM infrastructure.

Several academic teachers from my early student years contributed significantly to my academic development and motivated me to pursue an academic career. I would like to mention Dr. George Adam of Technological Educational

Institute of Larissa, Greece for giving me the opportunity to spend a year abroad during my undergraduate studies. It was essentially the springboard for my international studies and for this I am very grateful. Prof. Martin Taylor and Dr. Julian Burt of Bangor University, Wales, UK are acknowledged for providing me with a solid background in Nanotechnology which was necessary for continuing my studies on the PhD level. Finally, I'd like to express my gratitude to my electronics tutor in secondary school, Mr. George Antonakopoulos (R.I.P.) for teaching me scientific thinking, a quality few teachers possess.

Last but not least I would like to thank my family: My mother, Mrs. Eleni Vervenioti for insisting on my postgraduate studies and supporting me through the years, my father Mr. Mihalis Verveniotis (R.I.P) for always doing his best and acting with my well-being in mind, and my life partner, Ms. Magda Urbanovská for being always there and believing in me. Without their never ending financial and, most importantly, emotional support I would have never made it that far. This work is dedicated to Dad who did not live long enough to see me graduate. You will be never forgotten.

Prague, December 2012

Abstract of thesis

Semiconductor materials play a crucial role in modern society as they have become integral parts of our daily life through personal computers, mobile phones, medical implants, solar panels and a plethora of other commercially available electronic devices. The semiconductor industry has been relying predominantly on silicon so far and will continue to do so for a few more years, until the material limits for miniaturization and device engineering are reached. Fortunately, worldwide research has already demonstrated that there are materials exhibiting superior mechanical, electronic, and optical properties and which can thus replace or at least complement silicon. This represents a very important step towards satisfying the ever rising global demand for smaller, faster, energy-efficient and cheaper electronic devices. To that end, nowadays research is focused on fabrication and characterization of diverse materials and nanostructures which are aimed to be integral in electronic devices. Due to the miniaturization, it is essential that the electronic, structural and chemical characterization and modification of those novel materials and structures is performed on the microscopic scale. The relatively young but nevertheless rapidly expanding and exciting field of nanoscience and nanotechnology has provided scientists with a wide range of appropriate instruments over the past few decades which are able to fulfil this need. In this work, we examine and modify in the nanoscale two application-relevant systems: 1) nanocrystalline diamond thin films and 2) hydrogenated amorphous silicon thin films.

We study nanocrystalline diamond as a relatively novel semiconducting material due to its unique combination of electronic, mechanical, thermal and optical properties. As recent developments have allowed the production of electronic grade synthetic diamond, prospects have opened for its utilization in real applications. We tailor the diamond deposition for production of thin films with the desired thickness, material purity and nanocrystal size. Characterization of the structural, chemical and electronic properties is performed mainly by scanning electron microscopy, micro-Raman spectroscopy and various scanning probe microscopy (SPM) techniques. The latter are also utilized for surface modification of the diamond. By that we resolve that the grain boundaries are predominantly responsible for 1) electronic transport and 2) electrostatic charging of oxidized diamond when the film is subjected to an external

electric field. In addition, we demonstrate that it is possible to self-assemble nanoparticles on such charged diamond surfaces if the stored charge in the diamond is enough to create potential contrast (and related electrostatic field) of at least ±1 V. We identify and explore the parameters that lead to effective electrostatic charging of diamond by close correlation of material properties (sp^2/sp^3 ratio) and experimental parameters (voltage, current, applied force, and material of SPM probes). These results have the potential to be utilized for self-assembly of hybrid nanodevices. Such devices can at the same time benefit from the unique properties of diamond.

The second system that was studied in this work is hydrogenated amorphous silicon. We apply atomic force microscopy to promote phase transition from amorphous to crystalline silicon and thus define micro- or nano-scopic crystalline features in the amorphous material. Development of such technology can be beneficial for fabrication of electronic or optical nanodevices that require precise positioning of nanocrystals. Such devices can also benefit from the usage of amorphous silicon substrate due to its easy and inexpensive fabrication when compared to silicon wafers. As another route we also demonstrate selective deposition of silicon nanocrystalites in pits of nanoscale dimensions which are created in the amorphous film by SPM.

We conclude this thesis with a chapter proposing combination of the two materials above. To that end we use the pits in the amorphous silicon films as templates for diamond deposition and we investigate the influence of the deposition parameters. We evidence selective growth of diamond nanocrystals with pronounced graphitic content within the pits. The progress reported here provides an important piece of knowledge for future research and applications of diamond and silicon nanostructures.

Abstrakt dizertace

Polovodičové materiály hrají velmi významnou roli v moderní společnosti, jelikož se staly nedílnou součástí našich každodenních životů prostřednictvím osobních počítačů, mobilních telefonů, lékařských implantátů, solárních panelů a spousty dalších elektronických přístrojů, které jsou komerčně dostupné. Polovodičový průmysl se zatím spoléhá hlavně na křemík a i v následujících několika letech v tom bude pokračovat, dokud nebudou dosaženy limity zmenšování velikosti a materiálového inženýrství obecně. Naštěstí se díky celosvětovému výzkumu podařilo ukázat, že existují materiály vykazující lepší mechanické, elektronické a optické vlastnosti, a které tak mohou nahradit nebo alespoň doplnit křemík. Toto představuje velice důležitý krok pro uspokojení stále rostoucí celosvětové poptávky po menších, rychlejších, energeticky výhodných a levnějších elektronických zařízeních. Z tohoto důvodu se současná věda zaměřuje na přípravu a charakterizaci různých materiálů a nanostruktur, které mají být začleněné do elektronických zařízení. Kvůli miniaturizace je kromě toho zásadní, aby elektronická, strukturální a chemická charakterizace a modifikace těchto nových materiálů a struktur byla provedena na mikroskopické úrovni. Relativně mladý, nicméně rychle se rozvíjející a velmi zajímavý obor nanověd a nanotechnologií naštěstí během posledních několika desetiletí poskytuje vědcům širokou škálu nástrojů schopných plnit tuto potřebu. V této práci zkoumáme a modifikujeme na mikroskopické úrovni dva aplikačně relevantní systémy 1) Tenké vrstvy nanokrystalického diamantu a 2) tenké vrstvy amorfního hydrogenovaného křemíku.

Nanokrystalický diamant studujeme jako relativně nový polovodičový materiál kvůli jeho unikátní kombinaci elektronických, mechanických, tepelných a optických vlastností. Díky tomu, že nedávný rozvoj umožňuje produkci syntetického diamantu v elektronické kvalitě zařízení, otevírají se nové možnosti pro jeho využití v reálných aplikacích. Parametry depozice diamantu jsou upravovány pro přípravu tenkých vrstev v požadované tloušťce, čistotě materiálu a velikosti nanokrystalů. Charakterizace strukturálních, chemických a elektronických vlastností provádíme především rastovací elektronovou mikroskopií, mikro-Ramanovskou spektroskopií a nejrůznějšími technikami rastrovací hrotové mikroskopie (SPM). Poslední zmíněné techniky jsou také využívany k modifikaci povrchu diamantu. Tímto se nám podařilo

vysvětlit, že hranice zrn jsou převážně zodpovědné za 1) elektronický transport a 2) elektronické nabíjení oxidovaného diamantu, když je vrstva vystavena vnějšímu elektrickému poli. Navíc ukazujeme, že nanočástice se mohou samy uspořádávat na takto nabitých površích diamantu, jestliže náboj uložený v diamantu vytváří potenciálový kontrast (a s tím související elektrické pole) alespoň ±1 V. Identifikujeme a zkoumáme parametry, které vedou k efektivnímu elektrostatickému nabíjení diamantu korelací materiálových vlastností (sp^2/sp^3 poměr) a experimentálních parametrů (napětí, proud, použitá síla, a materiál SPM sondy). Tyto výsledky mají potenciál pro vytváření samouspořádávajících se hybridních nanosystémů. Taková zařízení mohou současně využít unikátních vlastností diamantu.

Druhý systém studovaný v této práci je amorfní hydrogenovaný křemík. Používáme mikroskopii atomárních sil za účelem podpory přeměny fáze z amorfního na krystalický křemík a tím definujeme mikro- a nanorozměrové krystalické útvary v amorfním materiálu. Rozvoj této technologie může být přínosný pro přípravu elektronických nebo optických zařízení, které vyžadují přesné umístění nanokrystalů. Tato zařízení mohou mít také prospěch z použití amorfních substrátů díky jejich snadné a nenákladné výrobě v porovnání s křemíkovými wafery. Jako další možnou cestu ukazujeme selektivní depozici křemíkových nanokrystalů v nanorozměrových prohlubních, které jsou vytvořeny v amorfní matrici pomocí SPM.

Tuto dizertaci uzavíráme kapitolou navrhující kombinaci dvou výše zmíněných materiálů. Za tímto účelem využíváme prohlubně ve vrstvách amorfního křemíku jako šablony pro depozici diamantu a zkoumáme vliv depozičních parametrů. Prokázali jsme selektivní růst nanokrystalů diamantu s výrazným grafitickým obsahem uvnitř prohlubní. Ukazujeme, že lze dosáhnout a výsledky poskytují důležité poznatky pro budoucí výzkum a aplikace diamantoých a křemíkových nanostruktur.

Table of contents

1. Introduction 1

1.1 Semiconductor materials 3

1.1.1 Thin film Si and nanostructures 3

1.1.2 Thin film diamond and nanostructures 4

1.1.3 Combining diamond and silicon 5

1.2 Assembly of nanoparticles on surfaces 6

1.3 Aims of this work 6

2. Materials and Methods 9

2.1 Material deposition 9

2.1.1 Physical Vapor Deposition 9

2.1.1.1 Thermal evaporation 10

2.1.2 Chemical Vapor Deposition 10

2.1.2.1 Silicon thin film deposition 13

2.1.2.2 Diamond thin film deposition 14

2.1.3 Post-deposition surface treatment 18

2.1.3.1 Silicon oxide etching 18

2.1.3.2 Diamond surface termination 19

2.2 Material characterization 20

2.2.1 Macroscopic electrical current measurements 20

2.2.2 Advanced microscopy methods 21

2.2.2.1 Scanning Electron Microscopy 21

2.2.2.1.1 Electronic contrast in SEM 23

2.2.2.2 Scanning Probe Microscopy 24

2.2.2.2.1 Scanning Tunneling Microscopy 24

2.2.2.2.2 Atomic Force Microscopy 25

2.2.2.2.3 Conductive Atomic Force Microscopy 27

2.2.2.2.4 Kelvin Force Microscopy 28

2.2.2.2.5 AFM-aided surface modifications 29

2.2.3 Raman scattering 32

2.2.3.1 Microscopic Raman spectra and maps 33

3. Results and Discussion 35

3.1 Local diamond charging 35

3.1.1 NCD deposited on silicon 35

3.1.2 Chemical composition of NCD and its impact to charging 41

3.1.3 Electrostatically-guided assembly of nanoparticles on NCD 47

3.1.4 Detailed study of NCD electronic properties in the nanoscale 54

3.1.5 Charging NCD by constant current application 60

3.2 Nanocrystallization of a-Si:H 71

3.2.1 FE-MISPC of a-Si:H with improved current control 71

3.2.2 Effect of secondary silicon deposition on FE-MISPC pits 79

3.3 Combination of diamond nanocrystals with a-Si:H 90

3.3.1 Nucleation and growth of NCD on a-Si 90

3.3.2 Selective growth of diamond nanocrystals 93

4. Conclusions 98

Bibliography 101

About the Author *107*

Curriculum Vitae **107**

List of publications and conference contributions **108**

Peer-reviewed scientific journals 108

Conference contributions 109

1. Introduction

Nearly two centuries have passed since the discovery of silicon by Jöns Jacob Berzelius [1] and the first documented observation of a semiconductor effect by Michael Faraday [2, 3]. Since then, semiconductor technology did several technological leaps to become the ever evolving and rapidly changing field we know today. Several milestone discoveries contributed to this evolution. While stating all of them would be out of scope for this work, it is worthwhile to mention the few that pioneered the technological progress in semiconductor physics.

First silicon-based p-n junction

Russel Ohl accidentally fabricated the first solid-state, silicon-based p-n junction while experimenting for improving the purity of his material [1]. When he shone light on the junction, he observed the presence of a field across it. This represented the first silicon solar cell.

Figure 1.1 The first transistor. Image courtesy of Bell Labs.

Invention of the transistor

William Shockley, John Bardeen and Walter Brattain of Bell labs fabricated the first transistor [1]. It was a Germanium-based, point-contact device (Figure 1.1).

They showed that the transistor was amplifying the input signal, thus resulting in power gain. The team won the 1956 Nobel Prize in Physics for this invention.

The Integrated Circuit (IC)

Jack Kilby created the first IC on Germanium. It contained transistors, resistors and capacitors [4]. This groundbreaking achievement allowed the fabrication of all the components by a single material. Robert Noyce (co-founder of Intel) developed independently a half year later his silicon-based IC where he formed all the components together on a silicon chip [1].

Semiconductor-based electronics have evolved greatly since those milestone inventions. They enabled the fabrication of a plethora of commercial devices such as personal computers (PC), mobile phones, medical implants and photovoltaic solar cells which are used by billions of people worldwide on a daily basis.

The constant need for smaller and more efficient devices is addressed by miniaturization of the feature size on IC's. Modern PC processors are built with the 22 nm method, allowing the presence of billions of transistors within areas of a few tens of mm^2. While continuous miniaturization provides significant power boosts to the devices of every new generation, it also has some drawbacks and unwanted side effects.

First of all as the theoretical limit of silicon miniaturization draws near, the industry will have to devise other methods or use novel materials which will allow the continuation of the development trends. As transistors get smaller, ways to limit the resulting increase of the current density must be devised to avoid factors that endanger the device integrity such as electromigration [5].

In addition, in these small sizes, quantum mechanical effects start to play a role [6, 7]. Some quantum-related issues with gate current leakage had to be resolved already in the current generation. They were overcome by replacing the silicon oxide with different compounds of higher dielectric strength [8].

Furthermore, high integration and dense packing of many electronic components call for faster, more efficient cooling of the IC. Lack of proper dissipation of the excess heat was the reason for various temperature-related failures of Pentium 4 chips during the last decade [5]. Now the issue is addressed by flip-chip [9] and silicon-on-diamond (SOD) technologies.

There are thus many difficulties and corresponding technological as well as scientific challenges arising from the current trends in semiconductor technology forward. Since the global interest and thus market for consumer electronics, photovoltaics, sophisticated medical devices etc. constantly expand, new technologies and new materials have to be used (or combined with the available ones) in order to preserve the growth of this exciting field and satisfy the needs and demands of modern society.

1.1 Semiconductor materials

Applications involving semiconductors are clearly still dominated by silicon. However, there is an emerging trend for the use of diverse novel materials whose electronic, thermal and optical properties are superior or complementary to silicon. Present examples would be graphene and diamond which are both carbon-based.

Introduction of new materials for nanoelectronics generates the need for detailed characterization of their properties in the appropriate nano- or micro-scale. Resolving their structural, electronic and chemical properties is a prerequisite to actual device fabrication. Such characterization is important since it provides valuable information concerning the strengths and weaknesses of a material, which ultimately leads to the decision if it is appropriate for a particular application. Typically, the material of choice is deposited in the form of a thin film and characterized by various methods able to provide nanoscale resolution (e.g. Atomic Force Microscopy-AFM). In this work the employed materials are silicon and diamond.

1.1.1 Thin film Si and nanostructures

Silicon thin films are usually deposited by Chemical or Physical Vapor Deposition techniques (CVD or PVD). Nature of the produced thin films depends on the deposition parameters [10-12]. It is thus possible to grow amorphous, polycrystalline or mixed-phase films with control over the crystal size and density. Tailoring properties of the deposited material is important since it gives the possibility for targeted, application-specific silicon growth.

Silicon can be grown as a uniform, continuous thin film, but it can also be deposited or processed in the form of nanoribbons/nanowires [14, 15] on diverse substrates [16-18]. Figure 1.2 shows such nanowires (a) as well as a mixed-phase silicon film (b). Those structures can be used then for actual applications, such as microscopic Field Effect Transistors (FET) [19].

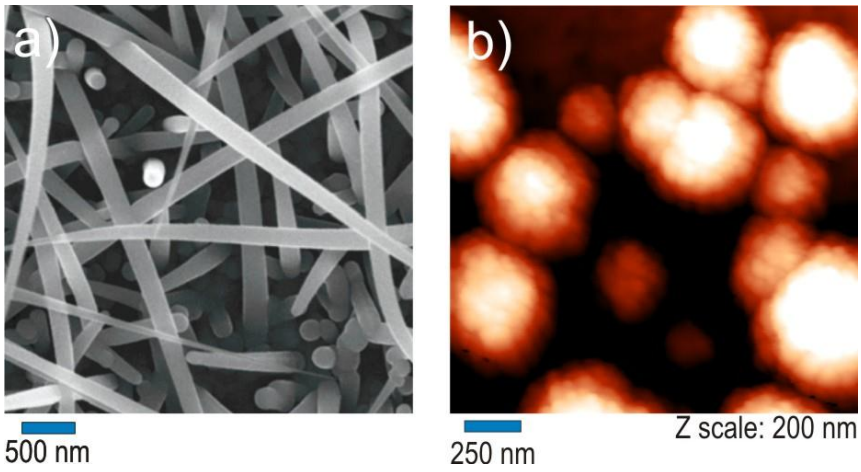

Figure 1.2 (a) Scanning electron microscope micrograph of silicon nanorods grown on glass and (b) detailed AFM topography showing a mixed-phase Si thin film grown on glass. Images after Červenka et al. [14] and Ledinský et al. [20] respectively.

1.1.2 Thin film diamond and nanostructures

Rarity and thus high cost of electronic grade diamond (mostly natural, clear diamond) prevented its extensive research until recently. However, nowadays it is possible to grow synthetic high quality diamond by CVD, which opens perspectives for taking advantage of its unique set of properties for electronic-related applications [21].

From the electronic point of view, diamond is a wide band gap semiconductor (5.5 eV). It can be transformed into p- or n-type semiconductor by boron [22] or phosphorus [23] doping, respectively. Intrinsic diamond is thus generally electrically insulating and transparent for visible light. Furthermore, its thermal conductivity [24] is unrivalled by any known material and, in addition, it is also bio-compatible which makes it ideal for bio-applications [25-27].

Deposition of diamond in nanocrystalline form (NCD) has already been demonstrated on a wide range of substrates such as silicon, polymers, and glass [28]. As the CVD process enables control over the deposition conditions, we can manipulate the resulting film thickness, grain size and chemical composition (thus electronic properties) of the diamond. An example of CVD diamond thin film AFM topography and local current map (measured by Conductive AFM – C-AFM) is illustrated in Figure 1.3 (a, b).

Diamond can be also grown or manipulated selectively. For example, by employing photo- or e-beam lithographic techniques it is possible to create diamond structures such as microchannels [29], nanochannels [30, 31], in-plane transistors [32, 33] and nanoelectronic device components [34] at will. A diamond 470 nm wide nanochannel grown on Si/SiO_2 substrate can be seen in Figure 1.3 (c).

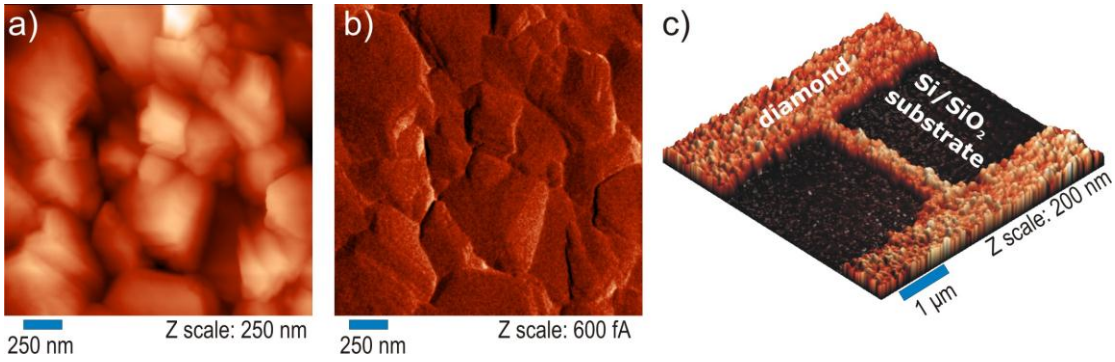

Figure 1.3 (a) AFM topography and (b) corresponding C-AFM current map (sensing bias voltage = 50 V) of an oxidized NCD film deposited on p-doped silicon wafer. (c) AFM topography of a directly grown diamond nanochannel on Si/SiO_2 substrate after Babchenko et.al. [30].

1.1.3 Combining diamond and silicon

Diamond is generally combined with silicon in order to address the various thermal limitations of the latter in device fabrication [35]. As discussed above, silicon is a poor thermal conductor when compared to diamond. Moreover, the buried oxide that is used in a range of silicon-based applications limits heat conduction. Hence, implementing diamond can greatly benefit silicon nanodevices in terms of heat

dissipation and thus drastically improve their reliability. This concept has already been adopted in electronic industry, for instance by Intel [36].

1.2 Assembly of nanoparticles on surfaces

The constant necessity for device miniaturization calls for new technologies able to fulfil the industry needs while keeping the production cost on reasonable levels. This necessity is becoming more evident as the classic photolithography-based miniaturization approach has been almost driven to its limits.

One promising alternative method able to provide assembled nanostructures in the sub-100 nm scale is the organization of atoms and molecules (either organic, inorganic, polymers, bio-molecules), which effectively form nanoparticles, on diverse surfaces [37]. This assembly initially involved organic molecules transferred or chemisorbed on solid substrates. Typical examples would be alcanethiolates forming self-assembled monolayers on gold surfaces [38] or amphiphilic molecules deposited on some solvent as Langmuir-Blodgett films [39].

Besides the above well-known molecular self-organization processes, it is possible to assemble biological components (proteins, cells) [27] or nanoparticles [40-42] on chemically or electrically functionalized surfaces. In those cases the substrate is treated in order to attract or repel the to-be-deposited compound. That way it is possible to create patterns of desired geometry which will be either covered by or completely free of nanoparticles. For example, charging the substrate prior its exposition to the nanoparticles enables self-assembly by electrostatic attraction/repulsion [41, 42]. Such methodology is promising for combined silicon/diamond nanosystems where silicon nanopaticles or nanocrystals would be self-assembled on diamond surfaces in order to create, for instance, microscopic opto-electronic devices [43].

1.3 Aims of this work

Merging different semiconductor materials represents an important and up-to-date step in development of new applications and devices in nanoelectronics. Small

size enables higher sensitivity, portability and hence broader availability of such devices. Moreover, qualitatively new electronic and optical phenomena appear in small dimensions, which ultimately affect the macroscopic device behaviour. Fabrication of such miniature structures with well-defined placement and arrangement is still a challenging task despite the long-term and worldwide effort and progress.

For instance, silicon nanostructures and nanocrystals are important for optoelectronic, nanoelectronic and biological applications [44]. Therefore, precise positioning of such nanomaterials opens prospects for various applications. In addition, usage of diverse materials such as diamond for selective growth in nanoscale templates can create well-ordered, hybrid structures whose importance is constantly increasing for today's nanoelectronic industry as discussed above. On the other hand, self-assembly of nanoparticles and other nanomaterials on diamond thin films could be beneficial for creating complex nano-devices or nano-systems that exploit the unique set of diamond properties.

Therefore, this work aims at characterization and control of local (down to nanometer level) structural, electronic and chemical properties of silicon and diamond. Before proceeding to the fabrication of an actual nanodevice, the behaviour of the materials employed is thoroughly investigated in the appropriate nano- or micro-scale. Detailed knowledge of the material properties is crucial for their further optimization and, ultimately, manipulation in order to use them as functional interfaces for guided assembly, selective deposition or other applications. For these tasks, we optimize our materials by CVD growth targeted towards specific structural, electronic and chemical properties which are then observed by Scanning Elecrton Microscopy (SEM), Raman spectroscopy and a wide range of advanced scanning probe methods such as Kelvin Force Microscopy (KFM) and C-AFM.

As regards material modifications, amorphous silicon films are subjected in AFM to electric field in order to produce nanoscopic, well-ordered arrays of pits. These pits can consist of either crystalline or amorphous silicon. The altered interface can then be used as template for a secondary deposition of silicon or diamond nanocrystals inside the pits. Similarly, NCD thin films are charged locally by biased AFM probes. The resulting charged micro-patterns are persistent and can be used for nanoparticle assembly by electrostatic attraction/repulsion.

Improvement of nanocrystal positioning in amorphous silicon, self-assembly of nanostructures on diamond substrates, understanding the electronic properties of

nanocrystalline diamond and, ultimately, formation of hybrid silicon/diamond systems thus became major accomplishments of this study. The progress done may be beneficial for a wide range of fields related to natural sciences.

2. Materials and Methods

In this section we describe the experimental methods that were used to fabricate, functionalize and characterize the materials, interfaces and nanostructures studied in this work.

2.1 Material deposition

There is a wide range of options offered to scientists and engineers when it comes to thin film deposition. Many new methods were introduced and developed in the course of the last century [1]. Each has its advantages and disadvantages. The method of choice always depends on the intended application (thus the nature and purity of the resulting material a particular method offers) and of course on the available budget. All deposition methods are roughly divided in two categories: CVD and PVD. In this work we used CVD variants for silicon and diamond deposition. Thermal evaporation, which falls under PVD, was implemented for deposition of metal layers.

2.1.1 Physical Vapor Deposition

This method enables the deposition of thin films via transfer of material vapor on a substrate. The vapor can be produced from materials in the solid, liquid or gas phase. In contrast to CVD, there are no chemical reactions between growth precursors involved in the process. PVD can be used for deposition of diverse materials (metals, semiconductors, ceramics etc.).

The most common PVD methods are thermal evaporation and sputtering. While sputtering is mostly used in VLSI fabrication due to its superior results in terms of deposited film structure and homogeneity, thermal evaporation is still being employed for various semiconductor and laboratory applications. Choosing which technique to follow depends on various factors such as:

- what kind of material needs to be deposited
- physical properties of the substrate (shape, temperature tolerance etc.)
- homogeneity of the final product
- deposition rate

In this work we used thermal evaporation for deposition of metal films (Ti/Ni) on corning glass substrates before silicon CVD. We preferred evaporation because it is faster and inexpensive compared to sputtering and the resulting film quality is good enough for our purposes. Titanium was used as an interlayer between Ni and the glass for improved adhesion. Those thin films were used as bottom electrodes.

2.1.1.1 Thermal evaporation

Thermal evaporation is based on heating (by e-beam or resistive means) of the target solid material to be sublimed or melted and evaporated. In this work we used resistive heating for evaporation. The material to be evaporated is put in a container (boat) made of a highly refractory metal (tungsten in our case) which is heated by a high electrical current that flows through it [1]. When the temperature is high enough, the target material melts and starts evaporating to the top of the evaporation chamber, effectively introducing the vapor on the substrates. The thickness of the film can be constantly monitored by a Quartz Crystal Microbalance (QCM) sensor, giving a fairly good control over the deposited thickness and deposition rate. Presence of high vacuum is mandatory. The presence of oxygen in the chamber could lead to oxidation and deposition of contaminating layers on the substrates.

In our case, we deposited Ti (melting point 1668 ^{o}C) by heating the tungsten boat with a current of 250 A. Nickel on the other hand has a lower melting point (1455 ^{o}C) and thus requires lower current in order to be melted and evaporated (187 A). Typical metal deposition rates in this work were in the order of 4 Å /sec.

2.1.2 Chemical Vapor Deposition

Chemical vapor deposition is based on the growth of a solid material via chemical reaction of precursors in the gas phase and on the substrate. It typically

employs a chamber which is connected to inlets of the various gases that will take part in the process. The desired substrate temperature is achieved by placing it on a heater. When the CVD reaction chamber establishes the target pressure (for example by a vacuum pump in Low-Pressure CVD) the gas flow is initiated and the material starts growing on the substrate. The chemistry that promotes CVD growth is quite rich as deposition can be promoted by pyrolysis (typical for Si growth), reduction, oxidation, disproportionation etc. [45].

There are two types of reactions that take place during CVD deposition: surface (heterogeneous) and gas phase (homogeneous). The latter should always be preferred and the contribution of the former minimized if the desired result is homogeneous, good quality thin film. This can be controlled by adjusting the reactant concentration. The higher the concentration the less heterogeneous nucleation occurs. However, re-nucleation can be enhanced, too.

The possibility of introducing various reactants into the CVD chamber enables better control over the resulting material. This influences the structure and composition of the produced films (crystalline, amorphous) as well as possible doping type and dopant concentration. In Figure 2.1 we can see the relation between temperatures, deposition rate and growth type for CVD silicon.

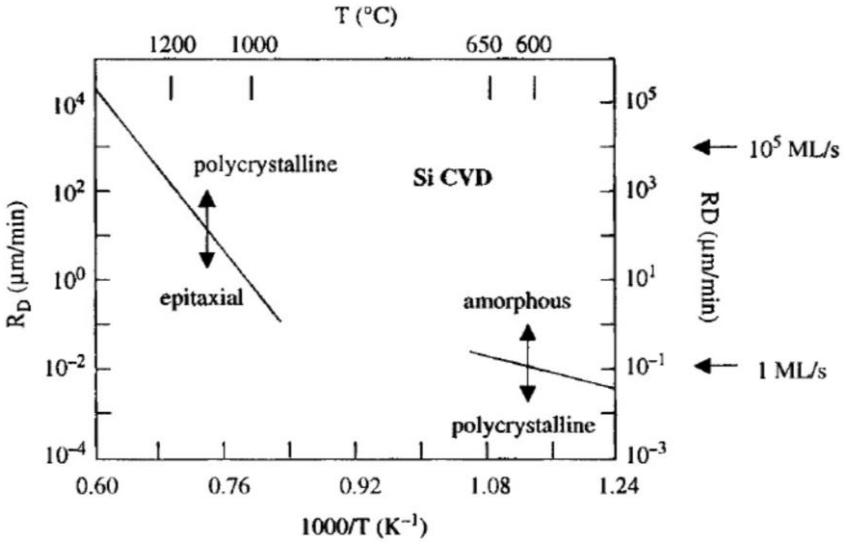

Figure 2.1 Relation between temperature, deposition rate and growth type for CVD Si. Graph after J. Bloem et al. [46].

The CVD reactions need energy to be activated. This energy is usually supplied via elevation of the substrate temperature or by hot filament (pyrolysis). However, this is not always convenient. For example, when the substrate is thermally sensitive and its properties change with temperature. For these cases modified CVD methods, such as Plasma Enhanced CVD (PE-CVD) and Laser Enhanced CVD, are preferred. A comparison between PE-CVD and Low-Pressure CVD (LP-CVD) for polysilicon growth can be seen in Figure 2.2. It is clear that the latter is effective only for higher temperatures as its deposition rate drops significantly under the 700 ^{o}C threshold. On the contrary, PE-CVD yields satisfactory deposition rates even at lower temperatures due to the presence of plasma which provides the system with necessary energy for the chemical reactions.

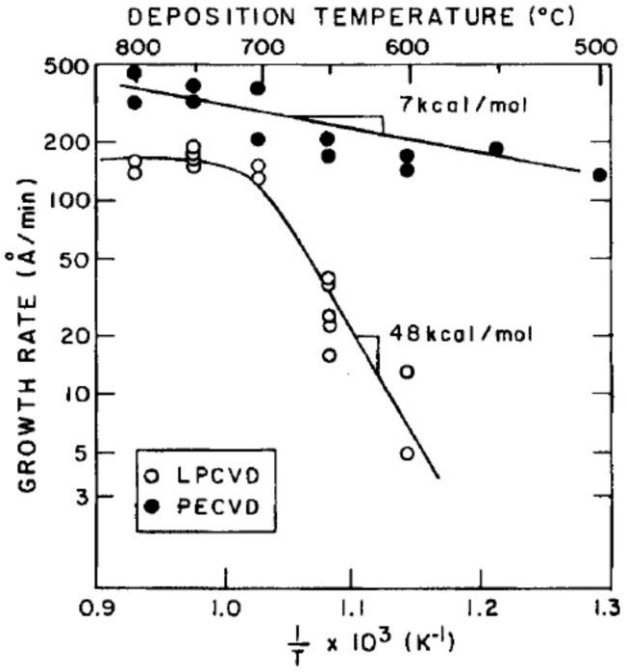

Figure 2.2 Deposition temperatures vs. growth rate for LP- and PE-CVD. Graph after J.J. Hajjar et al [47].

CVD methods are classified depending on the compounds used for the reactions (e.g. metal-organic CVD), the atmospheric conditions in which it is conducted (e.g. LP-CVD) and the presence or not of plasma (PE-CVD). Method of choice depends on the target material since with CVD allows the deposition of metals (e.g. Ti, Al, W), semiconductors (e.g. Si, Ge, GaAs) and insulators (e.g. SiO, AlO).

We employed CVD for depositing both silicon and diamond due to its various advantages. This method is well documented in the literature [48-50], gives us reasonably good control over the final result (thin film) by adjusting the deposition parameters, and enables deposition on temperature-sensitive substrates. The specific growth conditions need to be optimized, though, to achieve the desired target material and properties.

2.1.2.1 Silicon thin film deposition

For the purpose of this work we grew amorphous and mixed-phase (amorphous/crystalline) silicon thin films. Both types were deposited by RF-CVD (plasma excited by radio frequency) and employing silane decomposition. In addition, our films are hydrogenated, which is necessary for the purpose of this study as we will discuss in Chapter 3. Generally, hydrogen passivates dangling bonds on the surface and in the bulk, stabilizing the material [51, 52]. However, hydrogenation can also cause sample degradation by light [53] but this is not an issue for our work.

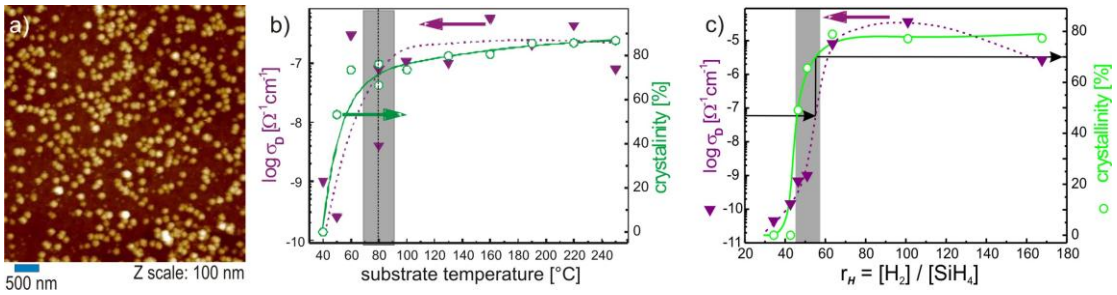

Figure 2.3 (a) AFM topography of mixed-phase silicon thin film grown on Ni/Ti/glass substrate by CVD. (b, c) Dependence of produced silicon thin film crystallinity/conductivity to (b) substrate temperature and (c) silane dilution. Graphs after Kocka et. al. [12].

The a-Si:H films were deposited in the thickness of 170-400nm (± 30 nm, measured by a stylus profilometer) on a Corning 7059 glass substrate coated with 40 nm thin nickel film and 10 nm titanium interlayer for improved adhesion to glass. The metals are deposited by thermal evaporation. Substrate temperature of 50^{o}C (note the

temperature difference compared to CVD without plasma as illustrated in Figure 2.1) and 0.02% dilution of SiH_4 in helium result in a hydrogen content of 20–45 at.% in the films [54].

Mixed-phase silicon thin films are deposited using the same process by increasing the deposition temperature to 100^{o}C while keeping all the other parameters identical. The elevated temperature enables deposition of a film at the border of amorphous and crystalline silicon growth [12]. It results in a continuous a-Si:H layer with several scattered silicon micro- or nano-crystals as shown in Figure 2.3 (a). Altering the temperature or Si_4H_2 dilution shifts the nature of the deposited layer towards amorphous (lower T, lower r_h) or polycrystalline (higher T, higher r_h), as shown in Figure 2.3 (b, c).

2.1.2.2 Diamond thin film deposition

Diamond in this study was also deposited by PE-CVD but this time the plasma was excited by microwaves. Microwave plasma is more efficient for molecular deionization-dissociation than RF plasma. This makes the actual deposition more efficient due to the better gas decomposition [55]. Schemes of the two different reactors used for the diamond growth are illustrated in Figure 2.4 (a, b). The distinctive difference between them is the geometry of the produced plasma: in the AIXTRON [56] reactor the plasma is confined in the close proximity of the substrate (focused plasma), while in the Roth and Rau reactor [57] the plasma is distributed all over the reactor with its intensity declining as we move farther from the antenna (linear plasma). It is possible to produce high quality, continuous diamond films with both setups [28, 58].

There are two routes of substrate preparation for diamond growth by PE-CVD. In the first, the substrate is exposed to the growth precursors "as is", without any surface pre-treatment, thus allowing the growth species to be deposited spontaneously. The second involves substrate pre-nucleation. This was achieved in our case by ultrasonication in a solution containing diamond nanopowder. During CVD the diamond growth occurs predominantly on the diamond nanoparticles already present on the substrate.

A variety of different gases can be used for diamond deposition. What is typically needed is a carbon source (for diamond growth) diluted in etch agents (for selectivity of sp^2 to sp^3 carbon etching). In this work we used methane as primary carbon source, hydrogen as the main etchant and carbon dioxide as secondary etchant and carbon source. During the deposition process the CH_4 is reduced, losing gradually its H, effectively forming carbon bonds. By this process we create both sp^3 (diamond) and sp^2 (graphite) carbon bonds. However, as the target material is diamond and not graphite, there is the need to etch any sp^2 bonded carbon. Hydrogen etches away both sp^2 and sp^3 phase. Nevertheless, the etch rate of sp^2 is almost ten times larger than the corresponding sp^3 etch rate [59]. Thus, proper tuning of deposition parameters can result in thin films with predominant diamond character. CO_2 acts primarily as an etchant (oxygen) with simultaneous donation of its carbon atom to the diamond growth. It is preferred than pure oxygen to avoid the possible exothermic reaction (explosion) due to combination with H in high temperature environment.

Diamond growth requires careful selection of deposition parameters. Those are mainly concentration of the carbon source gas, pressure and temperature. By manipulating them we can tailor the resulting chemical composition of the films. Impact of each of those parameters to the deposition is as follows:

- Increasing the deposition temperature increases the reactions on the substrate, causing the growth precursors to deposit faster. This benefit is countered by the fact that diamond deposited at higher temperatures can be of inferior quality due to oversaturation of sp^2 phase deposition. However, this behaviour applies mostly to pre-nucleated samples. In untreated substrates the more energetic etchant (H) removes faster the structures formed in the very first growth steps. Such behaviour reduces spontaneous nucleation and thus affects the deposited diamond crystal density on the substrate.
- Methane concentration must be kept reasonably low (usually <5%) in order to ensure diamond growth. Increasing the concentration of CH_4 increases the amount of available growth species, while reducing the relative concentration of the primary etching agent (H). This will result in more sp^2 bonded carbon in the film since the available hydrogen will not be enough to etch the unwanted non-diamond carbon fast enough.

- Pressure is proportional to the plasma density. Therefore, by increasing the pressure we increase the physical amount of growth precursors as well as H in the system. This results in somewhat faster deposition with side effects similar, but less pronounced, to the ones discussed above for the temperature.

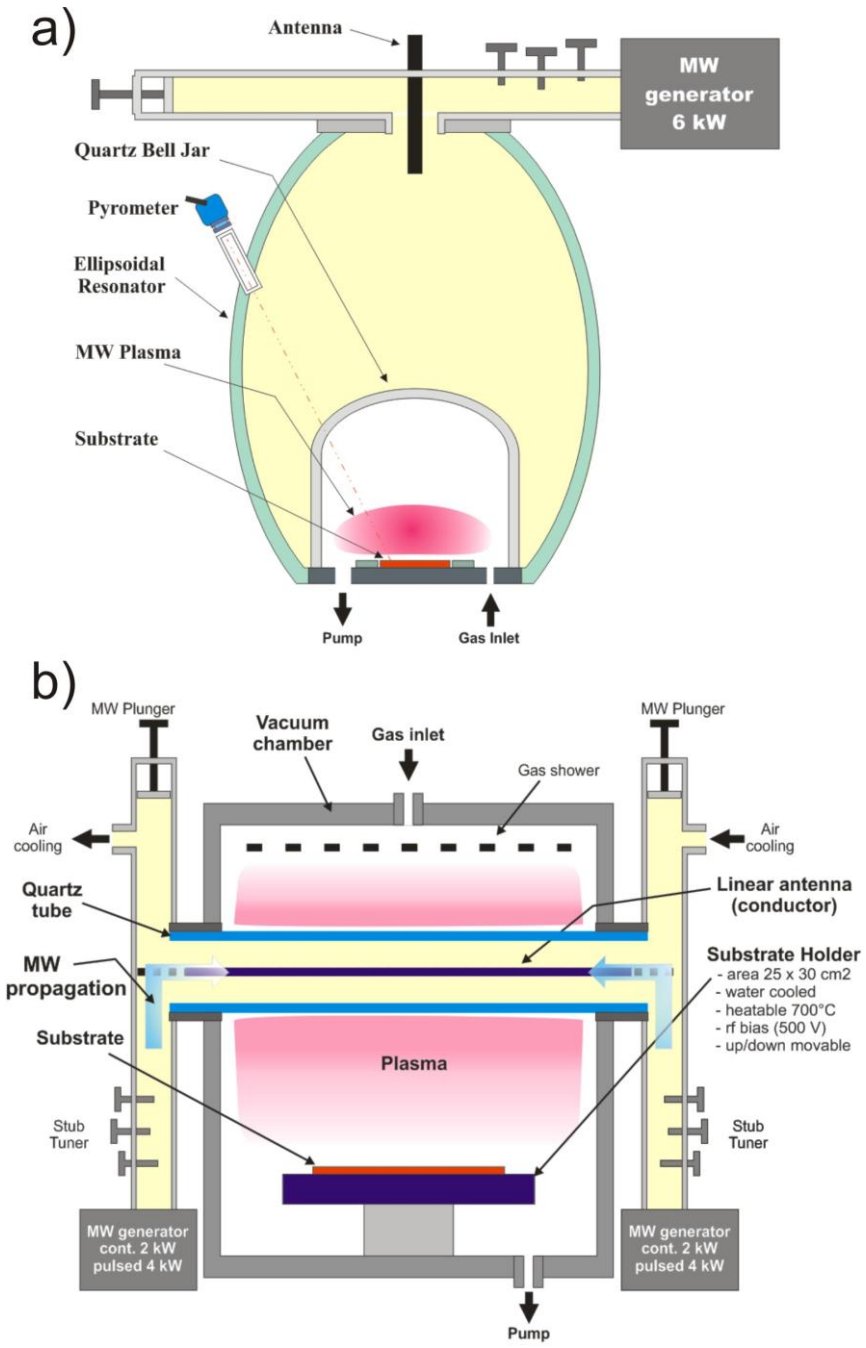

Figure 2.4 CVD reactors used for NCD deposition utilizing (a) focussed and (b) linear plasma. Images after [60] and [58].

For the NCD films grown in the focussed plasma reactor, microwave plasma power was 900W and CH_4:H_2 dilution 3:300 sccm. Deposition temperature was ranging between 420 ^oC and 820 ^oC. The substrates were conductive, p-doped silicon wafers nucleated by water-dispersed detonation diamond powder of 5 nm nominal particle size (NanoAmando, New Metals and Chemicals Corp. Ltd.) using an ultrasonic treatment for 40 min. Typical examples of NCD deposited by this methodology can be seen in the SEM micrographs in Figure 2.4. Sample in Figure 2.4 (a) was deposited at 420 ^oC for 8 hours while its Figure 2.4 (b) counterpart at 600 ^oC for 16 hours.

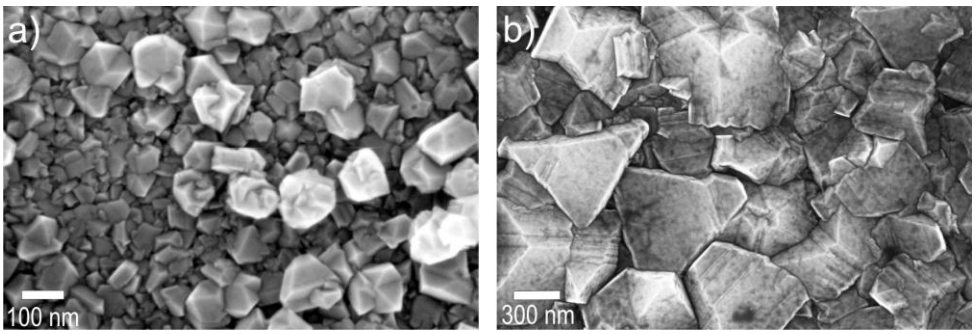

Figure 2.4 SEM micrographs of NCD thin films deposited on pre-nucleated, p-doped silicon wafer by CVD in the focussed plasma reactor. (a) At 420 ^oC for 8 hours and (b) at 600 ^oC for 16 hours.

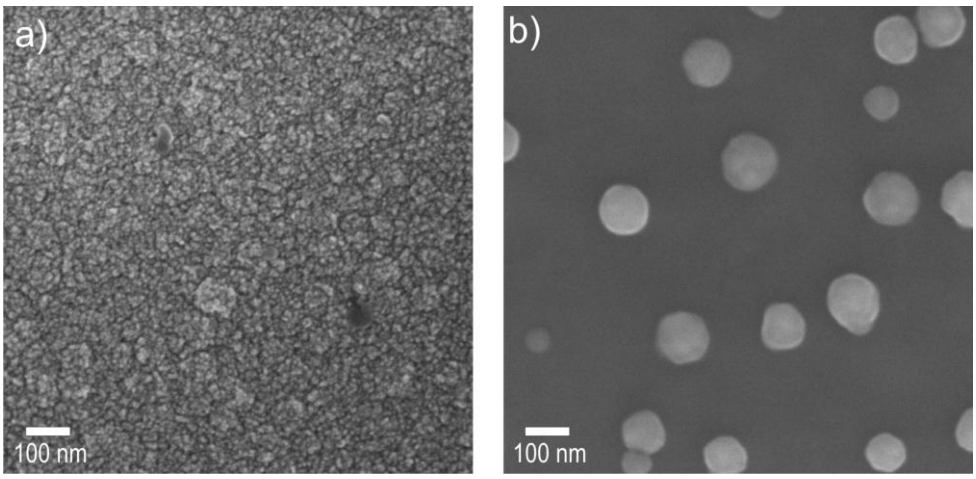

Figure 2.5 SEM micro SEM micrographs of NCD thin films deposited by CVD in the linear plasma reactor. (a) on pre-nucleated, p-doped silicon wafer at 650 ^oC and (b) on untreated a-Si:H at 250 ^oC.

Diamond grown in the linear plasma reactor was performed both with or without pre-nucleation of the substrates which were either silicon wafers (n-type, p-type, intrinsic) or a-Si:H. Temperature during deposition was between 250 ^{o}C and 750 ^{o}C. Microwave plasma power and CH_4:H_2:CO_2 dilution were 1200-2500 W and 5:200-1000:20 sccm, respectively. SEM micrographs of NCD deposited by this methodology can be seen in Figure 2.5. Sample in Figure 2.5 (a) was deposited on pre-nucleated, p-doped silicon wafer at 650 ^{o}C for 20 h while its Figure 2.5 (b) counterpart on untreated a-Si:H at 250 ^{o}C for 24 h.

2.1.3 Post-deposition surface treatment

For the specific purposes of this work it was often necessary to subject the thin films to pre- or post-deposition treatments. The most important of those treatments were:

- silicon oxide etching
- diamond surface terminations

2.1.3.1 Silicon oxide etching

It is well known that when silicon films are exposed to ambient atmospheric conditions, a native oxide layer starts forming on them [61]. This is due to adsorption of species on the surface (mostly oxygen) and occurs regardless of the specific material phase (amorphous or crystalline). Thickness of the resulting oxide layer is typically around 15 Å after a few hours of exposure to ambient environment. While its presence does not pose a significant factor to the topographical structure of the silicon film, it plays a role when those films are used for electrical measurements and applications. This is because the insulating oxide acts as an additional tunneling barrier, meaning that the system needs higher applied voltages to facilitate conduction. This issue is more evident in measurements of poorly conductive materials such as a-Si:H.

There are a number of methods for removal of the native oxide. The ones most widely used are implementing wet chemical etching [62] and/or cleaning in a plasma

of mild gases [63]. In this work we used wet chemical etching in hydrofluoric acid (HF) which is a well- known oxide etchant that does not attack the silicon itself.

Oxide removal was crucial for our experiments. For example, before diamond CVD for better defined nucleation, and before C-AFM electrical current measurements for removal of the additional conduction barrier [62]. Note that the measurement has to be performed shortly after etching since a new oxide layer will start forming within few hours in ambient atmosphere.

2.1.3.2 Diamond surface termination

Termination of diamond surfaces is commonly used for functionalization of the material. It is important for various applications such as field-effect transistors [32] and biosensors [27]. Diamond is typically terminated either by hydrogen or oxygen. Unlike on silicon, H and O terminated surfaces are stable in the long term (years).

Hydrogen treatment of diamond (exposure to H plasma) affects the material in a similar fashion as described above for silicon: it passivates the material by H atoms occupying C dangling bonds, thus not allowing surface reconstruction and phase transitions from sp^3 to sp^2 bonded carbon. Another interesting and widely employed property of H-diamond is its surface conductivity [64-66]. This occurs due to the chemisorbed hydrogen atoms which give rise to negative electron affinity via surface dipole [67-69]. Adsorbed species from ambient exposure are also necessary for this effect [68, 70]. Note that as-deposited diamond is inherently H-terminated due to the hydrogen-rich atmosphere in the CVD reactor.

On the other hand, oxidation of as-deposited diamond provides the original high electrical resistivity of undoped diamond [71]. This is because it gives rise to large density of surface states and positive electron affinity, as opposed to the negative electron affinity and almost no surface states of H-diamond [72]. This difference is due to the higher electronegativity of O when compared to C, thereby causing dipole moment with negative charge on the O atom [68]. The resulting highly resistive diamond can be employed for various applications and experiments such as radiation detectors [73], UV detectors [74], field-effect transistors [66, 75, 76] and diamond charging [77-81].

In this work we used O-diamond thin films for studying charge transport and trapping. Oxidation was done by boiling the samples (200 ^{o}C) for one hour in a HNO_3/H_2SO_4 solution (ratio 1:3) followed by oxygen plasma (300 W) treatment for 3 minutes.

2.2 Material characterization

After the deposition of the materials, we implemented a number of experimental methods for characterization of the structural, chemical and electronic properties of the thin films and nanostructures.

2.2.1 Macroscopic electrical current measurements

These measurements were conducted using a metallic, voltage-biased point-contact on the diamond thin films while the c-Si substrate was grounded. By using a wide range of bias voltage we obtained the current-voltage characteristics (*I/V*) of the films. The data then were evaluated as a function of sample thickness (measured by ellipsometry) and chemical composition (sp^2/sp^3 ratio) as measured by micro-Raman spectroscopy. The former obviously affects the applied field intensity for a given value of applied bias. For example, an order of magnitude difference in thickness (i.e. 100 nm vs. 1 μm) would mean that the effective field is an order of magnitude weaker across the thicker film for the same voltage value ($E=V/m$). On the other hand, chemical composition affects the electrical conductivity of our samples. The richer in sp^2 a diamond film is, the more conductive it will be since sp^2 bonded carbon is graphitic (conductive) as opposed to sp^3 which corresponds to diamond phase (resistive). This means that when we compare diamond films of similar thicknesses, the ones exhibiting higher sp^2 content will conduct higher currents for the same applied bias.

We did not perform *I/V* measurements on the a-Si:H samples. Applying high bias across such films may induce Field-Enhanced metal-induced solid phase crystallization (FE-MISPC). This would change the material phase locally from amorphous to crystalline [82-84]. As c-Si conductivity is higher than the one of a-Si,

such phase transition renders the measurement unreliable since it is not clear what exactly we are measuring. In addition, absolute values of conductivity of the as-deposited a-Si:H are not crucial for this work as will be discussed extensively in Chapter 3.

2.2.2 Advanced microscopy methods

Common optical microscopes use visible light to project and magnify the specimen under investigation. Their spatial resolution is generally limited by a diffraction limit, which is a function of the illumination wavelength and the numerical aperture of the lens. This limits the capabilities of such instruments since the wavelength range is limited to the visible spectrum (390-740nm). Hence, even implementing lenses of the highest quality does not practically improve the resolution past the 200 nm mark.

There are, however, optical microscopy methods able to achieve higher resolution, beyond the diffraction limit of visible light. This includes advanced optical microscopy methods which can for example use light of smaller wavelengths (e.g. ultra-violet), structured illumination, deconvolution procedures or operate in the near-field regime (SNOM).

There are also other microscopy methods which do not use light as the measurement medium which makes them completely independent of the diffraction limit. Such methods are for example various scanning probe and scanning electron microscopies. In this work we used atomic force microscopy (including some of its advanced regimes) and scanning electron microscopy.

2.2.2.1 Scanning Electron Microscopy

SEM is an extension of light microscopy and allows visualization of solid samples using an electron beam for illumination. The principle of SEM operation lies in the wave-particle duality of matter (including electrons), first described by DeBroglie in 1924 [85] and demonstrated by the famous double slit experiment. This property is exploited in SEM which is able to visualize the illuminated specimen by

collecting the products of electron collisions. These are evaluated according to their energy (thus wavelength). That way it is possible to obtain local topographical or chemical composition images by interaction of the electrons with the structural features on the sample. Resolution depends on the beam size and energy Current cutting-edge instruments are able of imaging features as small as 0.4 nm [86]. Figure 2.6 illustrates the most important components of an SEM.

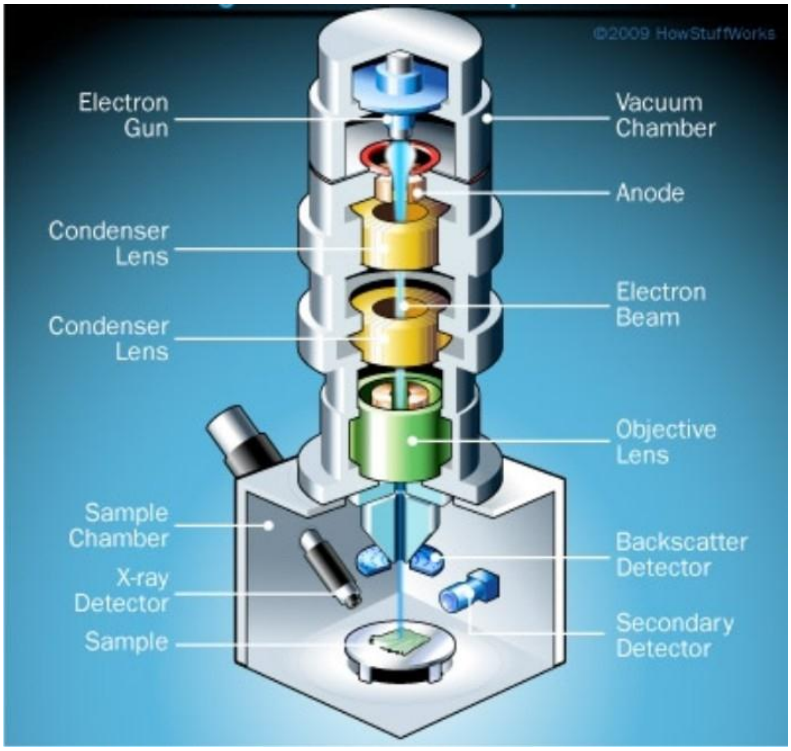

Figure 2.6 SEM scheme. Image courtesy of howstuffworks.com.

SEM implements a series of condenser and objective lenses to decrease the e-beam diameter and focus it on the sample. When an incident electron hits the sample it scatters according to its energy. Low energy beam e^- (usually a few keV) have limited penetration depth and induce emission of e^- from the sample surface. The latter have very low energy (<50 eV) which means that only those which originate near the surface are detectable. If such an e^- is ejected from the bulk it looses its energy before reaching the surface due to interactions with atoms of the sample itself. Therefore, imaging these secondary electrons can give information about the sample morphology. Scattering in this case is obviously inelastic because the energy of the incident e^- does not equal the energy of the emitted electron(s).

Increasing the beam energy allows it to penetrate deeper into the specimen. Those e^- are nevertheless affected by the various inelastic scattering events, but they possess sufficient energy to exit the sample in case their direction changes, e.g. by deflection from an atomic nucleus (backscattering). In this case the energy of the backscattered e^- is mostly conserved (elastic scattering) as it typically equals 80-90% of the initial energy [87]. As different elements backscatter e^- differently, with respect to their atomic number, detection of such e^- can give chemical composition information about areas in the bulk consisting of more than one element.

High beam energy (tens of keV) can also enable X-ray emission from the specimen. Those X-rays can be collected and give information regarding the specific elements present in the sample. As the high energy beam strikes the sample, it can excite low orbital e^- tightly bound to atomic nuclei. The electron deficiency is compensated by an outer shell e^- moving to take the place of the missing, excited e^-. As the transition involved a higher energy outer shell electron moving to a lower orbital (less energetic), the excess energy is emitted as an X-ray. Since every element has distinct e^- spectral lines, the X-rays are characteristic of the element that emitted them. The SEM method that works in this principle is Energy-Dispersive X-ray spectroscopy (EDX).

In this work we used secondary emission SEM on diamond samples because its non-destructive nature (low beam energy) is combined with excellent spatial resolution, enabling it to resolve even fine structural details of nanocrystals. EDX was performed on AFM tips used for various electrical experiments in order to determine the tip quality, durability and whether species from the sample get deposited on the tip during the measurements.

2.2.2.1.1 Electronic contrast in SEM

As already discussed above, diamond surface terminations with oxygen or hydrogen produce opposite results in terms of electron affinity. This property finds practical usage when measuring SEM on diamond samples exhibiting both types of surface termination [27]. In Figure 2.7 we can see such a surface. It is clear that H-diamond is brighter than its O-diamond counterpart. This occurs due to the negative electron affinity present in H-diamond which reduces the work function, effectively

enabling easier e^- emission [88, 89]. Such pattern cannot be obtained by optical microscopy unless visualized by some specific adsorption.

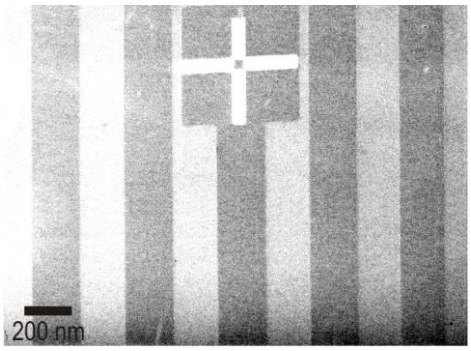

Figure 2.7 SEM micrograph of an NCD film exhibiting both oxidized (darker) and hydrogenated (brighter) areas. Image after [27].

2.2.2.2 Scanning Probe Microscopy

Another family of methods able to provide resolution well below the diffraction limit of visible light is scanning probe microscopy (SPM). It employs a sharp tip (ideally atomically sharp) which scans the sample surface and provides information about its properties (structural, electrical, thermal, magnetic etc.). The signals that can be measured depend on the specific measurement regime. Conductive atomic force microscopy, for example, gives information about local currents (and thus local conductivity), Magnetic Force Microscopy measures local magnetic fields, Scanning Capacitance Microscopy provides local capacitances and so on. Several SPM techniques are capable of true atomic resolution [90].

2.2.2.2.1 Scanning Tunneling Microscopy

The first SPM-based method that was invented and gave the initiative for a number of spin-off techniques over the last thirty years was Scanning Tunneling Microscopy (STM). It was realized in the early 1980's by Binnig and Rohrer of IBM Zurich who shared a Nobel Prize for that invention in 1986 [91]. Their innovation was the combination of electron tunneling from a tip with the emerging technology of

piezoelectric ceramics. Tunneling of electrons occurs between the tip apex and the surface atoms under applied bias when the STM tip scans the sample at a sufficiently small separation distance (typically <1 nm). STM can resolve surface conductivity, morphology and density of states.

2.2.2.2.2 Atomic Force Microscopy

AFM follows the sample surface through cantilever deflection as opposed to electrical current changes in STM. The deflection is caused by mechanical, Casimir or Van der Waals forces depending on the mode of operation. The measurement is realized by using a laser focused on top of the scanning cantilever and deflected to an array of photodiodes. That way it is possible to map the sample surface by evaluating the laser signal. AFM thereby provides height information, which is not available in standard SEM. There are three basic modes of operation in AFM: contact, non-contact and tapping.

Contact mode

In this mode the cantilever is kept constantly in contact with the specimen during scanning as illustrated in Figure 2.8 (a). Surface morphology is thus obtained through the repulsive forces between the sample and the tip which cause cantilever deflection. Contact mode AFM has two basic scanning regimes like its STM counterpart: constant height, and constant force (current in STM). The former scans the surface at a preset z-position which does not change with respect to the topography. This regime is simple and fast but it is good only for reasonably flat surfaces since sloping samples could cause AFM tip crashes (high hillocks) or move the tip far from the surface (deep pits).

The constant force regime is more sophisticated as it implements a feedback circuit for control of the height, thus adjusting it with respect to the sample topography. When the deflection deviates from the given set-point, the amplifier applies the appropriate voltage to the z-piezo element. This helps to maintain a constant contact force throughout the whole measurement and eliminates the artifacts present in the constant height regime.

Non-contact mode

In this mode the sample is scanned with the tip being held at a distance of 5-15 Å away from the surface as seen in Figure 2.8 (b). At this distance attractive Van der Waals forces dominate. Due to the fact that the attractive force is much smaller (< 1 nN) compared to repulsive forces present in contact mode AFM (> 1 nN), the cantilever is oscillated in order to map the scanning area according to the amplitude, frequency or phase changes of the oscillations.

Non-contact mode is good for mapping sensitive samples that cannot withstand the higher forces of contact mode scanning and for achieving atomic-scale resolution. However, it is mostly usable in vacuum. It is well known that under ambient conditions, an adsorbed contaminant layer is forming on the samples. Thus, performing non-contact AFM measurements in air introduces the possible artifact of detecting the contaminant layer instead of the real surface.

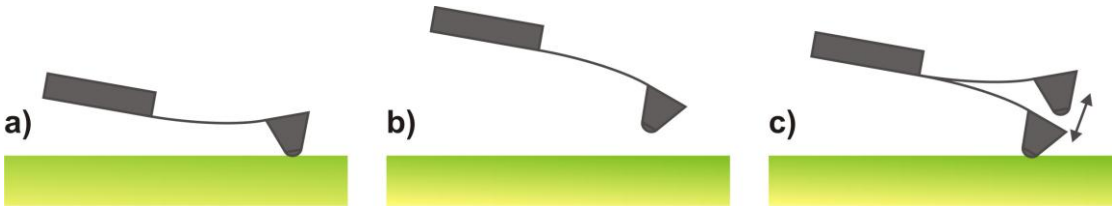

Figure 2.8 Scanning modes of AFM. (a) Contact, (b) non-contact and (c) tapping.

Tapping mode

In tapping mode the cantilever oscillates with larger amplitude than in non-contact mode (> 10 nm). The tip moves from up to down position where it comes in touch with the surface as illustrated in Figure 2.8 (c). This causes the tip to tap the specimen and immediately get withdrawn. Thereby, it avoids dragging or damaging of the tip or surface. The various signals that can be deduced from this mode (topography, phase etc.) are obtained by changes in the cantilever oscillating amplitude, resonance frequency and phase due to the tip-sample interactions.

When it comes to topography measurements in air, this mode is usually preferred since it combines the accuracy of contact mode with the delicate nature of non-contact mode.

It is obvious that the employed probes represent a crucial part of the experiment. They must be selected carefully with mind on the sample and regime of operation. For example, it is not advised to use stiff cantilevers for mapping sensitive samples. The most important parameters of an AFM cantilever are the spring constant and resonance frequency. Their relation is given by:

$$\omega = 0.5\pi^{-1}(k/m)^{1/2}$$

where ω is the resonance frequency, k is the spring constant and m is the cantilever mass. While the resonant frequency has to be reasonably high (in the kHz range) in order to minimize the cantilever's sensitivity to any building and airborne mechanical noise, the spring constant needs to be low for the detection of very small forces. This is achieved by minimizing the factor of mass, which results in extremely small cantilevers (typically a few hundreds of micrometers long). Spring constant of an AFM cantilever is typically 0.1-20 N/m, which means that a force of 1 nN would cause a deflection of 1 nm-5 pm.

The tip that is fixed at the end of an AFM cantilever is commonly described by its curvature radius. The radius defines the amount of detail that can be observed in a measurement. This dependence is similar to the operation wavelength in optical microscopes or e-beam focus/energy in SEM, as discussed above. Typical AFM tip curvature is 10-50 nm. There are, however, ultra-sharp tips of ~1 nm radius which can resolve very fine details in demanding measurements.

2.2.2.2.3 Conductive Atomic Force Microscopy

C-AFM is an advanced contact mode method which is able to measure local currents simultaneously with the topography. C-AFM is therefore important not only determining the local conductivity of a specimen but also for correlating that conductivity to the topographical features. This is achieved by applying a bias between the tip and the substrate during scanning as seen in Figure 2.9. It can be viewed as "contact mode STM", since C-AFM also includes the quantum tunneling principle in local current detection. The key difference between them is that C-AFM deduces the topography from cantilever deflection as in standard contact mode AFM. This means that structural and electronic properties can be de-coupled, unlike in STM.

It is implied that a conductive tip and a sample exhibiting conductivity within the available bias voltage and pre-amplifier range are necessary for such measurement.

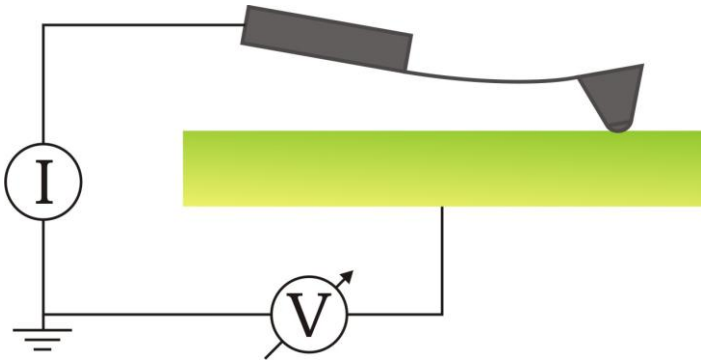

Figure 2.9 C-AFM scheme.

2.2.2.2.4 Kelvin Force Microscopy

Another advanced and useful AFM-based method is Kelvin Force Microscopy (KFM). It is able to provide information about the electric potentials of a specimen. From the potentials it is also possible to deduce material work-function [78] and electrostatic charges [41, 42]. KFM does not require a conductive sample to be realized. It does, however, need a conductive AFM tip to be able to compensate the electric potential of the surface being scanned. Typical KFM scheme is illustrated in Figure 2.10 (a).

It is well known that bringing two different materials in contact initiates e^- flow (diffusion) in order to achieve equilibrium throughout the junction. This e^- flow occurs with respect to the work function difference between the two materials and continues until the system can be described by a single chemical potential (Fermi level). KFM is based on this principle and measures the electric potential difference between the AFM tip and the sample as seen in Figure 2.10 (b) [92].

There are two ways to realize such measurement with an AFM: one or two pass regime. The most common method implements a two pass scheme. During the first pass the AFM maps the topography in standard tapping mode. Then it re-scans the same line at a user-defined Δz from the surface (usually a few nanometers) following the topography scheme as recorded from the first pass. During the second

pass the tip is excited by a signal containing AC and DC components. The AC voltage causes slight oscillations (~ 1 nm) due to the potential difference between the tip and the surface. The DC component is then adjusted accordingly in order to nullify these oscillations. This DC offset corresponds to the contact potential difference between the tip and the specimen, thus the difference between their work functions and/or electrostatic charges.

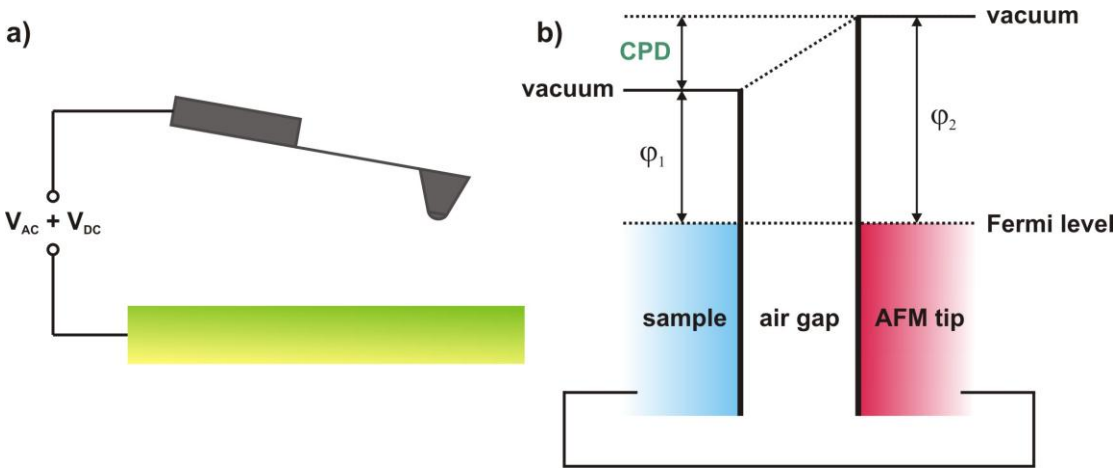

Figure 2.10 (a) Experimental setup of KFM and (b) energetic scheme.

The single-pass KFM is able to provide potential and topography measurements at the same time by tuning the tip at a different resonance for every signal (e.g. primary resonance for topography and first harmonic for potential). It is a relatively new technique whose edge over the 2-pass KFM is obviously the half measurement time needed for a given experiment. However, it is not so well researched and documented like the 2-pass technique resulting sometimes in ambiguous artefacts and questionable results. Moreover, precise control of tip-surface distance, which is essential for accurate characterization, is difficult. For this reason, all KFM work in this thesis was conducted using the 2-pass method.

2.2.2.2.5 AFM-aided surface modifications

In this work we did not only characterize our diamond or silicon thin films. We actively engaged in modifying their structural, chemical and electrical properties

by various methods. The two main methods that our laboratory devised, developed and patented are diamond charging [93] and a-Si:H nanocrystallization [94]. Both these methods are AFM-based, meaning that the induced modifications can be confined down to micro- or nano-scale dimensions.

Diamond Charging

Applying a DC bias on the AFM tip while scanning in contact mode an O-diamond film can charge the film locally. Scheme of this experiment can be seen in Figure 2.11. The mechanism is attributed to a combination of polarization and charge trapping [77] with the latter being the dominant contributor to the process [80]. Trapping requires current flow which allows charges to be trapped in empty and/or defect states in the material. The applied voltage threshold for facilitating conduction depends on the nature of the diamond film under investigation, namely its sp^2/sp^3 ratio. The more graphitic phase it contains, the lower the conduction threshold is, meaning that sp^2-rich films are charged easier.

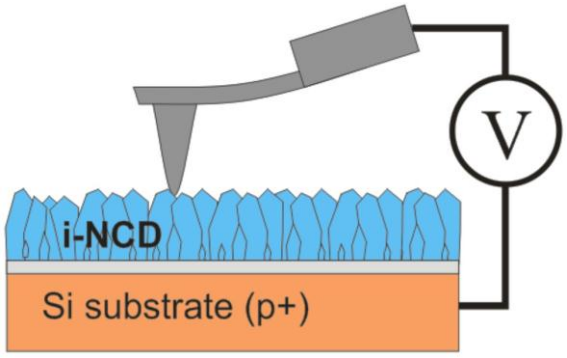

Figure 2.11 Experimental scheme for O-diamond charging.

By performing KFM on the same area after the voltage application, we observe a shift in the exhibited electric potential, which means that the film is locally charged. The detected charge polarity and magnitude depends on the bias voltage polarity and magnitude that was used for the charging [79]. These charged patterns can be later used for electrostatic assembly of nanoparticles from colloidal solutions or gases, given that the induced potential is high enough [42]. Results and detailed up-to-date progress is presented in Chapter 3.

There are of course several other methods able to produce localized charging. One could use SEM, biased needles, ion sources etc. However, only our combined AFM/KFM methodology is able to provide such precise position control, sub-μm spatial resolution and, most importantly, in-situ qualitative/quantitative evaluation of the injected charge.

Nanocrystallization of a-Si:H

As already discussed above, when an electrical current is allowed to pass through a-Si:H deposited on a metal that encourages crystallization (such as Ni), it initiates FE-MISPC [82]. The change in the material phase occurs due to diffusion of NiSi species through the amorphous tissue. This diffusion is encouraged by voids present inside the amorphous tissue [82]. As the void density is dependent to the hydrogen content within the silicon (more H, more voids), H-rich films are necessary for effective FE-MISPC.

By using an AFM probe as the top electrode (with the bottom being the metal film under the silicon) we have confined FE-MISPC in nanoscopic areas [83, 84]. Experimental setup can be seen in Figure 2.12. The challenge is to avoid discharge from the parasitic parallel capacitance (C_p) which arises from the wiring [95].

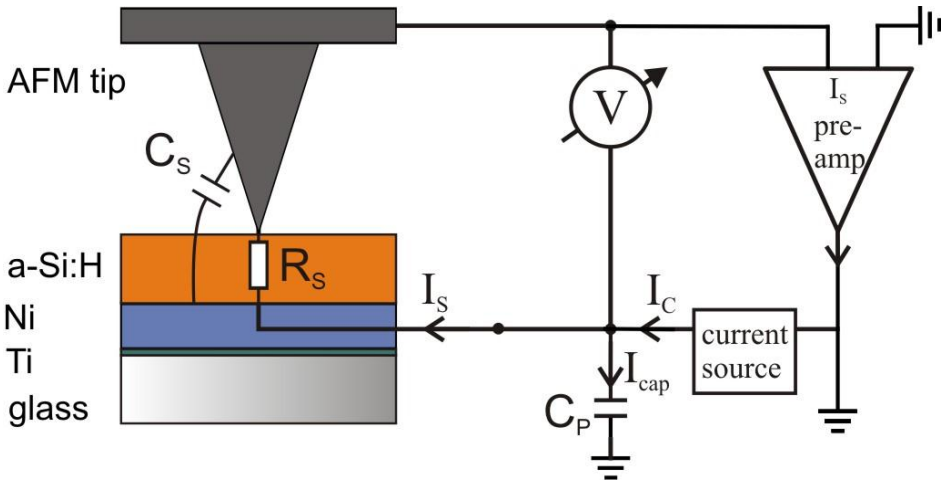

Figure 2.12 Experimental scheme for nanocrystallization of a-Si:H

Besides in-situ crystallization, this method is able to produce shallow, resistive pits in the a-Si:H film. Those pits can be then used for, instance, as nucleation centers for the deposition of silicon nanocrystals, effectively producing well organized arrays

of c-Si in the amorphous matrix [96]. Results and detailed up-to-date progress is presented in Chapter 3.

2.2.3 Raman scattering

Obtaining information about material structure and chemical composition through AFM is quite difficult. It requires special experimental conditions and can work reasonably only on atomically flat samples. Moreover, such characterization is confined merely to the sample surface [97].

A popular method able to provide effective characterization of material composition from both surface and the bulk is Raman spectroscopy. The principle of operation is similar as in SEM with backscattered electron detection. In other words, it also implements scattering. This time, however, the specimen is probed by light, meaning that photons and not electrons are the detection medium here.

In similarity with e^- scattering, photons also scatter either elastically or inelastically. This means that when a photon interacts with matter and is not fully absorbed, it is possible to detect a backscattered photon bearing either the same or different energy of the incident one. Elastically scattered photons are the vast majority in light-induced excitation methods (Rayleigh scattering). Nevertheless, there is also the small probability (about one in the 10^7) of a photon being inelastically scattered which represents the Raman effect. This can happen in two different ways. As the incident photon interacts with a molecule, it excites it to a virtual state of higher energy. When it relaxes, it emits a photon of lower (Stokes) or higher (anti-Stokes) energy, as we can see in Figure 2.13. Through this energy exchange it is possible to detect the different elements and molecules as well as the way they are bonded since energy spectral lines are unique in every material.

Raman is the preferred technique for characterization of thin films because it is a fast, non-contact method, operated in ambient conditions. It is also safe for the samples given that the probing laser intensity is within the appropriate range. The edge of Raman over SEM and EDX is obvious since there is no high intensity e^- beam illumination (tens of keV) which could potentially damage the sample. Furthermore, Raman spectroscopy can identify different phases of the same element (e.g.

amorphous or crystalline silicon), something that is not possible to resolve by EDX. In addition, vacuum is not required, which cuts down measurement time drastically.

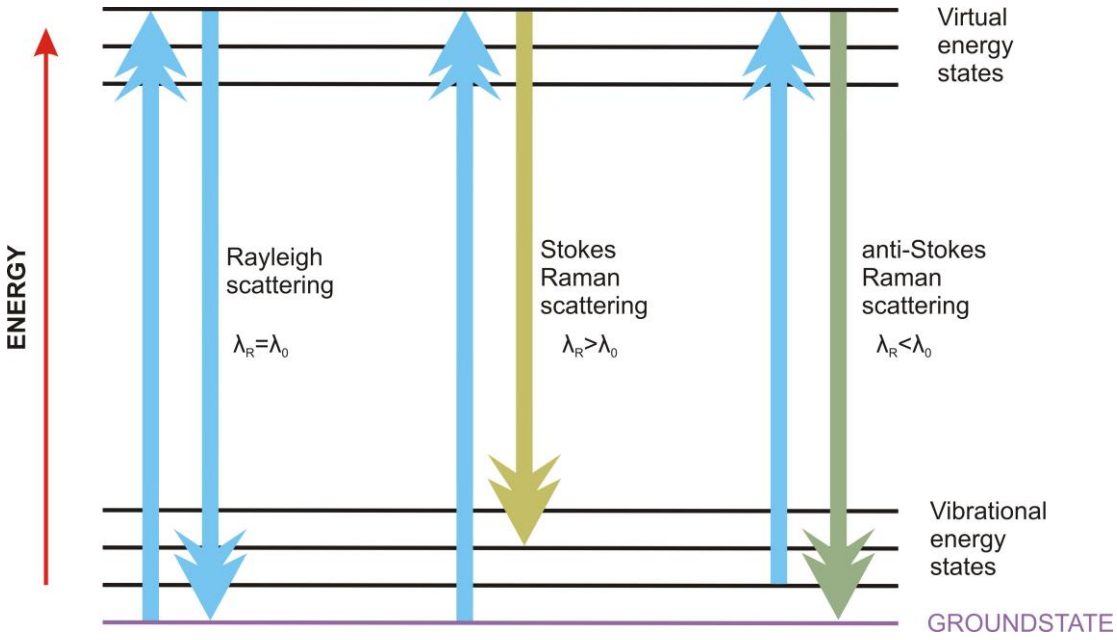

Figure 2.13 Energy scheme of Rayleigh (elastic) and Raman (inelastic) scattering.

2.2.3.1 Microscopic Raman spectra and maps

Detection of the Raman effect falls into two categories: Macroscopic and microscopic. In the former the excitation laser illuminates the sample "as is". This method is optimal when there is a need for simultaneous excitation of a large number of molecules which can be excited by light of low intensity. Micro-Raman, on the other hand, employs objective lenses in order to reduce the beam size and focus the light on a microscopic area of the sample. The minimum diameter of the beam, which depends on the excitation wavelength and the objective lens used to focus the light (diffraction limit), can be of sub-micron dimensions. This means that it is possible to retrieve structural data from sub-μm areas and thus investigate thoroughly sample homogeneity. The excellent lateral resolution combined with the laser light penetration depth of up to ~1 μm makes this method excellent for the study of thin films.

Besides measuring a single spectrum on the specimen, micro-Raman also offers the possibility of mapping microscopic areas. This can be done by measuring multiple adjacent spectra within a defined area and using each one of them as a pixel for constructing the image. Color of each pixel is defined by the specific material properties revealed by its corresponding spectrum. Hence, micro-Raman mapping is extremely useful for characterization of samples whose structural properties can vary even within a very small area (few μm).

All the above mentioned benefits of this method make our nanocrystalline diamond (slight changes in sp^2/sp^3 phase) and mixed-phase silicon (detection of amorphous phase and crystals) samples ideal candidates for micro-Raman investigation.

3. Results and Discussion

The two main research directions followed in this work were local electrostatic charging of nanocrystalline diamond and nanocrystallization of amorphous silicon thin films. In this chapter we present and discuss the results obtained using those methods and propose ways to combine them both for the creation of diamond-on-silicon nanosystems.

3.1 Local diamond charging

Previous work employed NCD thin films deposited on silicon with an intermediate Au layer [77]. This proved that the detected (by KFM) electrostatic potential after charging is not due to the silicon substrate. Hence, scanning in contact mode with AFM and a biased probe charges the diamond film itself. The work by Čermák et al. also showed that the system exhibits an electret-like behavior since the polarity of the induced electrostatic field depends on the polarity of the applied voltage unlike in a-Si thin films [78]. In addition, *I/t* characteristics obtained by applying a constant voltage on the NCD by a macroscopically-sized contact indicated the capacitive character of the system.

3.1.1 NCD deposited on silicon

In the article "AFM induced electrostatic charging of nanocrystalline diamond on Silicon" [79] we describe a series of charging experiments performed on NCD deposited directly on silicon (no Au interlayer). We found that the charging saturates for the bias voltage of 20 V in the positive and -25 V in the negative polarity. Nevertheless, the achieved potential contrast of 1.4 V peak to peak is almost 5 times larger than what was observed before [77]. *I/V* characteristics indicated the presence of larger currents, probably as a result of the better mechanical and electrical contact achieved by omitting the Au electrode.

It was also shown that applying a voltage of opposite polarity on pre-charged areas recovers the surface potential to the value it had before the charging. Thus the charged areas can be reset by the opposite polarity (decharging).

Scan speed-dependent measurements indicated that the magnitude of the induced potential due to charging depends on how long the biased tip was in contact with the surface: the longer the time (lower scan speed), the higher the induced potential. In addition, the charged features are larger and more homogeneous for lower scan speeds.

The charging appeared homogeneous by that time with no significant differences between charged grains and grain boundaries. Moreover, temporal stability of the induced charge on bare silicon samples showed that the effect of charge decay is determined by the ambient conditions, irrespective of the material being charged.

Phys. Status Solidi B **246**, No. 11–12, 2798–2801 (2009) / **DOI** 10.1002/pssb.200982305

physica status solidi b
www.pss-b.com
basic solid state physics

AFM induced electrostatic charging of nanocrystalline diamond on silicon

E. Verveniotis*, J. Čermák, A. Kromka, and B. Rezek

Institute of Physics, ASCR, Cukrovarnická 10, 16253 Prague 6, Czech Republic

Received 30 April 2009, revised 4 August 2009, accepted 18 August 2009
Published online 19 October 2009

PACS 68.37.Ps, 72.20.Jv, 81.05.Uw, 81.07.Bc, 81.15.Gh

* Corresponding author: e-mail verven@fzu.cz, Phone: +420 220 318 519, Fax: +420 220 318 468

A nanocrystalline diamond (NCD) thin film (80 nm) is deposited on a p-type Si substrate and oxygen terminated by r.f. oxygen plasma. An atomic force microscope (AFM) is used to induce electrostatically charged micrometer-sized areas on the diamond film by applying a bias voltage on the AFM tip during contact mode scan. Trapped charge is detected by Kelvin force microscopy showing a potential difference of up to 1.4 V. The potential amplitude and spatial distribution are controlled by the bias voltage applied on the tip (±30 V) and scan speed (2–20 μm/s). Contribution of diamond bulk and grain boundaries to the charging effects shows no significant variations. We compare the results with the charging of bare Si substrate.

© 2009 WILEY-VCH Verlag GmbH & Co. KGaA, Weinheim

1 Introduction Electrostatic charging of surfaces is widely used in a variety of technological processes. It improves wetting of plastics for painting or it is used in printers and copiers for toner positioning on paper. It is also employed in electronics, e.g. for influencing transport properties of field-effect transistors. Electrostatic charging is also an effective method for guiding self-assembly of micro- and nanosized particles on insulating materials [1, 2, 3].

A large variety of materials have been used for electrostatic charge storage (semiconductors [4] including amorphous silicon [5] as well as polytetrafluoroethylene and poly(methyl methacrylate) [6]) by various methods (laser, ion, or electron beam illumination, using electrodes etc). Charged patterns of submicrometer resolution can be created by using nanometer-sized probes, such as those employed in atomic force microscopy (AFM) [4, 5].

For such local and intentional charging, diamond has been only little investigated [7] even though it packs some amazing properties for applications. It can, for example, be used as a semiconductor for device fabrication [8], is biocompatible [9, 10] and can be deposited on diverse substrates [11]. From the electronic point of view, diamond is a wide band gap semiconductor (5.5 eV). Intrinsic diamond is thus electrically insulating and transparent for visible light. It is transformed into p- or n-type semiconductor by boron [12] or phosphorus [13] doping, respectively. Also, when the intrinsic diamond is hydrogen-terminated (H-diamond), a thin (<10 nm) conductive layer is formed close to the diamond surface (surface conductivity) under ambient conditions [14]. So far, research on electronic properties of oxygen-terminated intrinsic diamond (O-diamond) has been focused on only a few applications (e.g., radiation or UV detectors [15]), although except for the lack of electrical conductivity it still keeps the other outstanding properties.

In this paper we report on local electrostatic charging of an oxygen-terminated nanocrystalline diamond (NCD) surface which, unlike in a previous work [7], is deposited directly on silicon. When NCD is deposited on gold, voltages higher than 30 V damage locally the films [7]. Additionally, the potential differences observed on NCD-Au were relatively low (±150 mV within ±30 V range) considering the diamond band gap of 5.5 eV. This can be attributed to the low stability of the mechanical contact and, thus, to a low quality of electrical contact. Charging of NCD on Si is hence promising as the diamond film adhesion is much better due to the Si-C bonds at the interface.

2 Materials and methods NCD films were prepared by microwave plasma chemical vapor deposition using the following parameters: substrate temperature 820 °C, deposition time 16 min, microwave plasma power 900 W, CH_4:H_2 dilution 3:300. Resulting thickness was about 80 nm. The substrate was conductive p-doped silicon nucleated by water-dispersed detonation diamond powder of 5 nm nominal particle size (NanoAmando, New Metals and

WILEY InterScience DISCOVER SOMETHING GREAT

© 2009 WILEY-VCH Verlag GmbH & Co. KGaA, Weinheim

Chemicals Corp. Ltd., Kyobashi) using an ultrasonic treatment for 40 min. After the deposition, the diamond films were oxidized in r.f. oxygen plasma (300 W, 3 min).

Localized charging was performed by scanning in contact mode with an atomic force microscope (N-TEGRA system by NT-MDT). N-doped, diamond coated silicon probes were used (DCP11 by NT-MDT). The bias voltage was applied to the tip while the silicon substrates were grounded. An external voltage amplifier (HP 6826A) was connected to the cantilever and controlled by the AFM software via a signal access module, to apply voltages higher than 10 V. Charged areas of various size and shape were created by applying voltages in the range of ±30 V. The scan speed varied between 2 and 20 μm/s. KFM was used to detect potential differences across the sample [16]. No background corrections were applied to the data.

The potential differences were studied as a function of the charging voltage up to the saturation of trapped charge. Voltages were applied also on pre-charged areas in order to determine whether it is possible to restore the potential value: e.g., applying a bias of 25 V on an area previously charged by −25 V.

By experimenting with different probe speeds at the same voltage we studied the potential and dimensions of the charged areas depending on duration of the voltage application. For the rest of the experiments we used 10 μm/s as the probe velocity.

Similar experiments were done also on bare silicon substrate for comparison. Decay of the trapped charge in time was studied by KFM scans after 1 and 16 h. The relative humidity and temperature during all experiments were in the ranges of 19–32% and 20–26 °C, respectively.

3 Results In Figs. 1a and b we can see the KFM potential images and corresponding plots of potential difference after charging as a function of bias voltage. The individual curves correspond to the same experiment repeated on different spots on the sample. The inset images illustrate typical KFM measurements after charging. The scan was made from the bottom up gradually raising the bias from 0 to 25 V in steps of 5 V (Fig. 1a). For the negative polarity (Fig. 1b) the voltage was lowered down to −30 V with the same step size (−5 V). We observe a saturation of potential at 20 and −25 V for the positive and negative polarity, respectively. The saturation potential is about 300 mV for both polarities. However, there are noticeable variations depending on the place. The highest charged potentials achieved so far were 500 mV for the positive and 900 mV for the negative voltage polarity.

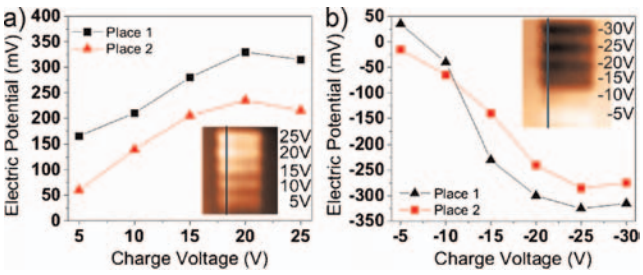

Figure 1 (online color at: www.pss-b.com) Plots of surface potential differences vs. surroundings after charging using (a) positive and (b) negative voltage polarity. The individual curves correspond to different spots on the sample. The inset images illustrate typical KFM measurements after charging. The lines are guides for the eye

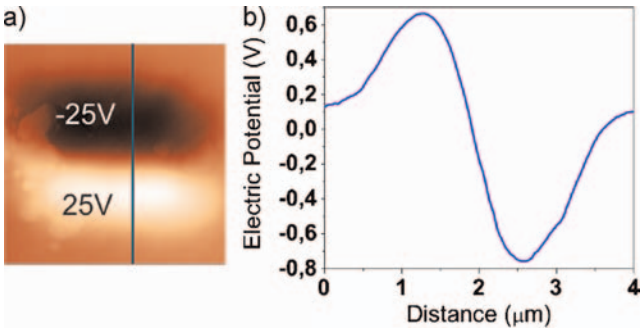

Figure 2 (online color at: www.pss-b.com) KFM potential image and profile of locally charged NCD film showing the total potential difference of 1.4 V.

Figure 2 shows such total potential difference of 1.4 V between the positively and negatively charged areas next to each other. They were charged using ±25 V. All the charged potentials are well above the ones seen on NCD-Au.

I/*V* characteristics of the NCD film on Si measured by the AFM tip is shown in Fig. 3. It exhibits slightly asymmetric double-junction character with exponential rise of the currents from zero toward positive and negative voltages. The currents are about six times larger compared to NCD-Au [7].

KFM image in Fig. 4 shows that charging a pattern by +25 V within the region that was previously charged using −25 V restores the potential back to the potential of unexposed surroundings. On the electric potential plot we can see that complete de-charging is achieved only for the center of the cross which was scanned twice (vertically and horizontally). De-charging by positive voltage is obviously

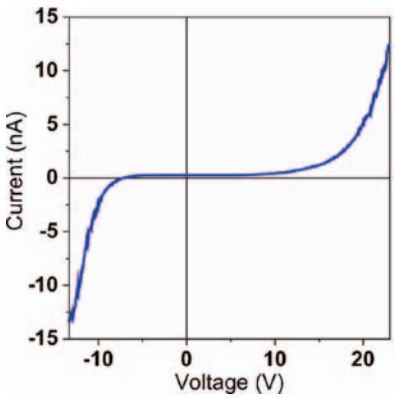

Figure 3 (online color at: www.pss-b.com) *I*/*V* characteristic of the NCD film on Si measured by an AFM tip. Voltage is applied to the tip.

© 2009 WILEY-VCH Verlag GmbH & Co. KGaA, Weinheim

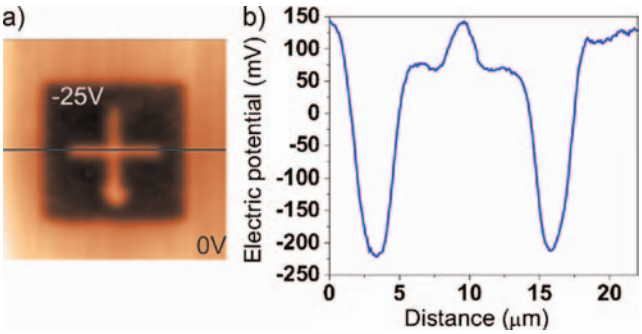

Figure 4 (online color at: www.pss-b.com) (a) KFM image showing a cross "written" by +25 V on a negatively pre-charged NCD area (−25 V). (b) Corresponding potential profile across the pattern.

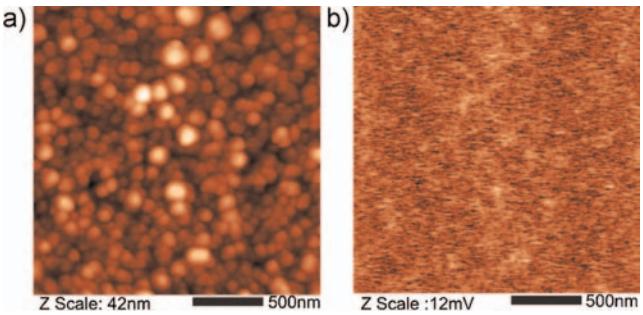

Figure 6 (online color at: www.pss-b.com) (a) Detailed topography and (b) potential map of NCD charged by −20 V.

slower, most likely due to asymmetric *I*/*V* characteristics of the system. As also shown in Fig. 3, same charge current amplitudes can be achieved for both polarities (±13nA) yet the positive voltage needed for this current is higher than the negative (22, −15 V, respectively).

Speed-dependent measurements in Fig. 5 show correlation between the scan speed during the charging, resulting electric potential, and dimensions of the produced features (rectangles). The scan speeds were 2, 5, 10, and 20 μm/s and the bias voltage was always −10 V. The size of the charged features is closer to the actual scanned area (1.08 μm) for the two higher scan speeds. The features are more uniformly charged for the two lower scan speeds. This is due to the fact that when scanning get slower, the desired voltage is applied longer on a particular spot, thus inducing more charge. Note that this occurs for charging voltages below the saturation. For charging voltages close or above the saturation threshold (+20 and −25 V), the potential becomes saturated so fast that charging will produce the same results independent of the scan speed.

Figure 6 illustrates the detailed AFM topography and KFM potential map of a 2 μm^2 NCD surface after charging. For that experiment, a large area (8 μm^2) was charged by −20 V, and then a smaller KFM scan was taken (2 μm^2) in its center. In this particular case the KFM image was flattened to show the details. The maximum contrast is 12 mV. The root-mean-square of the potential variations is 2 mV. These variations are negligible compared to the overall potential differences with respect to the un-charged background (200 mV). Same potential contrast was observed also prior to charging. This indicates that the NCD film becomes charged uniformly at such microscopic regions.

Figure 7a shows the result of charging on bare silicon. Four voltages were used in the following sequence: 10, 20, −10, and −20 V. The induced potential shifts are close to what we observed on NCD for the positive polarity (400 mV). They are much smaller on the negative polarity though (160–200 mV) since higher negative voltages produce positive potential. This positive potential is due to the local anodic oxidation of silicon [5]. We also measured the charge decay on Si as a function of time (Fig. 7b). The charging voltages were 20 and −7 V. After 16 h we observed 50 mV decay for the positive and 100 mV for the negative polarity. This is comparable to the charge decay on NCD [7].

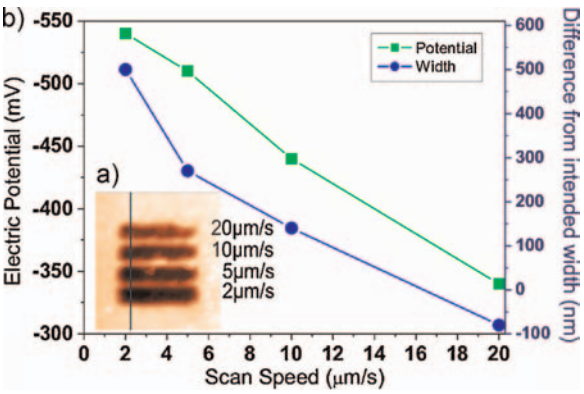

Figure 5 (online color at: www.pss-b.com) (a) KFM image of stripes produced on NCD by different scan speeds at −10 V. (b) The potential of the features and difference in their size from the originally intended (scanned) width as a function of the scan speed. The lines are guides for the eye.

4 Discussion As seen on all the KFM images, both positive and negative potential changes are observed. This is attributed to the electret-like behavior of the NCD films [7]. It was noticed though, that even by keeping the experimental parameters stable (sample, charge voltage, tips), we could

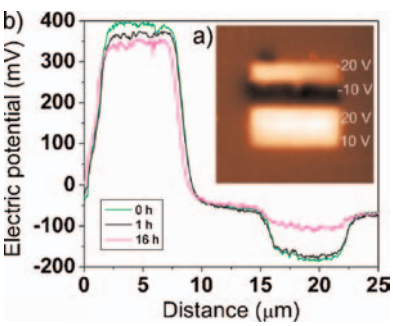

Figure 7 (online color at: www.pss-b.com) (a) KFM image of charge patterns on Si. (b) The decay of the stored charge on silicon (charged by +20 and −7 V) as a function of time.

© 2009 WILEY-VCH Verlag GmbH & Co. KGaA, Weinheim

not obtain the same electric potential shifts every time. The variations were usually around 50–100 mV but sometimes could be as high as 400 mV.

On the other hand, the saturation voltages of 20 and −25 V as shown in Fig. 1 are typical. Even though we could not reproduce the same potential values every time, 20 and −25 V were the voltages for which no further potential shifts were possible. Results in Fig. 4 show that also charging and de-charging by the same voltage amplitude on the same spot is reproducible.

The reproducibility of saturation voltages and de-charging while potential shifts are generally not the same for a specific bias voltage may mean that the amount of charge which can be stored depends on the material properties of a particular area being charged.

Nevertheless, the electric potential differences achieved were up to five times larger than the ones observed when a gold electrode was used between the Si and the NCD. Even when taking into account the above-mentioned local material-related random variations, the potential differences often exceed the Si bandgap (1.1 V).

We also observe that for bias voltages over the saturation threshold the potential does not only saturate but decreases slightly as well (see in Fig. 1). This is probably due to the faster detrapping of the charged states which occurs due to the increasing bias voltage [17].

The slight potential variation observed on the KFM images from left to right is due to the fact that the KFM scans were done vertically with slow scan direction from left to right. Small fluctuations between the scan lines may be caused by unstable measurement conditions (e.g., tip condition).

The *I*/*V* curve shows higher current values for lower applied bias without the Au electrode. As work-function of p-type Si (4.8 eV) is close to Au (5.0 eV) those higher current values are achieved most likely due to the better mechanical contact of NCD-Si which results in better electrical contact. This may be the reason for the higher potentials achieved within similar voltage range.

Detailed KFM measurements after charging indicate that the NCD film becomes charged relatively homogeneously and influence of grain boundaries is negligible. This is somewhat surprising as electronic properties of the grain-boundaries are expected to be different. One possible reason may be possible inaccurate resolution of the grain boundary potential because of the edge transfer function in KFM [18] which leads to averaging of the grain boundary potential with its surroundings. Nevertheless, it is obvious that the overall charge is dominated by charging of the diamond itself.

As for the charge temporal stability, the charge decay on Si was after 16 h exactly the same as the one reported for the NCD deposited on Au after 15 h [7]. Lateral extensions on the charged regions remained the same even after the decay. As the material, charged potential, and applied voltages are completely different, it leads us to an assumption that this decay over time could be in all cases an outside effect, most likely due to the ambient environment.

5 Conclusions It was found that for voltages above 20 V or below −25 V it is not possible to store more charge in the NCD films. It was also proven that the charging is fully reversible if an inverse bias of the same magnitude is applied on the previously charged area. The use of Si substrate instead of Au enabled us to achieve as high as 1.4 V potential difference. However, the maximum potential achieved by charging varies, which is probably a material-related effect. The charge stored in Si exhibited similar decay as on NCD-Au which indicates that this decay is a general, not material-related effect and is most likely caused by the ambient atmosphere.

In case we manage to standardize high potential contrast (>1 V) on diamond, it could be used for some applications such as electrostatically guided assembly of organic materials on pre-patterned areas of desired geometries.

Acknowledgements We would like to acknowledge the kind assistance of Z. Poláčková with surface oxidation and Dr. J. Potměšil with NCD deposition. This research was financially supported by AV0Z10100521, research projects KAN400100701 (GAAV), LC06040 (MŠMT), LC510 (MŠMT), 202/09/H041, and the Fellowship J. E. Purkyně (ASCR).

References

[1] H. Fudouzi, M. Kobayashi, and N. Shinya, Adv. Mater. **14**, 1649 (2002).
[2] W. Wright and D. Chetwynd, Nanotechnology **9**, 133 (1998).
[3] P. Mesquida and A. Stemmer, Microelectron. Eng. **61**, 671 (2002).
[4] H. Jacobs and A. Stemmer, Surf. Interface Anal. **27**, 361 (1999).
[5] B. Rezek, T. Mates, J. Stuchlík, J. Kočka, and A. Stemmer, Appl. Phys. Lett. **83**, 1764 (2003).
[6] N. Naujoks and A. Stemmer, Microelectron. Eng. **78/79**, 331 (2005).
[7] J. Čermák, A. Kromka, and B. Rezek, Phys. Status Solidi A **205**, 2136–2140 (2008).
[8] B. Rezek, D. Shin, H. Watanabe, and C. E. Nebel, Sens. Actuators B **122**, 596–599 (2007).
[9] B. Rezek, D. Shin, H. Uetsuka, and C. E. Nebel, Phys. Status Solidi A **204**, 2888–2897 (2007).
[10] B. Rezek, D. Shin, and C. E. Nebel, Langmuir **23**, 7626–7633 (2007).
[11] A. Kromka, B. Rezek, Z. Remeš, M. Michalka, M. Ledinský, J. Zemek, J. Potměšil, and M. Vaněček, Chem. Vap. Deposition **14**, 181–186 (2008).
[12] C. E. Nebel, Nat. Mater. **2**, 431 (2003).
[13] S. Koizumi, M. Kamo, Y. Sato, H. Ozaki, and T. Inuzuka, Appl. Phys. Lett. **71**, 1065 (1997).
[14] F. Maier, M. Riedel, B. Mantel, J. Ristein, and L. Ley, Phys. Rev. Lett. **85**, 3472 (2000).
[15] Y. Koide, M. Liao, and J. Alvarez, Diamond Relat. Mater. **15**, 1962 (2006).
[16] B. Rezek and C. E. Nebel, Diamond Relat. Mater. **14**, 466 (2005).
[17] M. Rogalla, T. Eich, N. Evans, R. Geppert, R. Goppert, R. Irsigler, J. Ludwig, K. Runge, T. Schmid, and D. G. Marder, Nucl. Inst. Meth A **395**, 49 (1997).
[18] H. O. Jacobs, P. Leuchtmann, O. J. Homan, and A. Stemmer, J. Appl. Phys. **84**, 1168–1173 (1998).

© 2009 WILEY-VCH Verlag GmbH & Co. KGaA, Weinheim

3.1.2 Chemical composition of NCD and its impact to charging

In the article "Local electrostatic charging differences of sub-100 nm nanocrystalline diamond films" [80] we implemented sub-100 nm thin films that had almost identical morphology and structure as evaluated by SEM, AFM and Fourier Transform Infrared Spectroscopy (FTIR). However, as the films were deposited under different experimental conditions, they exhibited differences in their material composition (sp^2/sp^3 phase ratios) as measured by micro-Raman spectroscopy. This was the reason for their different response when subjected to charging. We found that higher concentration of graphitic phase in a NCD film reduces the conduction threshold resulting in more intense and better spatially defined charged features.

Phys. Status Solidi A **207**, No. 9, 2040–2044 (2010) / **DOI** 10.1002/pssa.201000014

physica status solidi a
www.pss-a.com
applications and materials science

Local electrostatic charging differences of sub-100 nm nanocrystalline diamond films

E. Verveniotis*, J. Čermák, A. Kromka, M. Ledinský, Z. Remeš, and B. Rezek

Institute of Physics, ASCR, Cukrovarnická 10, 16253 Prague 6, Czech Republic

Received 24 February 2010, revised 8 June 2010, accepted 6 July 2010
Published online 18 August 2010

Keywords AFM, KFM, SEM, NCD, Raman, charging

* Corresponding author: e-mail verven@fzu.cz, Phone: +420 220 318 519, Fax: +420 220 318 468

Nanocrystalline diamond (NCD) thin films are deposited on p-type Si substrates at different deposition temperatures (600–820 °C) in thicknesses below 100 nm. The films are then terminated by oxygen using r.f. oxygen plasma. Atomic force microscopy (AFM) is used to induce electrostatically charged micrometer-sized patterns on the diamond films by applying a bias voltage on the AFM tip during a contact mode scan. Trapped charge is detected by Kelvin force microscopy, showing potential shifts different in geometry and amplitude on each film for the same absolute bias voltages. The films have similar structure and grain size, measured by AFM and scanning electron microscope (SEM). Fourier transform infrared spectroscopy (FTIR) in reflection regime shows the solidity of the films. Material differences are resolved via micro-Raman spectroscopy. Different charging properties are thus attributed to the differences in relative amount of diamond and sp^2 phase.

© 2010 WILEY-VCH Verlag GmbH & Co. KGaA, Weinheim

1 Introduction Electrostatic charging of surfaces is widely used in a variety of technological processes. It improves wetting of plastics for painting or it is used in printers and copiers for toner positioning on paper. Electrostatic charging is also an effective method for guiding self-assembly of micro- and nanosized particles on insulating materials [1–3]. It can also be employed in electronics, *e.g.*, in memory devices.

A large variety of materials have been used for electrostatic charge storage [semiconductors [4] including amorphous silicon [5] as well as polytetrafluoroethylene and poly(methyl methacrylate) [6]] by various methods (laser, ion, or electron beam illumination, using electrodes, *etc.*). Charged patterns of sub-micrometer resolution can be created using nanometer-sized probes, such as those employed in atomic force microscopy (AFM) [4, 5].

As regards such local and intentional charging, diamond has been only little investigated [7, 8] even though it packs a unique set of properties for applications. It can, *e.g.*, be used as a semiconductor for device fabrication [9], is biocompatible [10, 11] and can be deposited on diverse substrates [12]. From the electronic point of view, diamond is a wide band gap semiconductor (5.5 eV). Intrinsic diamond is thus generally electrically insulating and transparent for visible light. It is transformed into p- or n-type semiconductor by boron [13] or phosphorus [14] doping, respectively. Only when the intrinsic diamond is hydrogen-terminated (H-diamond), a thin (<10 nm) conductive layer is formed close to the diamond surface (surface conductivity) under ambient conditions [15]. While this feature attracted considerable interest and research effort in the past, research on electronic properties of highly resistive oxygen-terminated intrinsic diamond (O-diamond) has been limited to only a few applications (*e.g.*, radiation or UV detectors [16]), although except for the lack of electrical conductivity, it still keeps the remaining outstanding properties of diamond. Detection and understanding of electrostatic charging of diamond is crucial for many diamond-based electronic applications from detectors to field-effect transistors, batteries, and silicon on diamond (SOD) systems.

In this paper, we report on local electrostatic charging of oxygen-terminated nanocrystalline diamond (NCD) thin films deposited on silicon. The films were deposited at different temperatures and thicknesses below 100 nm. Different electrical behavior as well as different properties of the films according to the specific deposition conditions are discussed for resolving charge contributions both quantitatively and qualitatively.

2 Materials and methods NCD films were prepared by microwave plasma chemical vapor deposition using the following parameters: (1) substrate temperature 820 °C,

© 2010 WILEY-VCH Verlag GmbH & Co. KGaA, Weinheim

deposition time 16 min (sample A) (2) 600 °C, 80 min (sample B) (3) 600 °C, 150 min (sample C). For all samples microwave plasma power was 900 W and CH_4:H_2 dilution was 3:300 sccm. Resulting thickness was 74 nm (sample A), 45 nm (sample B), and 81 nm (sample C), respectively. The substrates were conductive p-doped silicon wafers nucleated by water-dispersed detonation diamond powder of 5 nm nominal particle size (NanoAmando, New Metals and Chemicals Corp. Ltd., Kyobashi) using an ultrasonic treatment for 40 min. After the deposition, the diamond films were oxidized in r.f. oxygen plasma (300 W, 3 min).

Localized charging was performed by scanning in contact mode with an atomic force microscope (N-TEGRA system by NT-MDT). Conductive, diamond coated silicon probes were used (DCP11 by NT-MDT). The bias voltage was applied to the tip while the silicon substrates were grounded. An external voltage amplifier (HP 6826A) was connected to the cantilever and controlled by the AFM software via a signal access module, to apply voltages higher than 10 V. Applied voltages were in the range of −20–20 V and the scan speed was always 10 μm/s. Kelvin force microscopy (KFM) was then used to detect potential differences across the sample [17]. The KFM potential values and differences are given as measured, not with respect to the vacuum level. The potential differences were studied as a function of the charging voltage, effective field and specific sample properties. *I*/*V* characteristics were measured locally, using the same experimental setup and voltage range. Relative humidity and temperature during all AFM experiments were in the ranges of 20–32% and 22–26 °C.

For resolving typical grain size, shape, and film homogeneity scanning electron microscopy (SEM) was applied. Film thickness was measured by ellipsometry. Micro-Raman Spectroscopy and Fourier transform infrared spectroscopy (FTIR) in reflection regime were employed to determine the material properties and nanostructure of the thin films.

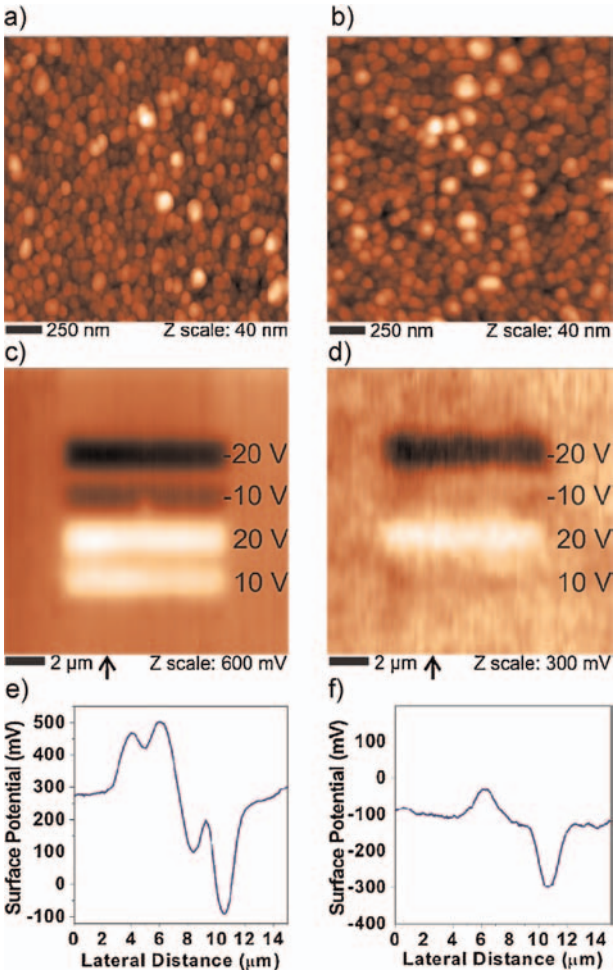

Figure 1 (online colour at: www.pss-a.com) (a, b) 2 μm^2 topography AFM scans on samples A and B, respectively. (c, d) 15 μm^2 surface potential map of charged features on samples A and B, respectively. Charging voltages are shown next to the exposed areas. Arrows indicate the cross-sections plotted in (e, f), respectively.

3 Results Figure 1(a, b) illustrates the typical AFM topography over a 2 μm^2 area of the NCD films [(a) sample A, (b) sample B]. Their morphology is very similar and the root-mean-square (RMS) roughness is 5 nm in both of them.

Figure 1(c, d) shows 15 μm^2 KFM images after a typical charging experiment [(c) sample A, (d) sample B]. The charging voltage of 10, 20, −10, −20 V was applied in an 8 μm^2 area during contact mode AFM scan, while scanning horizontally and with slow scan direction from the bottom to the top. We can see that the charged features in sample A are homogeneous and are observed for every value of bias voltage applied. On the contrary, the features in sample B are relatively inhomogeneous, and present only for the higher voltage settings (±20 V).

The surface potential values are also significantly different. Figure 1(e, f) shows the graphs of the cross-sections indicated by the arrows in the KFM images [Fig. 1(c, d)]. We can see four distinct surface potential peaks in the sample A graph, while in the one corresponding to sample B there are only two. The overall contrast is 600 mV (sample A) and 270 mV (sample B). The absolute potential values with respect to the background for the highest voltage settings in both polarities were 210, −390 mV and 70, −200 mV, respectively. The above described trend concerning the relative electric potential variations with respect to the charge voltage is typical, even though the absolute potential values can vary depending on the specific place of the sample in which the experiment was conducted [8]. This is reproducible across the sample area as well as between samples deposited under the same conditions.

In the *I*/*V* characteristics measured by AFM [Fig. 2(a)], we can see that for the same values of bias voltage the generated charging currents are lower in sample B. This is more pronounced for the negative polarity where a higher voltage is needed for current generation in the same sample (−15 V *vs.* −6 V). This effect is even more noticeable if we plot the current as a function of electric field (it is larger in sample B due to its smaller thickness), as seen in Fig. 2(b).

© 2010 WILEY-VCH Verlag GmbH & Co. KGaA, Weinheim

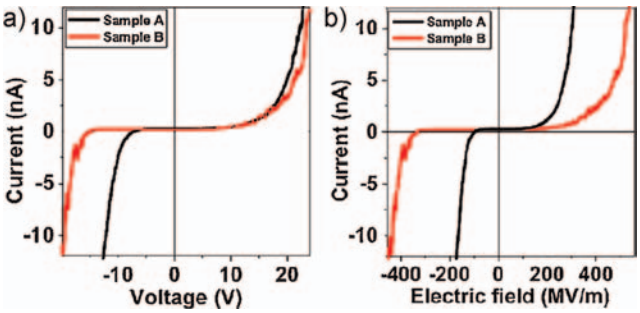

Figure 2 (online colour at: www.pss-a.com) Charge current plotted against the (a) applied voltage and (b) applied electric field.

Figure 3 shows SEM images of sample A (a) and sample B (b). As observed also with AFM, the surface morphology of the films is very similar and the grain size is comparable. Several typical grain sizes (31, 64, and 85 nm for sample A; 29, 42, and 70 for sample B) are indicated in the images. AFM topography [Fig. 1(a, b)] also resolved a similar grain size in both the films, but the grain shapes are not so sharp compared to the SEM. This can be explained by the high curvature of the AFM tips used (70 nm radius) which is comparable to the size of the grains being scanned. These tips were used due to their diamond coating which allows them to be more resistant to wear while scanning hard surfaces such as diamond.

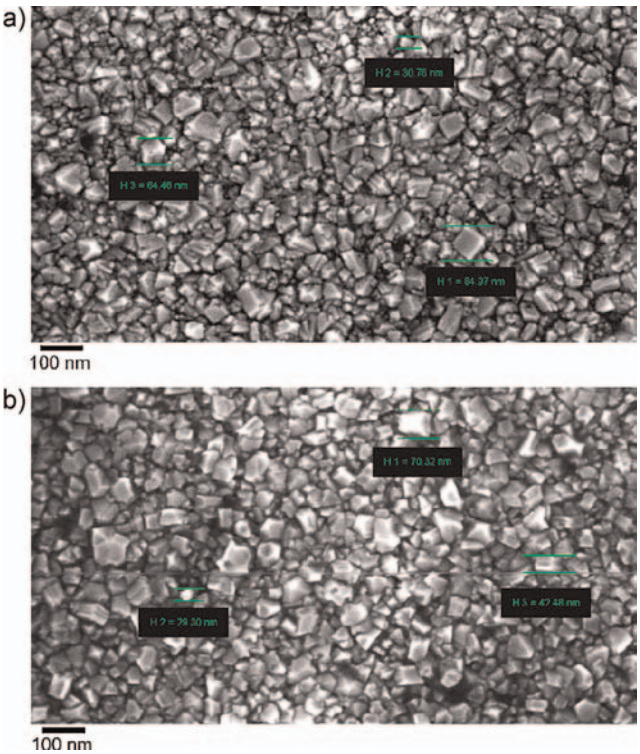

Figure 3 (online colour at: www.pss-a.com) SEM of (a) sample A and (b) sample B. Several typical grain sizes are indicated in the images as measured.

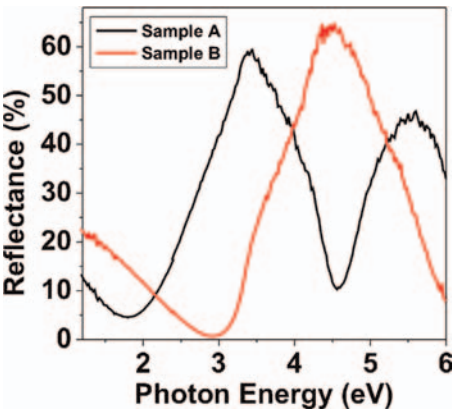

Figure 4 (online colour at: www.pss-a.com) FTIR spectroscopy in reflection regime of NCD thin films.

In volume, thin nanodiamond films may be grown porous or with a lot of voids or inhomogeneities. The presence of such defects can affect the electrical and optical properties of the film. The measured specular optical reflectance spectra of our NCD layers (Fig. 4) were modeled using effective medium approximation (EMA) in the commercially available software FilmWizard. In our case the EMA layer is modeled as a mixture of diamond and voids. The real component of the index of refraction of diamond is the same as the one of single crystal intrinsic diamond ($n = 2.38 + 0.011/L^2 + 0.003/L^4$, where L is the wavelength in μm), while the imaginary index of refraction part is $k = A^* \exp(B/L)$ (where the parameters A and B are found by fitting the reflectance spectra). Then the NCD layer is best represented by two EMA layers: one representing the bulk and the second the surface where the thickness of the surface EMA layer is two times the RMS surface roughness (=10 nm for both samples). The diamond bulk EMA layers may differ by their thickness (67 nm *vs.* 37 nm), but they exhibit similarly high solidity in both cases (98% *vs.* 95%, sample A, B, respectively). The surface layer is considered as "porous" with a 50:50 relation between the material and air due to the non-zero surface roughness. Note that the thickness found during the fitting (77 nm sample A, 47 nm sample B) was very close to the values measured by ellipsometry (74 and 45 nm, respectively).

Micro-Raman spectra (UV laser, $\lambda = 325$ nm) shown in Fig. 5 reveal that despite the similar surface structure, the films have material differences. Both films exhibit clear sp^3 peak at 1332 cm^{-1} indicating diamond character. Yet, in relation to the diamond peak, sample A exhibits higher sp^2 (graphitic) phase compared to sample B. Calculating the relative percentage of the diamond phase from Raman spectra $[I_D/(I_D + I_{sp^2})]$, we find the values of 63% in sample B and 39% in sample A. Higher sp^3 content in sample B deposited at 600 °C is in agreement with previous report that the optimum temperature for depositing NCD is around 600 °C [18]. Note that both 600 and 820 °C films exhibit surface conductivity when hydrogen-terminated, indicating similar electrical behavior.

© 2010 WILEY-VCH Verlag GmbH & Co. KGaA, Weinheim

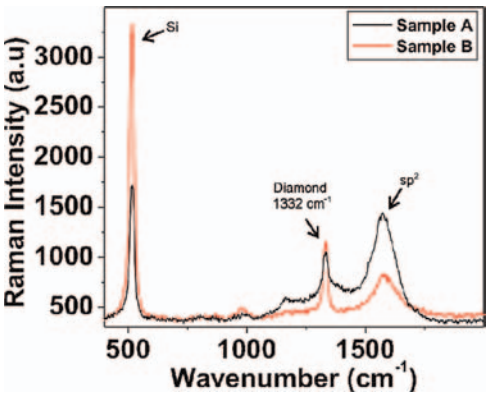

Figure 5 (online colour at: www.pss-a.com) Micro-Raman spectra of NCD thin films.

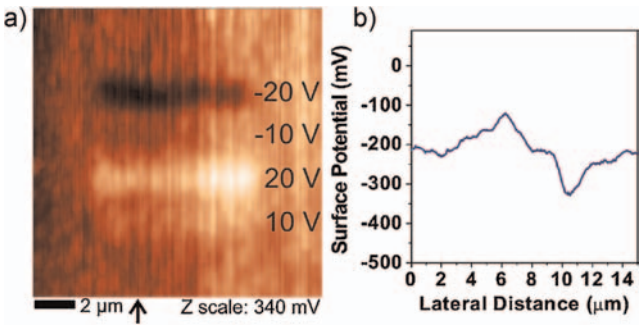

Figure 6 (online colour at: www.pss-a.com) (a) 15 μm^2 surface potential map of charged features on sample C. Charging voltages are shown next to the exposed areas. The arrow indicates the cross-section plotted in (b).

4 Discussion As seen in the KFM images, both positive and negative potential changes are observed. This can be attributed to the electret-like behavior of the NCD films [7]. The electric potential shifts achieved in each sample were different though: three times more positive and twice more negative potential for the high charge voltage setting.

The different electric potential shifts can be partially explained by *I*/*V* curves. Typically, we observe higher currents in sample A for a given voltage, except for the barrier region between about ±7 V. This is even more pronounced when plotted as a function of electric field. As sample A is thicker than sample B, one would expect smaller currents. Hence, it must be the material difference indicated by Raman spectra that is behind this effect.

When we applied 10 V, which means that we attempted to charge with similar current amplitudes (<1 nA) In both samples, a potential shift was observed only on sample A. Furthermore, we can also see that −3 nA on sample A (−10 V bias) induce practically the same potential shift as −12 nA (−20 V bias) do in sample B (190 mV *vs*. 200 mV). From the above, we can conclude that sample B needs higher currents in order to charge and charges with less efficiency. This current is generated by generally higher bias voltages.

The above is despite the fact that the applied electric field for any given voltage is 60% stronger on sample B as compared to sample A due to the thickness difference between the two (E = Voltage/Thickness). Furthermore, considering the generally higher voltages needed to generate current in sample B, the intensity of the electric field for any given non-zero charge current on this film can be twice as high compared to sample A. We also assume that the geometry of the field is always the same as we use the same type of AFM tips which have the same apex radius (70 nm) meaning that the contact area does not change taking into consideration the low surface roughness of both our films (5 nm).

The reflectance-FTIR spectra (Fig. 4), which provided the means for modeling our system using EMA, indicated similar high material solidity in both our samples. Therefore, the differences in charging cannot be attributed to structural inhomogenities within the bulk of the films.

Contributions to the observed potential shifts may come from charge being trapped in the grain surface/boundary states and from polarization of the material [7]. As capacitance of the thinner layer is expected to be higher compared to the thicker one (assuming the same material properties) more charge ($Q = C^*V$) should be stored in the thinner film. This is not the case. Hence, the charging is most likely dominated by the trap states in our case. This explains higher charging of sample A which has relatively higher sp^2 content and larger volume. As the films are "solid" (based on FTIR), more sp^2 is mostly related to more grain boundaries in the volume, which corresponds to more surface (interface) states. The states should be of graphitic nature so that they exhibit continuous density of states that is able to keep charges irrespective of the polarity [19].

To support this assumption, we deposited sample C (600 °C, 150 min, 81 nm). Charging results shown in Fig. 6 are similar to the ones obtained from sample B. Here the contrast is somewhat lower (230 mV *vs*. 270 mV, samples C and B, respectively). This can be attributed to the slightly higher fraction of sp^3 phase present in sample C (67% as measured by Raman spectroscopy).

Figure 2(b) shows that the thinner sample B needs larger electric fields to facilitate electronic conduction. This introduces a higher probability of field-induced charge carrier detrapping [20], which might be another reason for the lower potentials observed on the thin sample B. However, on the sample C the electric field applied is comparable to the sample A (due to the similar thickness of 81 and 74 nm, respectively), yet the charging behavior is still similar to sample B. Therefore, we suggest that the relative sp^2 content in the NCD films is the dominating factor for the observed charging properties.

5 Conclusions It was shown that NCD diamond thin films deposited for 16 min in 820 °C have morphology and grain size similar to those of the films deposited for 80 min in 600 °C. In spite of similar surface morphology, the amount of

© 2010 WILEY-VCH Verlag GmbH & Co. KGaA, Weinheim

stored charge differs significantly per both applied voltage and absolute current values. Homogeneity of charged features is also different. Reflectance-FTIR revealed (through EMA modeling) that the solidity of both our films is similar in the volume. Material differences of the films were resolved by Raman spectroscopy that detected relatively more sp^2 phase in the thicker sample. Still all samples exhibit similar electrical behavior.

The charging properties of the ultra-thin NCD films can be thus tailored by the deposition conditions according to application requirements. More sp^2 phase in the films leads to more intense and spatially better defined charged features (*e.g.*, for batteries). Minimizing sp^2 phase reduces induced charge as well as conduction. This may be optimal feature *e.g.*, for SOD applications where both electrostatic charging and electronic transport should be minimized.

Acknowledgements We would like to acknowledge the kind assistance of Z. Poláčková with surface oxidation, Dr. J. Potměšil with NCD deposition, Dr. K. Jurka with SEM imaging and Dr. K. Vyborny with ellipsometry. This research was financially supported by AV0Z10100521, research projects KAN400100701 (GAAV), LC06040 (MŠMT), LC510 (MŠMT), 202/09/H0041, SVV-2010-261307 and the Fellowship J. E. Purkyně (ASCR).

References

[1] H. Fudouzi, M. Kobayashi, and N. Shinya, Adv. Mater. **14**, 1649 (2002).
[2] W. Wright and D. Chetwynd, Nanotechnology **9**, 133 (1998).
[3] P. Mesquida and A. Stemmer, Microelectron. Eng. **61**, 671 (2002).
[4] H. Jacobs and A. Stemmer, Surf. Interface Anal. **27**, 361 (1999).
[5] B. Rezek, T. Mates, J. Stuchlík, J. Kočka, and A. Stemmer, Appl. Phys. Lett. **83**, 1764 (2003).
[6] N. Naujoks and A. Stemmer, Microelectron. Eng. **78/79**, 331 (2005).
[7] J. Čermák, A. Kromka, and B. Rezek, Phys. Status Solidi A **205**, 2136 (2008).
[8] E. Verveniotis Čermák, A. Kromka, and B. Rezek, Phys. Status Solidi B **246**, 2798 (2009).
[9] B. Rezek, D. Shin, H. Watanabe, and C.E. Nebel, Sens. Actuators B **122**, 596 (2007).
[10] B. Rezek, D. Shin, H. Uetsuka, and C. E. Nebel, Phys. Status Solidi A **204**, 2888 (2007).
[11] B. Rezek, D. Shin, and C. E. Nebel, Langmuir **23**, 7626 (2007).
[12] A. Kromka, B. Rezek, Z. Remeš, M. Michalka, M. Ledinský, J. Zemek, J. Potměšil, and M. Vaněček, Chem. Vap. Deposition **14**, 181 (2008).
[13] C. E. Nebel, Nature Mater. **2**, 431 (2003).
[14] S. Koizumi, M. Kamo, Y. Sato, H. Ozaki, and T. Inuzuka, Appl. Phys. Lett. **71**, 1065 (1997).
[15] F. Maier, M. Riedel, B. Mantel, J. Ristein, and L. Ley, Phys. Rev. Lett. **85**, 3472 (2000).
[16] Y. Koide, M. Liao, and J. Alvarez, Diamond Relat. Mater. **15**, 1962 (2006).
[17] B. Rezek and C. E. Nebel, Diamond Relat. Mater. **14**, 466 (2005).
[18] H. Kozak, A. Kromka, M. Ledinsky, and B. Rezek, Phys. Status Solidi A **206**, 276 (2009).
[19] J.-C. Charlier and J.-P. Michenaud, Phys. Rev. B **46**, 4540 (1992).
[20] M. Rogalla, T. Eich, N. Evans, R. Geppert, R. Goppert, R. Irsigler, J. Ludwig, K. Runge, T. Schmid, and D. G. Marder, Nucl. Instrum. Methods A **395**, 49 (1997).

© 2010 WILEY-VCH Verlag GmbH & Co. KGaA, Weinheim

3.1.3 Electrostatically-guided assembly of nanoparticles on NCD

In the article "Guided assembly of nanoparticles on electrostatically charged nanocrystalline diamond thin films" [42] we used an NCD film with high sp^2 phase content, based on our previous findings which indicated its better capability for charge storage. We tried to achieve as high potential contrast as possible in NCD for self-assembly of nanoparticles by electrostatic forces on the exposed areas.

We demonstrated that self-assembly of alumina nanoparticles by electrostatic repulsion or attraction on NCD is indeed feasible. However, in order for the assembly to work, the NCD must exhibit an electric potential contrast of at least ±1 V in the charged pattern vs. the background.

Electric potential contrast of the magnitude required for the self-assembly was not always achievable. This is due to the variation in the induced potential contrast which is observed when repeating the experiment under the same conditions on different spots of the same sample. The variation in the potential contrast was quite large, accounting for potentials in the range of 0.1-1.2 V per polarity. This effect was attributed to the changing quality of tip-surface junction when scanning hard surfaces such as diamond.

Nanoscale Research Letters
a SpringerOpen Journal

NANO EXPRESS Open Access

Guided assembly of nanoparticles on electrostatically charged nanocrystalline diamond thin films

Elisseos Verveniotis*, Alexander Kromka, Martin Ledinský, Jan Čermák, Bohuslav Rezek

Abstract

We apply atomic force microscope for local electrostatic charging of oxygen-terminated nanocrystalline diamond (NCD) thin films deposited on silicon, to induce electrostatically driven self-assembly of colloidal alumina nanoparticles into micro-patterns. Considering possible capacitive, sp^2 phase and spatial uniformity factors to charging, we employ films with sub-100 nm thickness and about 60% relative sp^2 phase content, probe the spatial material uniformity by Raman and electron microscopy, and repeat experiments at various positions. We demonstrate that electrostatic potential contrast on the NCD films varies between 0.1 and 1.2 V and that the contrast of more than ±1 V (as detected by Kelvin force microscopy) is able to induce self-assembly of the nanoparticles via coulombic and polarization forces. This opens prospects for applications of diamond and its unique set of properties in self-assembly of nano-devices and nano-systems.

Introduction

Electrostatic charging of surfaces is widely used in a variety of technological processes. It improves wetting of plastics for painting, it is employed in electronics, e.g., in detectors or memory devices, and it is used in printers and copiers for toner positioning on paper. In this context electrostatic charging has been also explored as an effective method for guiding self-assembly of micro- and nanosized elements on insulating materials [1-3]. Electrostatic charging can be generated by various methods (laser, ion, or electron beam illumination, diverse electrodes, etc.). Charged patterns of sub-micrometer dimensions can be created using nanometer-sized probes, such as those employed in atomic force microscopy (AFM) [4,5].

A large variety of materials have been applied for electrostatic charge storage: semiconductors [4] including amorphous silicon [5] as well as dielectric materials such as polytetrafluoroethylene and poly(methyl methacrylate) [6]. Detection and understanding of electrostatic charging of diamond is crucial for many diamond-based electronic applications from detectors to field-effect transistors, batteries, silicon on diamond systems as well as for electrostatically guided assembly. This is because diamond as a semiconductor material can, for instance, be used for device fabrication [7], for passive and active bio-interfaces [8,9], and can be deposited on diverse substrates in nanocrystalline form [10]. From the electronic point of view, diamond is a wide band gap semiconductor (5.5 eV). Nevertheless, it can be transformed into p- or n-type semiconductor by boron [11] or phosphorus [12] doping, respectively. Intrinsic diamond is generally electrically insulating and transparent for visible light. Only when the intrinsic diamond is hydrogen-terminated (H-diamond), a thin (<10 nm) conductive layer is formed close to the diamond surface (surface conductivity) under ambient conditions [13]. While this feature attracted considerable interest and research effort in the past [14], research on electronic properties of highly resistive oxygen-terminated intrinsic diamond (O-diamond) has been limited. It was related mostly to applications in radiation detectors [15], UV detectors [16], or field-effect transistors [17,18].

As regards local and intentional electrostatic charging, diamond has been only little investigated [19-21] even though it exhibits a unique set of properties for applications as described above. Both positive and negative persistent potential changes were observed on nanocrystalline diamond (NCD) [19], unlike in silicon thin films [5].

* Correspondence: verven@fzu.cz
Institute of Physics ASCR, Cukrovarnicka 10, 16253, Prague 6, Czech Republic

SpringerOpen

© 2011 Verveniotis et al; licensee Springer. This is an Open Access article distributed under the terms of the Creative Commons Attribution License (http://creativecommons.org/licenses/by/2.0), which permits unrestricted use, distribution, and reproduction in any medium, provided the original work is properly cited.

This has been attributed to the capacitor-like behavior of the NCD films [19]. Comparing charging of NCD films prepared on gold [19] and silicon [20] substrates demonstrates that the charging is not due to the substrate itself as could be argued in the case of silicon substrates. The charging has been also shown to be more effective when the NCD films contain more sp^2 phase [21]. Surprisingly, the charging is spatially homogeneous and not confined to grain boundaries where most of the sp^2 is localized [20]. Yet maximal induced electrostatic potential contrast has been reported to be varying by up to 400 mV depending on a position on the sample [20]. This may depend on the local material properties as well as actual tip condition.

In this article, we apply local electrostatic charging of oxygen-terminated NCD films to induce electrostatically driven self-assembly of colloidal nanoparticles into micro-patterns. Considering possible capacitive, sp^2 phase, and spatially related contributions to charging, we employ films with sub-100 nm thickness, and about 60% relative sp^2 content, probe their material uniformity, and repeat experiments at various positions across the films to induce as much potential contrast as needed for the self-assembly.

Materials and methods

NCD films were prepared by microwave plasma chemical vapor deposition using the following parameters: substrate temperature 820°C, deposition time 16 min, microwave plasma power 900 W, CH_4:H_2 dilution 3:300. Resulting thickness was 74 nm as measured by ellipsometry. The substrates were 5 × 10 mm^2 conductive p-doped silicon wafers nucleated by water-dispersed detonation diamond powder of 5 nm nominal particle size (NanoAmando, New Metals and Chemicals Corp. Ltd., Kyobashi) using an ultrasonic treatment for 40 min. After the deposition, the diamond films were oxidized in r.f. oxygen plasma (300 W, 3 min) [22].

Localized charging was performed by scanning in contact mode with an atomic force microscope (N-TEGRA system by NT-MDT). Conductive, diamond-coated silicon probes were used (DCP11 by NT-MDT). Applied contact forces were ~100 nN. The bias voltage was applied to the tip while the silicon substrates were grounded. An external voltage amplifier (HP 6826A) was connected to the cantilever and controlled by the AFM software via a signal access module, to apply voltages within the range of ±25 V (the potential contrast is saturated at these voltages [20]). The scan speed was always 10 μm/s. Kelvin force microscopy (KFM) was then used to detect potential differences across the sample [23]. The KFM potential values and differences are given here as measured, not with respect to the vacuum level. Relative humidity and temperature during all AFM experiments were in the ranges of 20-32% and 22-26°C.

For resolving typical grain size, shape, and film homogeneity, scanning electron microscopy (SEM) was applied (eLine by Raith, secondary electron detector, accelerating voltage 10 kV, working distance 8 mm). Micro-Raman spectroscopy (inVia by Renishaw, HeCd laser, λ = 325 nm, objective 40×, spot diameter 2 μm) was employed to determine the material properties and uniformity across the films.

For achieving directed self-assembly of nanoparticles, a charged sample was immersed vertically into a colloidal emulsion for 10 s. The sample was then let to dry in air for 5 min. The emulsion was prepared by putting 300-500 μl of the aqueous suspension containing the nanoparticles (alumina of 50 nm nominal size, particle concentration 15%, Buehler, USA) into 5 ml of an insulating fluorocarbon solution (Fluorinert FC-77, 3M Company, USA) and ultra-sonicating the mixture for 20 s. Since the two liquids do not mix, ultrasonication provided the means for creating emulsion with microscopic colloidal droplets [3]. FC-77 was selected due to its inertness, letting the charged features to maintain their electrical potential even after immersion, and allowing electrostatic forces to reach relatively far into the emulsion (~1 μm).

Results

Figure 1 shows a typical SEM image of an NCD sample. The NCD film appears continuous and uniform in surface morphology. There are smaller and bigger grains with resolvable crystalline facets. Average size of the grains is 53 ± 35 nm as evaluated from the SEM images. SEM investigation across the whole sample showed very similar structure, which indicates that our film is spatially uniform. The root-mean-square (RMS) roughness measured by AFM is about 5 nm.

Figure 2 shows a typical micro-Raman spectrum of the NCD film. It exhibits clear sp^3 peak at 1332 cm^{-1} indicating diamond character. Note that repeating the measurement on different spots across the sample indicated slight differences in the sp^2 (graphitic) phase content. The calculated relative percentage of the sp^2 phase from Raman spectra $[[I_{sp2}/(I_D + I_{sp2})] * 100]$ [24] is ranging between 58 and 60%.

Figure 3 shows KFM surface potential maps after the typical charging experiments. In Figure 3a we applied the charging voltage of 10, 20, -10, -20 V in an 8 μm^2 area during contact mode AFM scan, while scanning horizontally and with slow scan direction from the bottom to the top. The maximum potential values with respect to the background for the charging voltages of ±20 V are 210 mV for the positive and -390 mV for the negative polarity. Figure 3b shows the KFM map after charging with ±25 V in another 2 μm^2 area. Those voltages are at or above the saturation threshold of

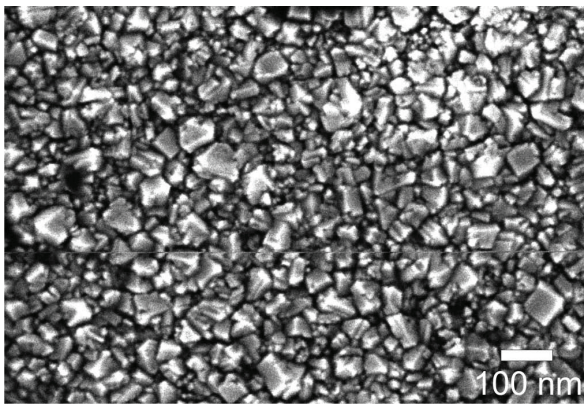

Figure 1 Micrograph from scanning electron microscopy on the employed nanocrystalline diamond thin films.

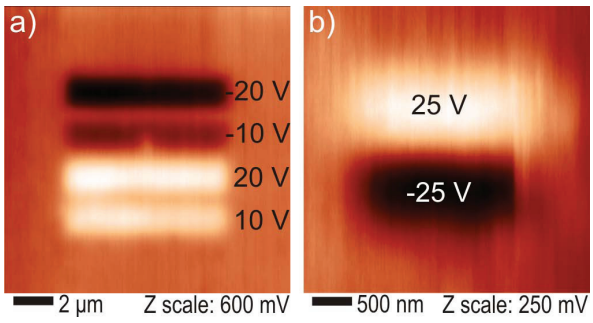

Figure 3 Kelvin force microscopy surface potential maps after typical charging experiments. **(a)** up to ±20 V and **(b)** at ±25 V. Charging voltages are indicated near each stripe pattern.

charging [20]. Yet the maximum potential values are only 110 mV for the positive and -140 mV for the negative polarity.

The maximum achievable potential shift in each polarity was varying when the experiment was repeated (inherently at another position on the sample). This is illustrated in Figure 4a,b, where we can see the total potential contrast varying from 230 to 2000 mV. The data points in Figure 4 correspond to average potential within the individual stripes that were charged using ±20 V (Figure 4a) or ±25 V (Figure 4b). The x-axis values between two integer values in Figure 4a correspond to experiments conducted within the same day. Positive and negative data points at the same x-value were obtained from a charging experiment and KFM in one scan frame such as the ones in Figure 3. Only in the case of x = 4 in Figure 4b the patterns were charged in separate frames (shown in Figure 5c,d). On the graphs we can also observe that charging with ±25 V

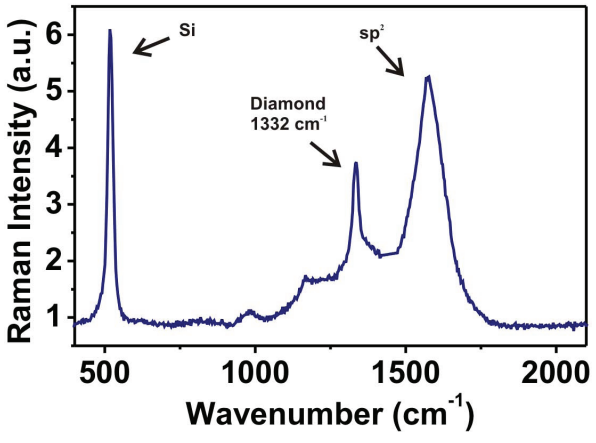

Figure 2 Typical micro-Raman spectrum (UV laser, λ = 325 nm) on the employed nanocrystalline diamond thin films.

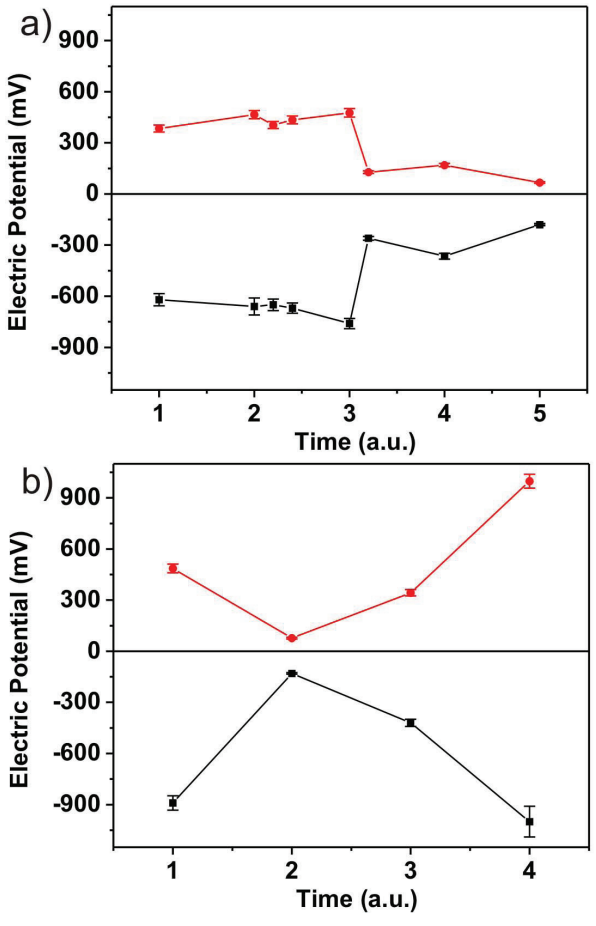

Figure 4 Surface potential shifts after electrostatic charging for positive and negative polarity. The data points correspond to average potential within the individual stripes that were charged using **(a)** ±20 V or **(b)** ±25 V. Positive and negative data points at the same x-value were obtained from a charging experiment and KFM in one scan frame. Only in the case of x = 4 in **(b)** the patterns were charged in separate frames. The x-axis values between two integer values in **(a)** correspond to experiments conducted within the same day.

does not always result in higher potential. Even though we did obtain the highest contrast to date with this voltage (x = 4, Figure 4b), there are features charged with ±20 V that exhibit higher potential than others charged with ±25 V (e.g., x = 2-3 in Figure 4a vs. x = 2, 3 in Figure 4b).

By experimenting repeatedly we were able to achieve ≥1 V contrast in each polarity on our sample and we used those patterns for self-assembly. Figure 5a-d shows the AFM and KFM images of such patterns in each polarity charged with -25 and 25 V (corresponds to x = 4, Figure 4b). The dimensions of the cross arms are 10 × 80 μm. Maximum amplitude of the charged patterns is 1.2 V (average = 1 V) in each polarity. The centers of the crosses show slightly higher potential compared to the rest because they were charged twice (horizontally and vertically). The potential is not double, though, since the charging exhibits saturation as reported before [20]. AFM in such large scale confirms the homogeneity of our samples and excludes possible external contributions to the observed electric potential shifts (i.e., topographical variations). Note that structural details are not resolvable because the size difference between a typical grain and the full scan shown here is at least three orders of magnitude (18-88 nm vs. 80 μm).

In Figure 5e,f we can see optical microscope images of the charged crosses after immersion to the solution containing the alumina nanoparticles. The nanoparticles assembled preferentially on the crosses. Their arrangement is determined by the polarity of the particular charged cross. Negative potential produced a filling effect (Figure 5e), where the assembly occurred on the charged area. Positive potential leads to a decorative effect (Figure 5f), where the nanoparticles attached predominantly on the cross edges. Charged patterns having potential contrast below 1 V did not lead to preferential assembly of the nanoparticles.

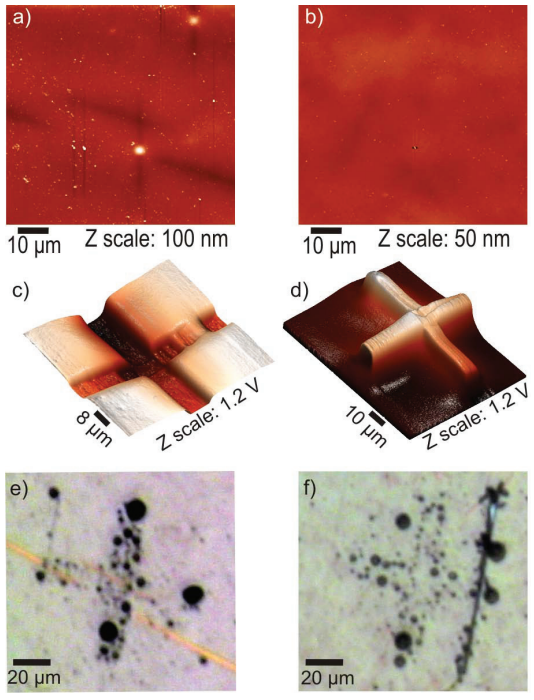

Figure 5 Local topography of typical work areas on the NCD thin films. **(a, b)** AFM morphology on charged areas. **(c, d)** Corresponding KFM of electrostatically charged crosses on the nanocrystalline diamond thin film using **(c)** negative and **(d)** positive voltage. **(e, f)** Optical microscope pictures of the charged crosses after immersion to emulsion containing alumina nanoparticles.

Discussion

In order to generate self-assembly of nanoparticles on charged areas, the electrostatic forces must be high enough to attract particles from the solution and promote assembly. In various charging instances identical to the one shown in Figure 5 but with less charged potential (up to 800 mV average potential) self-assembly was not possible. Therefore, we assume that potential differences below 1 V are insufficient to generate the self-assembly. The contrast of 1.2 V versus the uncharged background was already sufficient to generate self-assembled patterns even though it is still considerably lower than the potentials typically used in the case of dielectric materials (3-5 V) [1-3]. The assembled nanoparticle concentration is higher in the top component of the cross in Figure 5c as it exhibits slightly higher potential compared to the other two components on which particles did assemble. Furthermore, the lower charge in the right element of the same cross (600 mV) leads to missing particles in that region. Combination of positively and negatively charged regions [20] may improve definition of the self-assembled pattern, but it will not increase the electrostatic force itself needed for assembly. Hence the properties and charging process of NCD film have to be optimized to achieve contrast ≥1 V versus the surrounding surface of the film.

The different behavior per polarity can be explained from the fact that the nominally uncharged nanoparticles got positively charged (including their aqueous shell around them) when emulsified in the FC-77. This is due to the relative dielectric constant ε_r difference between the materials (9.9 vs. 1.86), as materials with higher ε_r tend to charge positively when brought in contact with other materials having lower ε_r [3]. Hence, the positively charged nanoparticles cover negatively charged areas via coulomb interaction (see Figure 5e). The edge decoration observed in Figure 5f is due to the attachment of non-charged or weakly charged nanoparticles that are

attracted via polarization effects to the places exhibiting the highest electrostatic field gradient.

It is noticeable that in the present case the selectivity of nanoparticles toward negative versus positive patterns is low. It indicates generally low charge on the nanoparticles in the emulsion. Optimizing the emulsion and/or nanoparticles may improve the selectivity toward specific charge polarity on diamond as reported for dielectric materials [3].

Another problem is the large variation in the potential contrast on the NCD films. There are various factors that can influence the charging and lead to the observed potential contrast variations in different experiments/positions under otherwise same experimental conditions. First factor is the ambient environment. Humidity can affect the size of the meniscus formed between the AFM tip and the sample while scanning under ambient conditions [25]. This can influence the area over which the voltage is applied, possibly altering electric field and current density, current path, as well as capacitance. Ambient temperature variations may also influence the electrical behavior of the system by moving the conduction threshold [26]. Second, the tip-sample junction properties have to be considered. Change in the electrical contact between the tip and the sample could be caused even during the same scan if the surface under investigation is rough [27]. In addition, the AFM tip can be abraded due to scanning. This could lead to local removal of the conductive-diamond coating of the tip, bringing the sample in contact with the residual SiO_2 at the very tip end [28]. This may cause a drop in the applied voltage, which would result in lower voltage across the diamond itself. Third, the cross-sectional morphology of the diamond film may also play a role. As the relative sp^2 content of the charged film is believed to be the governing factor toward effective charging [21], local accumulation of very small grains under the surface on the specific area being charged may lead to an increase in the local sp^2 content (more grain boundaries). This could increase the potential contrast.

In our case, the range of relative humidity and temperature, under which the experiments were conducted, was within 12% and 4°C, respectively. The samples were also relatively flat (5 nm RMS) and uniform. Local material differences based on the micro-Raman spectra are within 2% of relative sp^2 content. We assume that this is not enough to explain variation by almost an order of magnitude in the potential contrast. Hence the tip condition may be the important factor. Even diamond-coated tips may not be durable enough under hard conditions [29]. In spite of the above-mentioned problems, we were able to demonstrate the feasibility of self-assembly on diamond. Understanding and systematically achieving high potential contrast on NCD is only a matter of future research.

Conclusions

We have demonstrated successful electrostatically guided self-assembly of alumina nanoparticles into micro-patterns on NCD thin films. We have shown that the electrostatic potential contrast on the NCD films induced by charging must be ≥ ± 1 V to generate the self-assembly. In spite of variations in the maximum potential contrast (0.1-1.2 V) - most likely mainly due to a changing quality of tip-surface junction under otherwise same conditions - NCD films rich in sp^2 (about 60% relative content) employed in this study were able to retain the high enough potential contrast and consequently induce the self-assembly process. This opens prospects for applications of diamond and its unique set of properties in self-assembly of nano-devices and nano-systems.

Abbreviations

AFM: atomic force microscopy; KFM: Kelvin force microscopy; NCD: nanocrystalline diamond; RMS: root-mean-square; SEM: scanning electron microscopy.

Acknowledgements

We would like to acknowledge the kind assistance of Z. Poláčková with surface oxidation, J. Potměšil with NCD deposition, K. Hruška with SEM imaging, and K. Vyborny with ellipsometry. This research was financially supported by research projects KAN400100701 (GAAV), LC06040 (MŠMT), LC510 (MŠMT), 202/09/H0041, SVV-2010-261307, AV0Z10100521, and the Fellowship J.E. Purkyně (ASCR).

Authors' contributions

EV carried out the AFM/KFM measurements, performed the charging/self-assembly and drafted the manuscript. AK performed the nucleation and deposition of the NCD thin films. ML performed the Raman measurements. JČ participated in the optimization of the AFM/KFM methodology. BR conceived the study, participated in its design and coordination and edited the manuscript.

Competing interests

The authors declare that they have no competing interests.

Received: 30 September 2010 Accepted: 14 February 2011
Published: 14 February 2011

References

1. Fudouzi H, Kobayashi M, Shinya N: **"Site-controlled deposition of microsized particles using an electrostatic assembly".** *Adv Mater* 2002, **14**:1649.
2. Wright W, Chetwynd D: **"Can charge writing aid nanotechnological manipulation?".** *Nanotechnology* 1998, **9**:133.
3. Mesquida P, Stemmer A: **"Attaching silica nanoparticles from suspension onto surface charge patterns generated by a conductive atomic force microscope tip".** *Adv Mater* 2001, **13**:1395.
4. Jacobs H, Stemmer A: **"Measuring and modifying the electric surface potential distribution on a nanometre scale: a powerful tool in science and technology".** *Surf Interface Anal* 1999, **27**:361.
5. Rezek B, Mates T, Stuchlík J, Kočka J, Stemmer A: **"Charge storage in undoped hydrogenated amorphous silicon by ambient atomic force microscopy".** *Appl Phys Lett* 2003, **83**:1764.
6. Naujoks N, Stemmer A: **"Micro- and nanoxerography in liquids - controlling pattern definition".** *Microelectron Eng* 2005, **78/79**:331.

7. Rezek B, Shin D, Watanabe H, Nebel CE: **"Intrinsic hydrogen-terminated diamond as ion-sensitive field effect transistor".** *Sens Actuators B* 2007, **122**:596.
8. Rezek B, Shin D, Uetsuka H, Nebel CE: **"Microscopic diagnostics of DNA molecules on mono-crystalline diamond".** *Phys Status Solidi A* 2007, **204**:2888.
9. Kalbacova M, Kalbac M, Dunsch L, Kromka A, Vaněček M, Rezek B, Hempel U, Kmoch S: **"The effect of SWCNT and nano-diamond films on human osteoblast cells".** *Phys Status Solidi B* 2007, **244**:4356.
10. Kromka A, Rezek B, Remeš Z, Michalka M, Ledinský M, Zemek J, Potměšil J, Vaněček M: **"Formation of continuous nanocrystalline diamond layers on glass and silicon at low temperatures".** *Chem Vap Deposition* 2008, **14**:181.
11. Nebel CE: **"Semiconductor materials: From gemstone to semiconductor".** *Nat Mater* 2003, **2**:431.
12. Koizumi S, Kamo M, Sato Y, Ozaki H, Inuzuka T: **"Growth and characterization of phosphorous doped {111} homoepitaxial diamond thin films".** *Appl Phys Lett* 1997, **71**:1065.
13. Chakrapani V, Angus JC, Anderson AB, Wolter SD, Stoner BR, Sumanasekera GU: **"Charge transfer equilibria between diamond and an aqueous oxygen electrochemical redox couple".** *Science* 2007, **318**:1424.
14. Nebel CE, Rezek B, Shin D, Watanabe H, Yamamoto T: **"Electronic properties of H-terminated diamond in electrolyte solutions".** *J Appl Phys* 2006, **99**:033711.
15. Bergonzo P, Tromson D, Mer C: **"Radiation detection devices made from CVD diamond".** *Semicond Sci Technol* 2003, **18**:S105.
16. Koide Y, Liao M, Alvarez J: **"Thermally stable solar-blind diamond UV photodetector".** *Diamond Relat Mater* 2006, **15**:1962.
17. Stallhofer M, Seifert M, Hauf MV, Abstreiter G, Stutzmann M, Garrido JA, Holleitner AW: **"Photoconductance of a submicron oxidized line in surface conductive single crystalline diamond".** *Appl Phys Lett* 2010, **97**:111107.
18. Sumikawa Y, Banno T, Kobayashi K, Itoh Y, Umezawa H, Kawarada H: **"Memory effect of diamond in-plane-gated field-effect transistors".** *Appl Phys Lett* 2004, **85**:139.
19. Čermák J, Kromka A, Rezek B: **"Electrical characterization of locally charged oxidized nanocrystalline diamond films by Kelvin force microscopy".** *Phys Status Solidi A* 2008, **205**:2136.
20. Verveniotis E, Čermák J, Kromka A, Rezek B: **"AFM induced electrostatic charging of nanocrystalline diamond on silicon".** *Phys Status Solidi B* 2009, **246**:2798.
21. Verveniotis E, Čermák J, Kromka A, Ledinský M, Remeš Z, Rezek B: **"Local electrostatic charging differences of sub-100 nm nanocrystalline diamond films".** *Phys Status Solidi A* 2010, **207**:2040.
22. Rezek B, Michalíková L, Ukraintsev E, Kromka A, Kalbacova M: **Micro-pattern guided adhesion of osteoblasts on diamond surfaces".** *Sensors* 2009, **9**:3549.
23. Rezek B, Nebel CE: **"Kelvin force microscopy on diamond surfaces and devices".** *Diamond Relat Mater* 2005, **14**:466.
24. Kozak H, Kromka A, Ledinsky M, Rezek B: **"Enhancing nanocrystalline diamond surface conductivity by deposition temperature and chemical post-processing".** *Phys Status Solidi A* 2009, **206**:276.
25. Bartošík M, Škoda D, Tomanec O, Kalousek R, Jánský P, Zlámal J, Spousta J, Dub P, Šikola T: **"Role of humidity in local anodic oxidation: A study of water condensation and electric field distribution".** *Phys Rev B* 2009, **79**:195406.
26. Singh R, Arora SK, Tyagi R, Agarwal SK, Kanjila D: **"Temperature dependence of current-voltage characteristics of Au/n-GaAs epitaxial Schottky diode".** *Bull Mater Sci* 2000, **23**:471.
27. Rezek B, Stuchlík J, Fejfar A, Kočka J: **"Microcrystalline silicon thin films studied by atomic force microscopy with electrical current detection".** *J Appl Phys* 2002, **92**:587.
28. Häfliger D, Plitzko J, Hillenbrand R: **"Contrast and scattering efficiency of scattering-type near-field optical probes".** *Appl Phys Lett* 2004, **85**:4466.
29. Verveniotis E, Rezek B, Šípek E, Stuchlik J, Kočka J: **"Role of current profiles and atomic force microscope tips on local electric crystallization of amorphous silicon".** *Thin Solid Films* 2010, **518**:5965.

doi:10.1186/1556-276X-6-144
Cite this article as: Verveniotis *et al.*: Guided assembly of nanoparticles on electrostatically charged nanocrystalline diamond thin films. *Nanoscale Research Letters* 2011 **6**:144.

Submit your manuscript to a SpringerOpen journal and benefit from:

► Convenient online submission
► Rigorous peer review
► Immediate publication on acceptance
► Open access: articles freely available online
► High visibility within the field
► Retaining the copyright to your article

Submit your next manuscript at ► springeropen.com

3.1.4 Detailed study of NCD electronic properties in the nanoscale

In the article "How nanocrystalline diamond films become charged in nanoscale" [81] we investigate the structural and electrical properties of NCD films in the nanoscale in order to resolve the origins of the charge variations. We found that the electrical current during charging flows mainly through the grain boundaries. Detailed KFM measurements revealed that the induced charge is localized predominantly in the grain boundaries. Micro-Raman mapping performed with a smaller laser spot size (400 nm) and SEM cross sections showed that the material is not as homogeneous as shown before [42, 80] by UV-Raman (2 μm spot size) and top-view SEM. Nevertheless, the tip-surface junction is identified once more as the main reason behind the potential variation as also corroborated by macroscopic *I/V* characteristics.

Diamond & Related Materials 24 (2012) 39–43

Contents lists available at SciVerse ScienceDirect

Diamond & Related Materials

journal homepage: www.elsevier.com/locate/diamond

How nanocrystalline diamond films become charged in nanoscale ☆

E. Verveniotis *, A. Kromka, M. Ledinský, B. Rezek

Institute of Physics ASCR, Cukrovarnicka 10, 16253, Prague 6, Czech Republic

ARTICLE INFO

Available online 7 October 2011

Keywords:
Nanocrystalline diamond
Local electrostatic charging
Kelvin Force Microscopy
Current-Sensing Atomic Force Microscopy
Scanning Electron Microscopy
Nanoparticle assembly
Raman mapping

ABSTRACT

Electrostatic charging of oxygen-terminated nanocrystalline diamond (NCD) thin films deposited on silicon in sub-100 nm thickness and with intentionally high relative sp^2 phase ratio (60%) is characterized on a microscopic level. By correlating Kelvin Force Microscopy, Current-Sensing Atomic Force Microscopy, micro-Raman spectroscopy and cross-sectional Scanning Electron Microscopy data we show that the charging is determined by both the surface topography (grains and grain boundaries) and complex sub-surface morphology (arrangement of grains and sp^2 phase) on scales below $2\times2\ \mu m^2$. These microscopic data and macroscopic *I(V)* characteristics evidence that sp^2 phase dominates over diamond grains in local electrostatic charging of NCD thin films. Moreover, the tip-surface junction quality is identified as the main factor behind large variations (0.1 to 1 V) of the overall induced electrostatic charge contrast.

© 2011 Elsevier B.V. All rights reserved.

1. Introduction

Surface conductivity observed in H-diamond attracted considerable interest and research effort in the past [1]. However, research on electronic properties of highly resistive oxygen-terminated intrinsic diamond (O-diamond) has been limited mostly to applications in radiation detectors [2], UV detectors [3], or field-effect transistors [4, 5]. As regards local and intentional electrostatic charging, both positive and negative persistent potential changes were observed on nanocrystalline diamond (NCD) [6], unlike in a-Si thin films [7]. This has been attributed to the capacitor-like behavior of the NCD films [6]. Slight charge decay observed 16 h after charging experiments was attributed to an ambient effect since its magnitude per polarity is exactly the same on NCD [6] and bulk monocrystalline Si films [8]. Comparing charging of NCD films prepared on gold [6] and silicon [8] substrates demonstrated that the charging is not due to the substrate itself as could be argued in the case of silicon substrates. The charging has been also shown to be more effective when the NCD films contain more sp^2 phase [9]. Yet maximal induced electrostatic potential contrast has been reported to be varying by up to 2 V depending to the position on a sample [10]. This may depend on the local material properties as well as actual tip condition. Such potential variation represents a bottleneck towards successful electrostatically driven assembly of nanoparticles on the charged features, as the potential contrast needed for the assembly on NCD is $\geq\pm1$ V [10].

In this paper, we employed the same type of NCD film as previously used for guided assembly of nanoparticles [10] in order to identify the main factors behind the observed potential variations. To this end, we examine local current maps at various spots on the film, compare them with macroscopic data, analyze electrical potentials in charged features with high spatial resolution and investigate local material composition by micro-Raman mapping.

2. Materials and methods

NCD films were prepared by microwave plasma chemical vapor deposition. Microwave plasma power was 900 W and CH_4:H_2 dilution 3:300 sccm. Deposition temperature was 820 °C. The substrates were conductive p-doped silicon wafers nucleated by water-dispersed detonation diamond powder of 5 nm nominal particle size (NanoAmando, New Metals and Chemicals Corp. Ltd., Kyobashi) using an ultrasonic treatment for 40 min. After deposition, the diamond films were oxidized in r.f. oxygen plasma (300 W, 3 min) [11]. UV μ-Raman spectroscopy showed 60% relative sp^2 phase content in the films [10].

Localized charging was performed by scanning in contact mode with an atomic force microscope (N-TEGRA system by NT-MDT). Conductive, diamond coated silicon probes were used (DCP11 by NT-MDT). Applied contact forces were ~100–500 nN. The bias voltage was applied to the tip while the silicon substrates were grounded. The applied voltage range was within ±25 V (the potential contrast is saturated at these voltages [8]). Scan rate during charging was 0.5 Hz. Kelvin Force microscopy (KFM) was then used to detect potential differences across the sample [12] using the same tip. Lift off height for all KFM measurements and scan rate were +10 nm and 0.5 Hz, respectively.

Local current maps were obtained by Current-Sensing Atomic Force Microscopy (CS-AFM). CS-AFM was realized by scanning in

☆ Presented at NDNC 2011, the 5th International Conference on New Diamond and Nano Carbons, Suzhou, China.

* Corresponding author. Tel.: +420 220 318 519; fax: +420 220 318 468.
E-mail address: verven@fzu.cz (E. Verveniotis).

0925-9635/$ – see front matter © 2011 Elsevier B.V. All rights reserved.
doi:10.1016/j.diamond.2011.10.002

contact mode with the AFM described above while applying voltages within the range of ±10 V. The voltage is applied on the Si substrate and the generated electrical current through the film thickness is collected by the tip in contact with the surface. Scan rate was always 0.5 Hz. DCP11 tips were employed for these measurements with contact forces typically ~100 nN. Range of the pre-amplifier used to detect currents was 50 fA–100 pA. Relative humidity and temperature during all AFM experiments were in the range of 25–46% and 23–28 °C, respectively. Macroscopic current–voltage (*I(V)*) characteristics were measured by employing a biased spring micro-contact (<<mm area) in touch with the diamond, while the substrate was grounded.

Cross-sectional morphology of the samples was observed by Scanning Electron Microscopy (SEM). For this purpose the samples were broken and SEM was measured (eLine by Raith, secondary electron detector, accelerating voltage 10 kV, working distance 8 mm) with the sample tilted by 90°.

Micro-Raman mapping (inVia Reflex by Renishaw) was employed for material composition analysis within microscopic areas (HeCd laser, λ = 442 nm, spot diameter 400 nm). The signal is obtained from the whole sample thickness as the NCD films are transparent at this excitation wavelength (theoretical characterization depth ~1 μm).

3. Results

Fig. 1 shows typical KFM images of patterns charged with (a) −25 V and (c) 25 V. The dimensions of the cross arms are 10×80 μm. Maximum amplitude of the charged patterns is 1.2 V (average ~1 V) in each polarity. It is noticeable that the induced charge is not homogeneous within the charged areas. The centers of the crosses show slightly higher potential compared to the rest because they were charged twice (horizontally and vertically). The potential is not double, though, since the charging exhibits saturation as reported before [8]. On the other hand, the top arm of the cross in Fig. 1 (a) and a small area in the left arm (near the center of the cross) exhibit up to double electric potential compared to the rest of the charged features (1.2 V vs. 0.6 V). In addition, we can see several weakly charged areas in the right arm. Similarly, in the cross charged with positive voltage [Fig. 1 (c)] we can identify brighter (e. g. top left region) and darker (bottom cross arm) areas indicating non-homogeneous charging as well. Note that tip instability during KFM resulted in not obtaining the full image here. Charge profiles in Fig. 1 (b, d) are taken along the horizontal arms of the crosses. The electric potential fluctuates in both cases. The variation is more pronounced on the negatively charged cross (−0.8 V vs. 0.25 V).

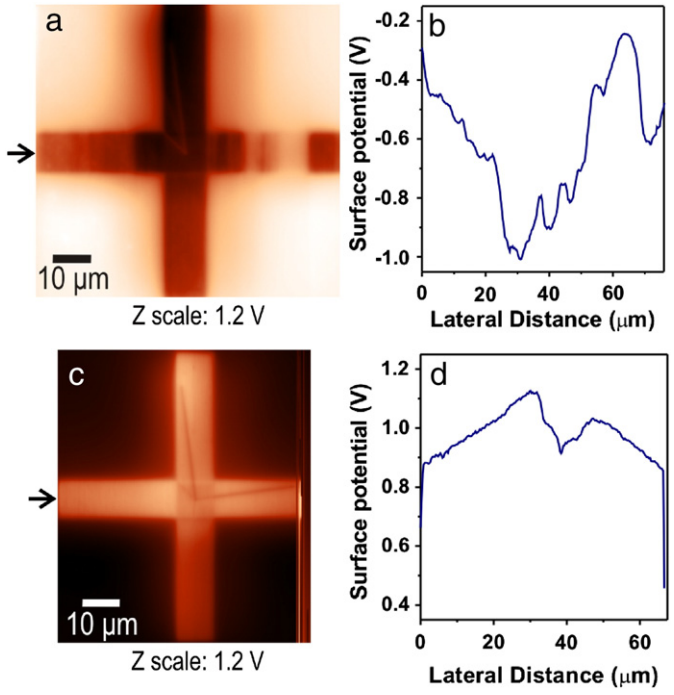

Fig. 1. KFM images of electrostatically charged cross-like patterns on the nanocrystalline diamond thin film using (a) −25 V and (b) 25 V. (b, d) The spatial profiles of the potential across the charged patterns as indicated by arrows next to the KFM images. They are measured in perpendicular to the charging direction (charge scan along the y-axis with slow scan direction from left to right).

In Fig. 2 we can see detailed regions (4×4 μm^2) charged with +25 V (a) and −25 V (d). Area of KFM images (6×6 μm^2) is somewhat larger than the charged regions for comparison with the uncharged vicinity. Overall potential contrast of the two charged regions compared to the surroundings is very similar (180 mV vs. −210 mV). However, charging does not appear homogeneous within the exposed areas. Even more detailed KFM images (2×2 μm^2) from inside of the charged areas are shown in Fig. 2 (b, e). Corresponding surface topography is shown in Fig. 2 (c, f). The potential contrast within the charged regions is up to 60 mV and −80 mV, respectively. The induced charge is mostly localized in the grain boundary regions irrespective of the polarity. In addition, there are also larger patches with higher potential contrast that does not correlate with surface morphology. Note that we did not notice any influence of the local electrostatic charge on the AFM topography either in contact or tapping mode. This is unlike in a previous report where the electrostatic charge of quantum dots clearly influenced the surface topography [13].

Fig. 3 shows the CS-AFM maps at the same magnification as the detailed KFM maps (2×2 μm^2) measured for the positive [Fig. 3 (a, b)] and the negative [Fig. 3 (d, e)] bias voltage polarity simultaneously with the corresponding topography. The bias voltage was ±10 V which was the minimum needed to facilitate stable current mapping on the oxidized NCD sample. Voltage is applied during contact mode AFM scan, while scanning horizontally and with slow scan direction from the bottom to the top. In both cases we can see that the topographical features were reproduced in the current maps. The grain boundaries exhibit always higher conductivity than the grains irrespective of the voltage polarity. The maps obtained with positive voltage appear better defined. In both CS-AFM images there are also features (or areas) that exhibited high current not correlated with the surface topography, similarly with the detailed KFM maps described in Fig. 2. This effect is more pronounced in the positively biased image.

In Fig. 3 (c, f) we can see the histograms of currents obtained from three different CS-AFM images measured across macroscopically separated areas on the NCD sample, using the same experimental parameters. Curves marked as "Spot1" correspond to the current map on the left of the graph. The CS-AFM images from which we derived the curves of Spot2 and Spot3 are qualitatively similar to the Spot1. However, the histogram profiles vary at these different sample areas. In the negative polarity their width and maximum current amplitude differs even though the position (current value) of the peaks is almost identical. In the positive polarity each histogram exhibits different amplitude and position of the peak. The overall distribution broadens as the value of current at the histogram peak increases.

Macroscopic current–voltage characteristics of the film plotted in linear and semi-log scale are shown in Fig. 4. The characteristics were measured on macroscopically separated areas across the sample. Based on the linear graph we can see that they are quantitatively very different. In addition, the semi-log plot indicates that the difference is 1–2 orders of magnitude all along the applied voltage range and that there is always some current for every voltage value. The current values at zero bias are under the detection limit (~100 fA).

In order to understand the factors behind the observed spatial fluctuations of potential and current we have measured SEM on the

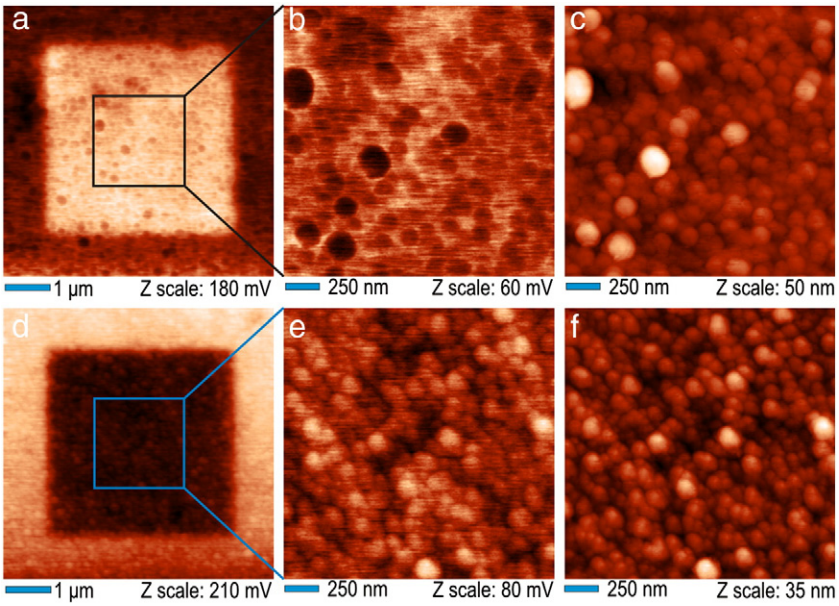

Fig. 2. (a, d) KFM of $4\times4\ \mu m^2$ squares charged with ±25 V. (b, e) Detailed KFM images in the charged regions on the left, in the areas indicated by the $2\times2\ \mu m^2$ squares. (c, f) AFM surface topography corresponding to the detailed KFM images.

cross section of the sample. The SEM image shown in Fig. 5 reveals complex microscopic morphology in the volume of the ultra-thin NCD film. Grain growth patterns are visible. One can see clusters of smaller crystals as well as bigger, triangular grains extending from the Si-NCD interface to the NCD surface. Such micro-structure is similar to the morphology of NCD films used for ultrafast spectroscopy studies where a model involving grains, their surface, and intergrain regions with graphitic and trans-polyacetylene sp^2 carbon species has been proposed [14].

Spatially resolved variations of relative sp^2 phase fraction within our films are shown in the micro-Raman map in Fig. 6. Each pixel is $100\times100\ nm^2$ and corresponds to the relative sp^2 ratio that is calculated as $I_{sp2}/(I_{sp2}+I_{sp3})$ from the respective Raman peak intensities. The map reveals variations in the material composition in a $2\times2\ \mu m^2$ area as the relative sp^2 ratio varies up to 12%. These variations were not obvious when measuring Raman spectra with UV light [10] across the sample since the larger focal point (2 μm) averaged them out and indicated differences of only up to 2% across the film. Furthermore, there is no correlation between the Raman map and surface topography of the film. Taking into consideration the transparency of our NCD films at the Raman excitation wavelength, the signal is obtained from the whole NCD thickness as evidenced also by the pronounced Si peak in the spectrum in Ref [10]. The Raman setup is thus not sensitive enough for surface only changes [15]. Moreover, the Raman focus used for the mapping (400 nm) is still much larger than the typical NCD grains. Hence the Raman map

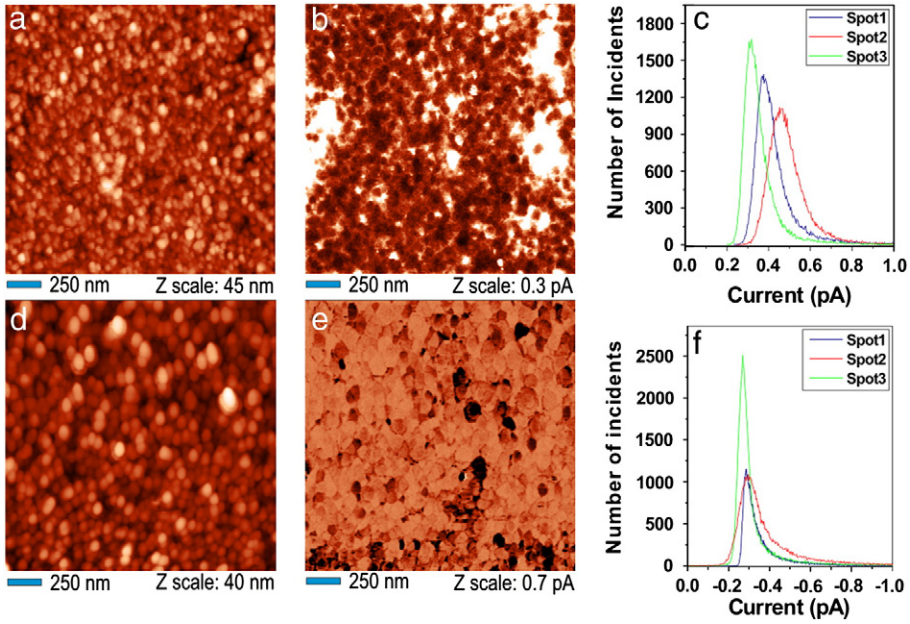

Fig. 3. (a, d) Detailed AFM topography images of the thin film and (b, e) their corresponding CS-AFM maps. (c, f) Histograms of currents for the positive and negative polarity obtained from CS-AFM maps at various spots on the sample. Histograms denoted as "Spot1" correspond to the current maps shown here.

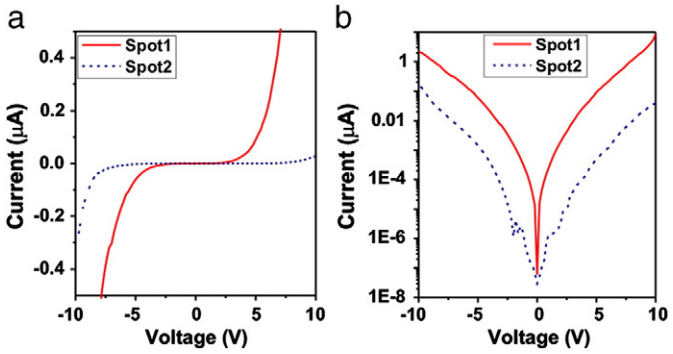

Fig. 4. (a) Current–voltage characteristics measured macroscopically by using a biased spring contact on the NCD sample. (b) The same measurements plotted in semi-log scale. Each curve corresponds to a different spot on the sample.

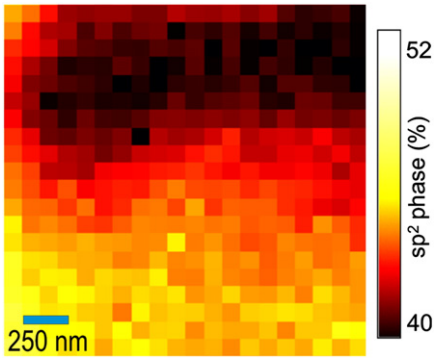

Fig. 6. Raman map of a $2\times2\ \mu m^2$ area of the NCD film showing spatial distribution of relative sp^2 phase fraction.

reflects rather a complex sub-surface morphology of the employed NCD film, in agreement with the cross-sectional SEM image in Fig. 5.

4. Discussion

Variations in the absolute potential have already been reported when NCD was being charged in various, macroscopically separated areas [10]. However, the charged features in Fig. 1 show a variation in the induced potential within one charging experiment. This is the most pronounced on the horizontal cross arm in Fig. 1 (a) where on the right side the film appears weakly charged. In the very end of the scan, though, the high contrast returns. Taking into consideration that the tip never lost contact with the sample (even though there were some fluctuations in the contact quality, based on corresponding AFM topography evaluation) it indicates that the charging efficiency changed abruptly between neighboring scan lines which are separated by 300 nm. Such abrupt variation in the potential contrast must be due to changes in the tip-surface junction properties.

On the other hand, the detailed potential maps shown in Fig. 2 (b, e) confirm the importance of sp^2 to charging [9]. The contrast within the charged regions seen in the detailed KFM maps of Fig. 2 (b, e) (60 mV and −80 mV, respectively) is up to 40% of the overall induced potential contrast between the exposed regions and the uncharged background as evidenced by the KFM maps of Fig. 2 (a, d) (180 mV and −210 mV, respectively). Furthermore, the grain boundary regions (containing sp^2), together with areas exhibiting higher charge (not correlated with the morphology) are charged more efficiently in both polarities (darker colors in the negative and brighter in the positive images indicate higher potential). This is why the negatively charged KFM is practically a mirror image of the topography while its positively charged counterpart looks like a "negative image" of its corresponding topography. The above are also observed in the uncharged regions of Fig. 2 (a, d), indicating that the vicinity of the exposed areas is somehow affected by charging as well. On pristine surface, KFM images resemble those in Fig. 2 (e), albeit with lower contrast of 50 mV. Note that AFM tip shape plays crucial role in obtaining KFM images with high spatial resolution as shown above. Previously reported homogeneity of charging across the grains [8] was influenced by degradation of the tip sharpness during charging.

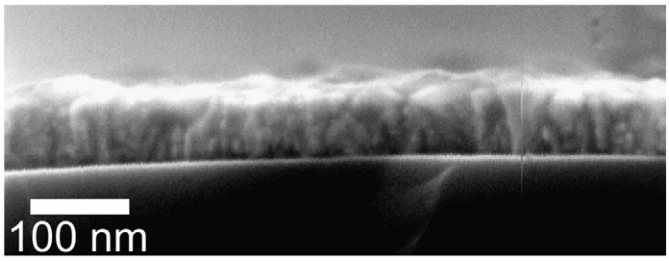

Fig. 5. SEM image of cross-sectional morphology of the NCD thin film.

KFM images correlate well with CS-AFM maps. Features with higher/lower potential contrast correspond to similar features with higher/lower current. Local features in potential and current that are not correlated with surface morphology are most likely due to inhomogeneous and complex microscopic morphology of the NCD film volume as evidenced by cross-sectional SEM and micro-Raman mapping of the relative sp^2 spatial distribution.

Having a closer look at the histograms we can see that the local currents can vary not only locally within one scan frame (histogram width) but also at different spots on the same sample. Such quantitative variations in electrical current may produce differently charged patterns in terms of amplitude.

The macroscopic *I (V)* curves in Fig. 4 (a) confirm what we have seen microscopically. The conductivity changes depending on the measurement spot on the sample. Thus different charging current is generated for the same value of voltage. When the same *I(V)* curves are plotted in semi-log scale [see Fig. 4 (b)] we can see that current is continuous in the whole voltage range. The kink seen in the semi-log curve of Spot2 is most likely due to detrapping from some defect states [16, 17] and is not visible in Spot1 probably due to the larger overall current amplitude. Since intrinsic diamond is an insulator, one would expect to see a gap in the semi-log graphs. The characteristic must be thus attributed to the conductive sp^2 phase (relative sp^2 ratio is 60% in our NCD film as measured by UV micro-Raman). Critically, one should also consider that in our ultra-thin nanocrystalline films the spring contact could have scratched the film. This could decrease effective film thickness, increase contact area or even bring the spring electrode in contact with the Si substrate. In all cases the current amplitude would be larger compared to other measurements employing the full film thickness. Yet CS-AFM histograms support the assertion that the current amplitude variations across the sample are real.

Although micro-Raman mapping reveal local variations in the material composition (12%) and CS-AFM reveals variations in local conductivity, the differences in current amplitude at various spots cannot be due to a film inhomogeneity on macroscopic scale because on average the morphology as well as UV-Raman spectra are uniform across the film [10]. Hence the overall current fluctuations are mainly related with the tip-surface contact quality. In-situ changes in the tip–surface junction can occur for several reasons. First, effective contact area is not constant while the tip scans corrugated surfaces [18] as it becomes duller. An increase in the contact area affects the current path and decreases the applied electric field locally which can influence the current amplitude [18]. This effect would not lead to abrupt changes on large scale patterns though. Second, small dimensions and loading force of the tip–surface contact make it naturally noisier and

less stable [18]. To test this effect we charged several stripes in a single frame while increasing the loading force (100–500 nN). No difference in the induced potential contrast was detected. Third, ambient effects (relative humidity and temperature variations) could also influence the quality of contact. However, pronounced charging variations were observed even under stable conditions within few hours [10]. Last, abrasion of the tip conductive coating (be it a metal or doped diamond) could bring the sample in contact with residual oxide on the silicon bulk of the tip, hereby reducing the potential applied on the diamond sample. After the oxide is also abraded, charging becomes more efficient again as seen in Fig. 1. We think that this is the most plausible reason, yet true nature of the tip–surface contact variations still remains to be elucidated.

Based on KFM and CS-AFM correlations, it is the electrical current that plays dominant role in NCD charging and not polarization effects as suggested earlier [6]. The local microscopic inhomogeneities in the NCD samples (as evidenced by SEM cross sections and μ-Raman map) can influence the detailed profiles of the charged regions (as demonstrated also by detailed CS-AFM and KFM maps). Nevertheless, the most pronounced effect comes from the fluctuations of the tip–surface junction quality during the charging process. Considering that we charge with constant voltage [8–10], the charging current which provides the main contribution to the process can vary greatly due to these fluctuations.

The above effects may be avoided by changing the charging procedure so that constant current is applied while voltage varies according to the local film properties and actual tip–surface junction quality. On the nanoscale, though, applying constant currents may result in unwanted problems with parasitic capacitances [19]. Furthermore, one has to consider influence of field-enhanced de-trapping of charge carriers [20].

An interesting aspect would be comparison of O-NCD electrostatic charging with H-NCD. However, H-NCD has not been characterized for charging so far due to several reasons which make the two systems hardly comparable. Hydrogenating the sample introduces the well-known effect of surface conductivity. This would cause lateral dissipation of the current due to the higher conductivity of the surface compared to bulk diamond and sp^2 phase [21] (i.e. the system would behave as if it had metallic contact on top) which would not result in the desired localized charging. In addition, applying positive voltage on H-NCD would lead to local anodic oxidation making the experiment ill-defined.

5. Conclusions

By correlating KFM, CS-AFM, micro-Raman spectroscopy and cross-sectional SEM data we showed that the local electrical behavior of ultrathin NCD films is determined by both the surface topography (grains and grain boundaries) and complex sub-surface morphology (arrangement of grains and sp^2 phase) on scales below $2\times2\ \mu m^2$. These microscopic data and macroscopic *I(V)* characteristics evidenced that sp^2 phase dominates over diamond grains in local electrostatic charging of NCD thin films. Nevertheless, the tip–surface junction quality during charging was identified as the main factor behind large variations of overall induced electrostatic charge contrast. These results shed some light on the mechanism of the local electrostatic charging of diamond. They may help to better understand electronic transport in NCD, control the charging process, and increase the yield and quality of electrostatically guided self-assembly on diamond.

Acknowledgements

We would like to acknowledge the kind assistance of Z. Poláčková with surface oxidation, J. Potměšil with NCD deposition, K. Hruška with SEM imaging and K. Výborný with ellipsometry. This research was financially supported by research projects KAN400100701 (GAAV), 202/09/H0041, SVV-2011-263307, P204/10/0212 (GAČR), LC06040 (MŠMT), LC510 (MŠMT), AV0Z10100521 and the Fellowship J.E. Purkyně (ASCR).

References

[1] C.E. Nebel, B. Rezek, D. Shin, H. Watanabe, T. Yamamoto, J. Appl. Phys. 99 (2006) 033711.
[2] P. Bergonzo, D. Tromson, C. Mer, Semicond. Sci. Technol. 18 (2003) S105.
[3] Y. Koide, M. Liao, J. Alvarez, Diam. Relat. Mater. 15 (2006) 1962.
[4] M. Stallhofer, M. Seifert, M.V. Hauf, G. Abstreiter, M. Stutzmann, J.A. Garrido, A.W. Holleitner, Appl. Phys. Lett. 97 (2010) 111107.
[5] Y. Sumikawa, T. Banno, K. Kobayashi, Y. Itoh, H. Umezawa, H. Kawarada, Appl. Phys. Lett. 85 (2004) 139.
[6] J. Čermák, A. Kromka, B. Rezek, Phys. Status Solidi (a) 205 (2008) 2136.
[7] B. Rezek, T. Mates, J. Stuchlík, J. Kočka, A. Stemmer, Appl. Phys. Lett. 83 (2003) 1764.
[8] E. Verveniotis, J. Čermák, A. Kromka, B. Rezek, Phys. Status Solidi (b) 246 (2009) 2798.
[9] E. Verveniotis, J. Čermák, A. Kromka, M. Ledinský, Z. Remeš, B. Rezek, Phys. Status Solidi (a) 207 (2010) 2040.
[10] E. Verveniotis, A. Kromka, M. Ledinský, J. Čermák, B. Rezek, Nanoscale Res. Lett. 6 (2011) 144.
[11] B. Rezek, L. Michalíková, E. Ukraintsev, A. Kromka, M. Kalbacova, Sensors 9 (2009) 3549.
[12] B. Rezek, C.E. Nebel, Diam. Relat. Mater. 14 (2005) 466.
[13] N. Shimizu, M. Ikeda, E. Yoshida, H. Murakami, S. Miyazaki, M. Hirose, Jpn. J. Appl. Phys. 39 (2000) 2318.
[14] B. Dzurňák, F. Trojánek, J. Preclíková, A. Kromka, B. Rezek, P. Malý, Diam. Relat. Mater. 20 (2011) 1155.
[15] H. Kozak, A. Kromka, E. Ukraintsev, J. Zemek, M. Ledinský, M. Vaněček, B. Rezek, Diam. Relat. Mater. 18 (2009) 722.
[16] Y. Garino, T. Teraji, S. Koizumi, Y. Koide, T. Ito, Phys. Status Solidi (a) 207 (2010) 1460.
[17] T. Makino, K. Yoshino, N. Sakai, K. Uchida, S. Koizumi, H. Kato, D. Takeuchi, M. Ogura, K. Oyama, T. Matsumoto, H. Okushi, S. Yamasaki, Appl. Phys. Lett. 99 (2011) 061110.
[18] B. Rezek, J. Stuchlík, A. Fejfar, J. Kočka, J. Appl. Phys. 92 (2002) 587.
[19] B. Rezek, E. Šípek, M. Ledinský, J. Stuchlík, A. Vetushka, J. Kočka, Nanotechnology 20 (2009) 045302.
[20] M. Rogalla, T. Eich, N. Evans, R. Geppert, R. Goppert, R. Irsigler, J. Ludwig, K. Runge, T. Schmid, D.G. Marder, Nucl. Instrum. Methods A 395 (1997) 49.
[21] P. Hubík, J.J. Mareš, H. Kozak, A. Kromka, B. Rezek, J. Krištofik, D. Kindl, Diam. Relat. Mater. (2011) doi:10.1016/j.diamond.2011.10.021.

3.1.5 Charging NCD by constant current application

Since the tip-surface junction quality was repeatedly identified as the main factor behind the potential contrast variation observed when NCD was charged, we needed to implement a method which would minimize the effects of the varying tip-surface junction quality while charging.

In the article "Persistent microscopic charging of oxidized nanocrystalline diamond by constant currents in atomic force microscope" [98] we employ a secondary AFM feedback while charging. This feedback controls the electrical current with respect to the local structural and electrical properties. As a result, it provides a relatively constant current, thus exposing the work area to the same (or at least similar) number of charge carriers.

This method resulted in more homogeneous charging and reproducible results as evaluated by KFM. In addition, we identified field-enhanced charge detrapping, as the main process due to which we couldn't consistently induce electrical potentials above 1 V. This work also evidenced that the voltage giving rise to the current governs the charging process because it determines the energetic range of traps that is available for charge storage.

Persistent microscopic charging of oxidized nanocrystalline diamond by constant currents in atomic force microscope

E. Verveniotis*, A. Kromka and B. Rezek

Institute of Physics ASCR, Cukrovarnicka 10, Prague 6, Czech Republic

Abstract

Constant electrical current in the range of -1 pA to -200 pA is applied by atomic force microscope (AFM) in contact mode regime to induce and study local electrostatic charging of oxygen-terminated nanocrystalline diamond (NCD) thin films. The NCD films are deposited on silicon in 70-100 nm thickness and with 60% relative sp^2 phase content. Charging current is monitored by conductive AFM. Electric potential contrast induced by the current is evaluated by Kelvin force microscopy (KFM). KFM shows well-defined, homogeneous, and reproducible microscopic patterns that are not influenced by inherent tip-surface junction fluctuations during the charging process. The charged patterns are persistent for at least 72 hours due to charge trapping inside the NCD film. The current induced charging also clearly reveals field-induced detrapping at current amplitudes > -50 pA and tip instability at > -150 pA, both of which limit the achievable potential contrast. In addition, we show that the field also determines the number of electronic states that can trap the charge. We present a model and discuss implications for control of the nanoscale charging process.

1. Introduction

Surface conductivity observed in hydrogen-terminated diamond attracted considerable interest and research effort in the past [1]. Research on electronic properties of highly resistive oxygen-terminated intrinsic diamond (O-diamond) has been so far focused mostly on applications in radiation detectors [2], UV detectors [3], or field-effect transistors [4, 5]. In such applications, electronic transport and charge related effects in diamond are often crucial factors for understanding and optimizing the device function. One way to study these effects is to apply intentional charging of the material.

After local and intentional electrostatic charging, both positive and negative persistent potential patterns were observed on nanocrystalline diamond (NCD) by Kelvin force microscopy (KFM) [6], unlike in silicon thin films [7]. Comparison between charged NCD films prepared on gold [6] and silicon [8] substrates demonstrated that the charging is not due to the substrate itself as could be argued in the case of silicon substrates. The charging has been also shown to be more efficient when the NCD films contain more sp^2 phase [9]. Yet maximal induced electrostatic potential contrast has been reported to vary even on the same sample [10]. In addition, charged patterns were not microscopically homogeneous, showing a variation up to 50 % of the maximum potential. This may depend on the local material properties, charge stability as well as to the tip-surface junction quality.

Previous works employed constant voltage for the local diamond charging [6, 8-11]. However, as conductivity of the NCD samples varies even in the nanoscale due to presence of grains (sp^3 bonded carbon-diamond), grain boundaries (sp^2 bonded carbon-graphite) [9] and complex sub-surface morphology [10, 11] the amount of injected charge was not fixed. Furthermore, changing properties of the tip and thus tip-surface junction during AFM scans of hard surfaces such as diamond represent another problem because the conduction barrier (or current) at a given voltage is altered even during one

* Corresponding author: e-mail: verven@fzu.cz, Phone: +420 220 318 433

experiment. Those are probably the main reasons why the induced potential contrast was not uniform both spatially and in amplitude and also not well reproducible. The variations observed in the outcome of otherwise identical charging experiments represented a bottleneck towards reliable applications [10].

In order to ensure similar exposure conditions and overcome the tip-surface junction-related problems it may be beneficial to charge NCD by using constant current instead of voltage. Implementing such technique in nanoscale, specifically in atomic force microscope (AFM), is experimentally challenging as it requires an additional, fast enough feedback for continuous control of the voltage to maintain the constant electrical current.

In this work we show that this method is indeed feasible, the charging can be better controlled by the applied electrical current, and well-defined uniform microscopic charge patterns can be obtained on NCD thin films. However, we also show that the voltage still plays an important role in generation of the potential contrast. Results after charging are analyzed by evaluation of surface potentials in correlation with electrical current and corresponding voltage maps. We propose a simple model explaining all the above phenomena.

2. Materials and Methods

NCD films were prepared by microwave plasma chemical vapor deposition using the following parameters: substrate temperature 820°C, deposition time 16 minutes, microwave plasma power 900 W, CH_4:H_2 dilution 3:300. Resulting thickness was 70 nm as measured by ellipsometry. The substrates were 5x10 mm^2 conductive p-doped silicon wafers nucleated by water-dispersed detonation diamond powder of 5 nm nominal particle size (NanoAmando, New Metals and Chemicals Corp. Ltd., Kyobashi) using an ultrasonic treatment for 40 min. After deposition the diamond films were oxidized in r.f. oxygen plasma (300 W, 3 min) [12]. Raman spectroscopy showed 60% relative sp^2 phase content in the films when intensity of diamond and graphitic bands were compared [10]. Yet note that the films still exhibit good diamond quality.

Electric current was applied locally by AFM (NTEGRA system by NT-MDT) scanning in contact mode. We used silicon cantilever coated by conductive diamond (DCP11 by NT-MDT) for all measurements. The scan rate was always 0.3 Hz. Applied contact forces were ~100 nN. We used a special AFM regime that enabled constant current application in the range of -1 to -200 pA. Similar results were obtained with positive polarity. The constant current was maintained by a secondary feedback circuit which was fast enough to adjust the applied voltage with respect to local variations of material properties and tip-surface junction quality while scanning the surface. The voltage that maintained such constant currents was within the -50 V range.

Kelvin Force microscopy (KFM) in the 2-pass regime was used on diamond [13] to detect electric potential differences induced by the current application. Lift height in the 2-pass was 10 nm and scan rate was also 0.3 Hz. Relative humidity and temperature during all AFM experiments were in the ranges of 20-32% and 22–26 ^oC.

3. Results

Figure 1 (a) shows three-dimensional representation of the current map obtained during the charging process. In this experiment we used four different current set-point (I_s) values: -1, -2, -3, and -4 pA from bottom to top. The stripes with applied current are separated by regions of the same size where no current was applied (darker, flat stripes in

the image). We can see that the current fluctuates around the set-point rather than being perfectly stable. Magnitude of this fluctuation is increasing at higher set-points both quantitatively (larger current spikes), and qualitatively (more current spikes per stripe). This is clearly demonstrated in Figure 1 (d) where the typical spatial profile of current is plotted. Even though average current matches well with the I_s set-point, the current fluctuations increase with the set-point. Root-mean-square (RMS) of each stripe is 0.13, 0.37, 0.66 and 1.1 pA, respectively. The sharpest current spike observed for the I_s = -1 pA is -1.19 pA (i.e. 19% over I_s) while for I_s = -4 pA it goes up to -5.2 pA (i.e. 30% over I_s).

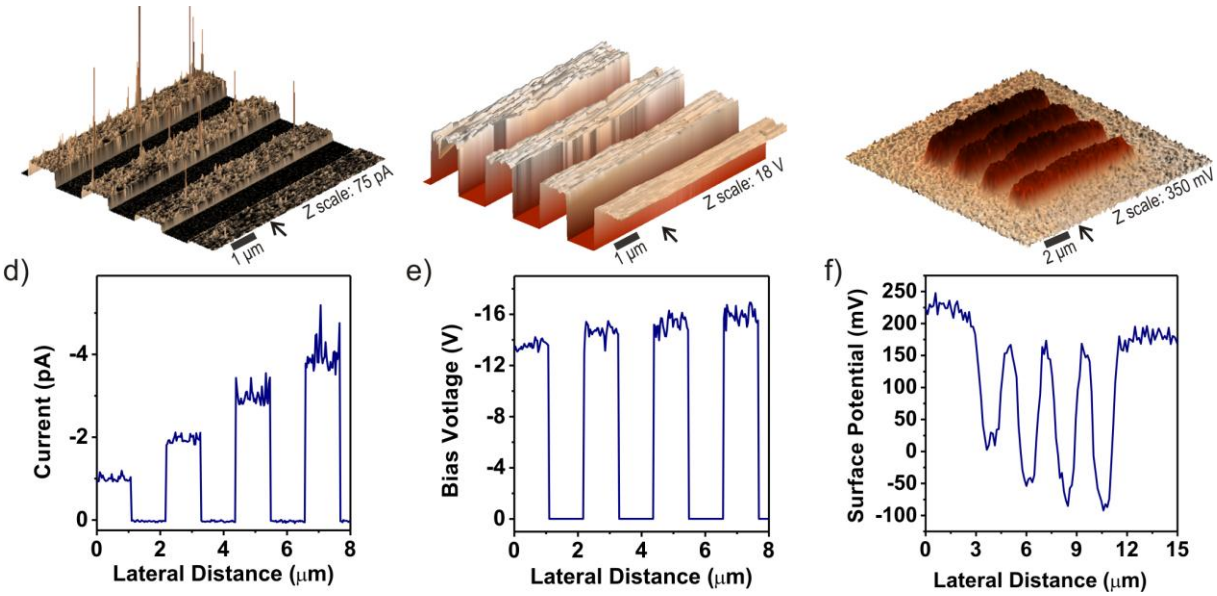

Figure 1 (a) Current, (b) bias voltage and (c) resulting surface potential maps in a regulated current charging experiment with I_s from -1 pA to -4 pA. (d, e, f) Their respective spatial profiles as indicated by the arrows.

Figure 1 (b) shows map of bias voltage corresponding to the applied current in Figure 1 (a). The voltage naturally increases at higher I_s values. In similarity to the current map, voltage fluctuation is somewhat larger with increasing I_s as evidenced by increasing RMS values from each stripe: 0.3, 0.6, 1.0, and 2.9 V. The fluctuation is also visible in the spatial profile of voltage in Figure 1 (e).

The result of the current application on the electrical charging of the NCD films can be seen in the KFM map in Figure 1 (c). First of all, all the applied currents lead to localized change of electric potential of the NCD film. Unlike previous results where constant voltage was applied [10] the charged regions are spatially uniform. Potential fluctuations are up to 80 mV, which is comparable to the original potential background (up to 60 mV). Spatial profile across the potential map [Figure 1 (f)] reveals increasing charge (potential contrast) after every increment of I_s. Nevertheless, the increment is not linear like the current. It should be noted that the current induced charging worked similarly with positive polarity. Thereby opposite potential contrast was achieved, in agreement with previous report on voltage induced charging [10].

Figure 2 shows similar experiment with higher I_s amplitudes. The set-point values were -50, -100, -150, -200 pA from the bottom to the top. In the current map in Figure 2 (a) and the spatial profile in Figure 2 (d) we can see that the electrical current fluctuations are more pronounced as I_s increases, in similarity to the findings of Figure 1. RMS of each stripe in the sequence is 14, 19, 66, and 70 pA, respectively. The sharpest peaks for the first and last value of I_s are at - 82 pA (64% over the set-point) and - 380 pA (90%

over the set-point), respectively. The corresponding bias voltage map and its spatial profile [Figure 2 (b, e)] show that higher current set-point does not always require higher bias voltage: the voltage increases with I_s until roughly the middle of the third stripe in the sequence (I_s = -150 pA). There we can see an abrupt decrease of the bias voltage needed for generation of the same current from -50 V to -30 V. RMS calculated from each stripe in the sequence is 2.1, 2.0, 7.3, and 1.9 V, respectively.

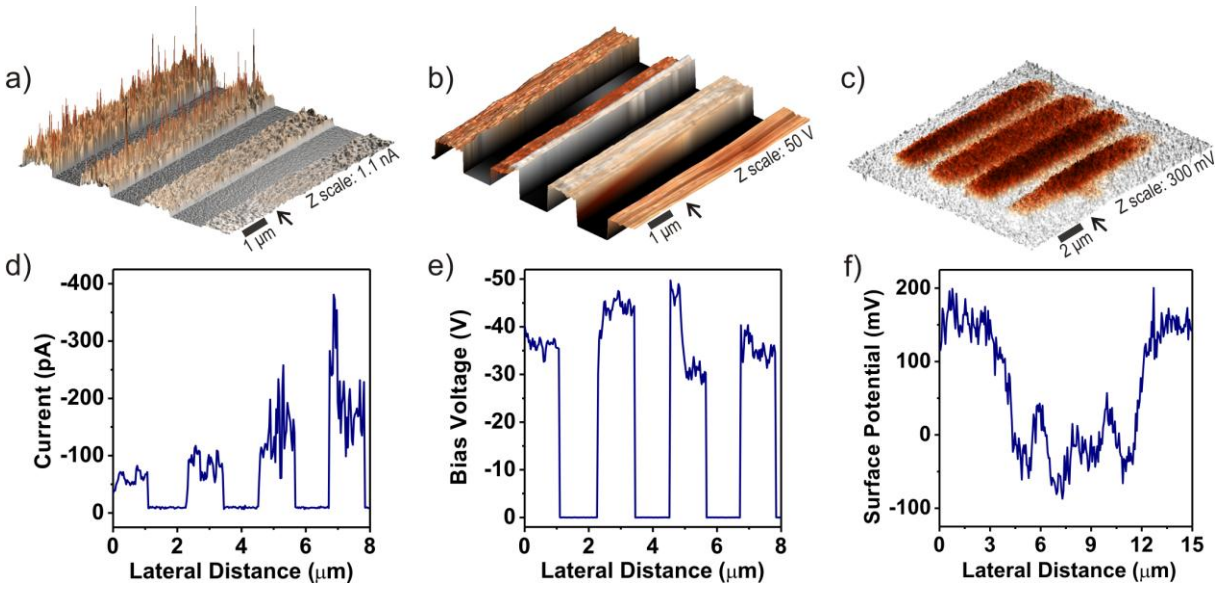

Figure 2 (a) Current, (b) bias voltage and (c) resulting surface potential maps in a regulated current charging experiment with I_s from -50 pA to -200 pA. (d, e, f) Their respective spatial profiles as indicated by the arrows.

Figure 2 (c) shows the electric potential map after the charging experiment with the higher current amplitudes. The charged areas are not homogeneous, neither well confined within the exposed regions. We can identify uncharged areas as well as areas where the vicinity of the exposed regions appears also affected. The corresponding spatial profile of Figure 2 (f) does not reveal any trend between the induced potential and the applied electrical current. The stripes appear weakly charged when compared to their Figure 1 (c) counterparts, with the electric potential intensity declining slightly at the two higher I_s states.

Quantitative evaluation of the potential contrast achieved by current charging is shown in Figure 3. The graph shows average potential contrast values obtained from each individual stripe in Figure 1 (c) and Figure 2 (c) as a function of the constant charging current I_s (blue triangles). The induced potential contrast increases with I_s but the magnitude of the contrast change ΔV is decreasing from -55 mV towards zero (red circles). The data also show that higher current does not necessarily mean higher potential contrast: the stripe charged with -150 pA exhibits lower potential contrast than the stripes charged with -50 pA and -100 pA (-170 mV vs. -175 mV and -185 mV, respectively). The contrast change shows no trend as it fluctuates between +10 and -25 mV.

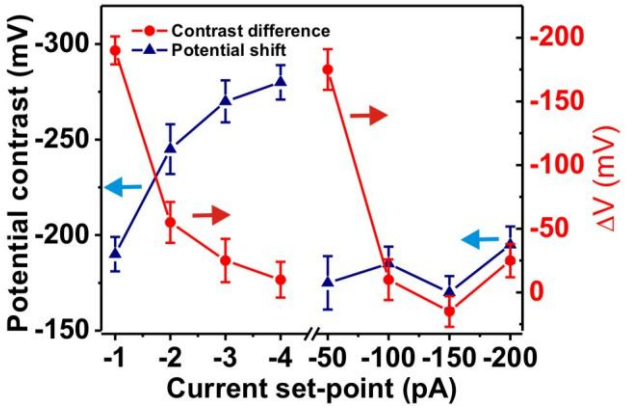

Figure 3 Average surface potential measured from each stripe of Figs. 1 (c). 2 (c) and differences between the induced potential contrast at successive current set-point values. Lines connecting the data points are guide for the eye.

Figure 4 shows the average applied current and voltage with respect to I_s. Each data point corresponds to average value of current (blue squares) and voltage (red inversed triangles) as measured from each individual stripe in Figs. 1 (a), 2 (a) and Figs. 1 (b), 2 (b), respectively. We can see that all the average current values are identical to the employed set-point. Even though the applied current fluctuates and this fluctuation is increasing with I_s (error bars in Figure 4), the average value always matches well the set-point (deviation is < 1%). As regards the voltage associated with the current, it shows a slight increase with I_s in the lower current set-point range. This is because the electrical current in our NCD samples rises exponentially with linear increase of the bias voltage [8, 9]. In the case of higher set-points we can see that the voltage increases up to -47 V until -100 pA are applied. After that it drops to -34 V for -150 pA. Note that I_s = -200 pA required an increase of only -1 V in the bias.

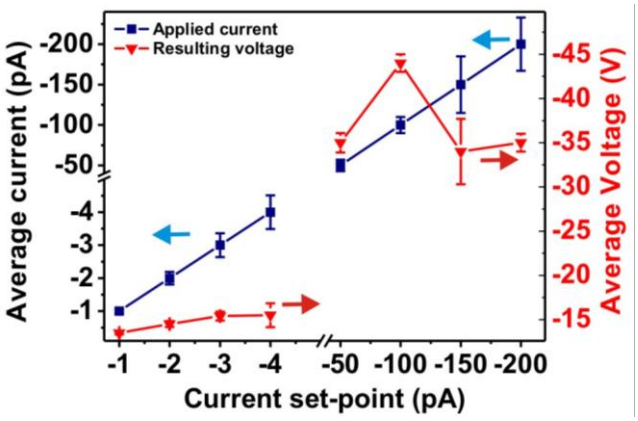

Figure 4 Average electrical current and bias voltage measured from each stripe of Figs. 1 (a, b), 2 (a, b) plotted as a function of the actual current set-point. Lines connecting the data points are guide for the eye.

Figure 5 (a) displays the KFM potential map after multiple constant current charging experiments. Inside each of the four frames there are 4 stripes with I_s from -1 pA to -4 pA from the top to bottom. The difference between the individual frames is the number of times the charging was repeated as indicated by the labels next to each individual frame: the top-right frame was charged once, the top-left twice, the bottom-left three times and

the bottom-right four times. We can see that the electric potential contrast achieved in all charged frames is similar and homogeneous, not showing any dependence on the number of charging processes. This is clearly demonstrated in Figure 5 (b) where we can see a spatial profile measured in the KFM map across all the stripes belonging to the frames that were charged once and four times (arrow on top of the KFM image). We can see similar values for the surface potential which increases sub-linearly with the set-point. Figure 5 (c) shows a spatial profile across the I_s of -3 pA in the frames charged three and four times (arrow on the right of the KFM image). We observe identical values of surface potential on the patterns. Figure 5 (b, c) illustrates also the relaxation of the induced electric potential after 24 h and 72 h. We can see that the charge from all stripes decays similarly, irrespective of I_s or charging count. In addition, the shape of curves measured after 72 h is almost identical to their 24 h counterparts, indicating that the charge which remains within the NCD film after one day is persistent and stable.

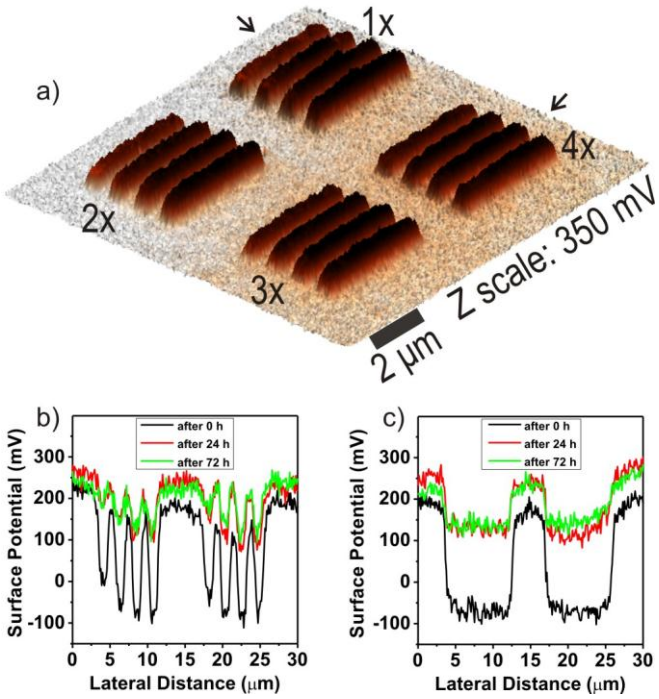

Figure 5 (a) KFM map of four different frames where current charging experiments were performed. Each experiment consisted of 4 stripes where constant currents -1, -2, -3, -4 pA were applied. The experiment was repeated 1x, 2x, 3x, 4x in the particular frame as indicated in the image. (b, c) Spatial profiles indicated by arrows next to the KFM map measured 0 h, 24 h and 72 h after charging.

4. Discussion

The initial model proposed for NCD charging [6] included contributions from charge trapping and polarization. The former was attributed to sp^2 phase and defect states within the material: the more the graphitic content the larger the density of trap states. This means that the trapped charge is a function of the charge carriers introduced to the system, i.e. a function of electrical current. On the other hand, polarization occurs on the highly resistive sp^3 diamond phase. Hence it is a function of the applied field. Previous work

indicated that the induced potential shifts depend mostly, if not only, on the passing current (trapping) rather than the effective electric field (polarization) [11].

By using constant current charging, our results show in a straightforward way that even though the current magnitude is fundamental for NCD charging, the voltage giving rise to the current still plays a significant role. We propose that the bias voltage determines the range of accessible trap states for charge storage as well as the degree of field-induced detrapping of charge in the NCD films. Figure 6 shows a schematic model of the charging mechanism in our system. The relation between energy and density of states (DOS) may be somewhat simplified, nevertheless it illustrates continuous DOS of graphitic materials [14]. For increasing voltage associated with the applied constant current I_s there is obviously larger range and density of available localized states to trap the charge.

However, as also seen from the results, when the bias is higher than the previously reported saturation threshold [8] we don't observe more charge in the film. This is because for voltages above the threshold the field-induce detrapping becomes more pronounced [15] as indicated in the model scheme. In our opinion, the proposed model can explain all the following effects that are evident from the measured data.

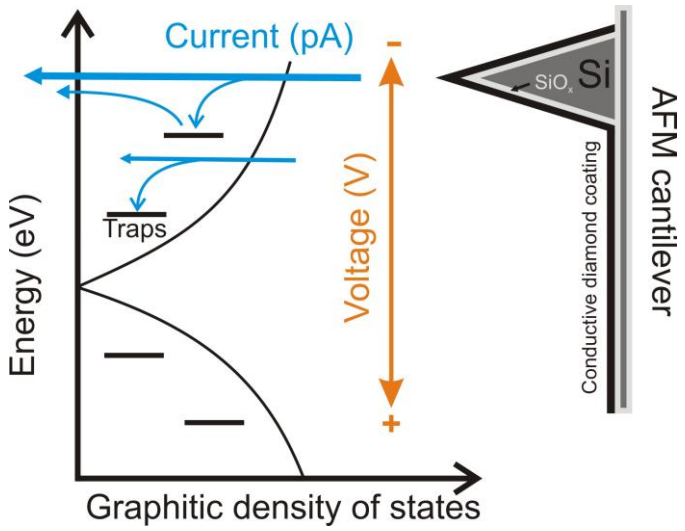

Figure 6 Schematic model of the charge storage mechanism in graphitic states of the NCD thin films.

First of all, the amount of injected charge does increase linearly ($I = Q/t$, where exposure time t is constant) but increase of potential contrast is not proportional to the applied current in both low and high current amplitude range (see Figures 1, 2 and 3). Since the bias voltage increase between I_s = -1 and -4 pA is only -3 V (-13 V to -16 V) the energetic range of the available charge traps does not increase significantly. At higher current amplitudes the potential contrast reaches saturation (ΔV fluctuates around zero) in spite of increasing voltage. This may be attributed to the field-induced detrapping of charge.

Comparing the KFM maps and potential graphs of the two experiments we can see that the charging was more efficient in the low I_s experiment (potential contrast -190 to -280 mV vs. -170 to -195 mV). Similar potential shifts between the -1 pA and -200 pA clearly evidence the pronounced effect of field-induced detrapping as higher currents lead to higher bias voltages (-13 V vs. -35 V). This effect counters both the introduction of more charges to the system (up to 200 times more), and larger range of available trap

states, effectively not allowing the patterning of larger potential contrasts. The detrapping effect can be also strengthened by oxide formation on the tip apex, which adds another conduction barrier to the system, meaning that the voltage has to be further increased to facilitate conduction with a desired value of electrical current.

In addition, it is evident that the amount of stored charge does not change with repeated charging of the same area up to 4 times. This means that after the initial charging we reach some kind of saturation which prohibits the trapping of additional charges when charging with the same current. However this does not correspond to overall system saturation and occurs most likely because there are no more available charge traps in the energy range covered by the bias voltage associated with the I_s range. Since -1 pA to -4 pA of current needs a bias of -13 V to -16 V to be realized (Figure 1), and considering that the system reaches saturation at around -25 V [8], it is possible that if we increased the applied current past the -4 pA mark during the consecutive charges, we would observe higher potential shifts due to charges trapped in deeper energetic states. This behaviour, however, would occur under the condition that the bias voltage generating the applied current would be always kept under the global saturation threshold of -25 V. After that value, the effects of field-induced detrapping overcome the benefit of having more available trap states (due to the larger energy range), leading to less efficient and/or inhomogeneous charging as seen in Figure 2.

Another crucial feature is uniformity of the charging. Figure 5 confirms that the constant current methodology implemented in this work generally improved the reproducibility of charging experiments significantly. This helped overcome the charge variation issue reported before with constant voltage charging [10]. Using lower I_s range resulted in better charging both quantitatively and qualitatively. The charged areas in Figure 1 are better confined within the exposed regions as opposed to Figure 2. This may be attributed to smaller field spreading and thus more localized current flow. The fluctuations within the charged regions are also smaller due to smaller current fluctuations at the lower I_s range.

The increased current fluctuation at higher I_s can be explained by the increased bias used to generate it: as the film consists of conductive graphite (sp^2 phase due to grain boundaries) and insulating diamond (sp^3 phase due to the grains), higher bias produces bigger differences between the current that flows through the grain boundaries and the grains. Since for such NCD films (grain size <100 nm) the AFM tip will encounter numerous transitions between grains and grain boundaries within few tens of msec (scan size 8 μm, scan speed 5 μm/sec), the inherently imperfect feedback controlling the current cannot respond that fast. This is more evident in Figure 2 (a, d) where the current set-points were higher. For the terminal current value of -200 pA, the fluctuation goes as high as two times the I_s (-400pA).

Analysis of Figure 2 (b) indicates also that some kind of tip “forming” can occur at higher bias voltages. Even diamond coated tips are not durable enough for scanning hard NCD samples [11] as the tip coating is scraped off relatively fast, bringing the sample in contact with the underlying silicon. The tip forming is thus most likely due to oxide abrasion on the tip apex which reduces the voltage necessary for driving a given value of current. This is clearly demonstrated in the third stripe of the sequence, where in the beginning it was necessary to apply nearly -50 V to drive -150 pA of current but after few scanlines the bias dropped abruptly to -30 V (I_s was constant). Thus the bias was lower than what we observed for the -50 pA stripe (-30 V vs, -37 V).

The KFM map and the average potential graph of Figure 2 (c, f) show that under such unstable tip-surface junction conditions, higher charging current does not necessarily mean higher induced potential: -150 pA charged less efficiently than -50 and -100 pA. In

addition, -200 pA charged slightly better than all the other I_s states of this experiment but with applied voltage (and thus field) similar the to one applied for I_s = -50 pA. This means that while we were applying four times higher current, the effects of field-induced detrapping (which are pronounced after the saturation threshold of -25 V [8]) were comparable at both -50 and -200 pA.

As for stability of the stored charge, the graphs in Figure 5 show that the charge decay is similar irrespective of the repeated charging. This corroborates well the previous argument of charge saturation in the available energy range since similar decay naturally requires similar qualitative and quantitative charging in each frame. In addition, we can see that after 24 hours the decay has little or no effect on the charged patterns and the charge is stable. It is expected that charges trapped in the surface states will decay faster due to the direct exposure to the atmosphere [6, 8]. We assume that the remaining charge corresponds to the charge trapped inside the NCD film where it is protected by the film itself, thus it remains even three days after charging. Note that charging experiments conducted on thicker NCD films (~1 μm) showed only little detectable charge one hour after charging. In addition, the patterns which were initially quite clear became poorly defined after one hour. Considering well-known averaging effect of KFM this indicates that the detected charge after one hour must be deeper in the sample rather than near the surface.

From the evidence provided in this work it is obvious that constant current charging does not exclude tip-surface junction variations completely. The potential drop on the tip, and thus across the film always varies which has an impact to the charged result. Hence the voltage is still detrimental to the process since it determines both the range of available traps and the field-induced detrapping. It is therefore clear that in order to achieve electric potential shifts over the threshold needed for electrostatically-guided assembly (1 V) we need to further optimize the process. Ideally, it is necessary to introduce as many charge carriers to the system as possible. In addition, the voltage corresponding to the current must not exceed the saturation threshold to limit the effects of field-induced detrapping, while the energy range, and thus number of accessible trap states is as high as possible. Thus for optimal charging, an equilibrium between the range of accessible traps and field induced detrapping, and tip-surface contact stability must be found. This also requires more durable AFM tips (ideally fully diamond) of high conductivity. Such tips would render the experiments more stable as tip-surface junction (and thus applied voltage) fluctuations would be only minor, free of tip forming artefacts, allowing the deliverance of a high electrical current in the -25 V region.

Conclusions

Local electrostatic charging of NCD by constant current application was successfully performed by implementing a secondary feedback controlling the bias voltage while scanning in AFM. This methodology, where the amount of injected charge is under control, solved the reproducibility issues encountered in the previous studies [8-10]. However, we found that increasing the amount of charge introduced to the system (up to 200 times) is not enough to create high potential contrasts. This is due to the pronounced field-induced detrapping at higher applied currents (and thus higher voltages) which counters also the benefit of wider available range of trap states. This work thus shed more light on the NCD charging process mechanism, indicating that the appropriate I_s has to be selected so that the voltage must not exceed the saturation threshold of -25 V.

We also showed that the induced potential contrast corresponds mostly to charges trapped inside the NCD film and which persists at for least 72 hours after charging. Such behaviour opens prospects for real applications based on locally charged NCD. Further experiments on monocrystalline diamond films (no grain boundary contribution) might elucidate more details with regard to the charging mechanism. Usage of highly conductive full diamond tips could be also beneficial as it would eliminate the factor of tip forming, possibly making the tip-surface junction more stable.

Acknowledgements

We would like to acknowledge the kind assistance of Z. Poláčková with surface oxidation, J. Potměšil with NCD deposition and K. Vyborny with ellipsometry. This research was financially supported by research projects P108/12/G108 (GAČR), P108/12/0996 (GAČR), and doctoral project 202/09/H041. This work occurred in frame of the LNSM infrastructure.

References

[1] C. E. Nebel, B. Rezek, D. Shin, H. Watanabe, T. Yamamoto, J. Appl. Phys. 99, 033711 (2006).
[2] P. Bergonzo , D. Tromson and C. Mer, Semicond. Sci. Technol. 18, S105 (2003).
[3] Y. Koide, M. Liao, and J. Alvarez, Diam. Relat. Mater. 15, 1962 (2006).
[4] M. Stallhofer, M. Seifert, M. V. Hauf, G. Abstreiter, M. Stutzmann, J. A. Garrido, and A. W. Holleitner, Appl. Phys. Lett. 97, 111107 (2010).
[5] Y. Sumikawa, T. Banno, K. Kobayashi, Y. Itoh, H. Umezawa, and H. Kawarada, Appl. Phys. Lett. 85, 139 (2004).
[6] J. Čermák, A. Kromka, and B. Rezek, Phys. Stat. Sol. (a) 205, 2136 (2008).
[7] B. Rezek, T. Mates, J. Stuchlík, J. Kočka, and A. Stemmer, Appl. Phys. Lett. 83, 1764 (2003).
[8] E. Verveniotis, J. Čermák, A. Kromka, and B. Rezek., Phys. Stat. Sol. (b) 246, 2798 (2009).
[9] E. Verveniotis, J. Čermák, A. Kromka, M. Ledinský, Z. Remeš and B. Rezek., Phys. Stat. Sol. (a) 207, 2040 (2010).
[10] E. Verveniotis, J. Čermák, A. Kromka, M. Ledinský, and B. Rezek., Nanoscale Res. Lett. 6, 144 (2011).
[11] E. Verveniotis, A. Kromka, M. Ledinský and B. Rezek, Diam. Relat. Mater. 24, 39 (2012)
[12] B. Rezek, L. Michalíková, E. Ukraintsev, A. Kromka and M. Kalbacova, Sensors 9, 3549 (2009)
[13] B. Rezek and C. E. Nebel, Diam. Relat. Mater. 14, 466 (2005).
[14] J.- C. Charlier and J.- P. Michenaud, Phys. Rev. B 46, 4540 (1992)
[15] M. Rogalla, T. Eich, N. Evans, R. Geppert, R. Goppert, R. Irsigler, J. Ludwig, K. Runge, T. Schmid, and D.G. Marder, Nucl. Inst. and Meth A 395, 49 (1997)

3.2 Nanocrystallization of a-Si:H

Previous work by Rezek and coworkers [83, 84] established a new method for crystallizing a-Si:H. It employed AFM in order to scale down FE-MISPC to the micro- or nano-scale. By using the setup illustrated in Figure 2.12 above, Rezek et al. found that they could produce crystallized (and thus conductive) pits or rings in the amorphous tissue. Geometry and size of the induced features (200 nm-3 μm) were found to be dependent on the energy rate supplied to the system. However, electrical current surges due to the presence of parasitic parallel capacitance (C_p) limited the reproducibility of *I/V* characteristics. This made the exposition parameters difficult to replicate even in consecutive experiments [83].

Further work aimed at reducing the effects of C_p by limiting the current that flows through the sample. This was done by using a Metal-Oxide-Semiconductor Field-Effect Transistor-based regulation circuit (MOSFET), implementing proportional feedback loop (P-FL), which allowed the sample current to fluctuate under a given threshold. The results were consistent and reproducible since the current surges occurring above were limited by the regulation circuit. As a result, the size of the crystallized areas was scaled down to sub-100 nm dimensions indicating the benefits of current limitation to the process [84]. Note that even though the exposition current was limited, it was fluctuating under the given set-point value rather than stabilizing

3.2.1 FE-MISPC of a-Si:H with improved current control

In the article "Role of current profiles and Atomic Force Microscope tips on local electric crystallization of amorphous silicon" [95] we improved further the regulation circuit by adding a derivative feedback component (PD-FL). This allowed for electrical current stabilization to a given set-point rather than fluctuation under it [84]. However, results indicated that perfectly stabilized current results mostly in resistive pits and thus does not crystallize the a-Si:H. Detailed statistical analysis showed that some current fluctuation above or below the set-point is crucial for initiating crystallization.

In this work we also characterized the durability of different types of AFM tips by subjecting them to a series of FE-MISPC experiments. We found that the process has a destructive effect on silicon probes (including metal and diamond coated silicon). Nevertheless, this was not detrimental for successful nanocrystallization. Bulk ultra nanocrystalline diamond (UNCD) tips appeared less affected by FE-MISPC and showed superior durability.

Thin Solid Films 518 (2010) 5965–5970

Contents lists available at ScienceDirect

Thin Solid Films

journal homepage: www.elsevier.com/locate/tsf

Role of current profiles and atomic force microscope tips on local electric crystallization of amorphous silicon

E. Verveniotis *, B. Rezek, E. Šípek, J. Stuchlík, J. Kočka

Institute of Physics, ASCR, Cukrovarnická 10, 16253 Prague 6, Czech Republic

ARTICLE INFO

Article history:
Received 30 October 2009
Received in revised form 13 May 2010
Accepted 25 May 2010
Available online 31 May 2010

Keywords:
Amorphous materials
Atomic force Microscopy (AFM)
Conductivity
Crystallization
Nanostructures
Silicon
Nickel

ABSTRACT

Various types of conductive tips in atomic force microscope (AFM) are used to localize field-enhanced metal-induced solid phase crystallization (FE-MISPC) of amorphous silicon at room temperature down to nanoscale dimensions. The process is driven by electrical currents ranging from 0.1 nA to 3 nA between the tip and the bottom nickel electrode. The amplitude of the current is controlled by a metal-oxide-semiconductor field-effect transistor-based regulation circuit using proportional and derivative feedback loops. We analyze the results of the FE-MISPC process as a function of exposition current profiles, topographic changes, local conductivity changes (using current-sensing AFM) and regulation parameters. We found out that the FE-MISPC crystallization requires fluctuations of the exposition current rather than its stability. This is independent of the actual current set-point level. We also show the influence of the process on the AFM probes employed and vice versa. Bulk diamond probes exhibit superior endurance compared to bare or coated silicon probes, nevertheless all tips produce similar FE-MISPC results.

© 2010 Elsevier B.V. All rights reserved.

1. Introduction

Crystallization of amorphous silicon films is traditionally employed as an alternative method for producing large-area electronics such as displays and solar cells. It is typically induced by laser [1] or high-temperature furnace annealing [2]. The presence of silicide-forming metals such as nickel [3] or the application of an electric field [4,5] was found to reduce the crystallization temperature.

Nowadays, production of silicon nanocrystals has become increasingly important as they are attractive for nanoelectronic, optoelectronic, as well as biological applications [6,7]. Usually they are produced by electrochemical etching of bulk monocrystalline silicon, yielding the so-called porous silicon [8]. Yet, producing the nanocrystals in well-defined locations or creating arranged microscopic patterns still remains a challenging task.

Recently, we have shown that field-enhanced [4,5] metal-induced [3] solid phase crystallization (FE-MISPC) at room temperature can be used to achieve spatially localized current-induced crystallization of amorphous silicon films using a sharp tip such as those employed in atomic force microscopy (AFM) [9]. This process resulted in the formation of microscopic crystalline rings and dots at controlled positions in the amorphous silicon thin films. However, the smallest sizes of the crystallized objects ranged from a few hundred nanometers to several micrometers due to electrical discharge from the inherently present parallel capacitance, caused by a drastic increase of local material conductivity (and hence a decrease of potential difference on the parallel capacitance) after the dielectric breakdown of the films. The process was then further miniaturized below 100 nm by limiting the passing current (which was fluctuating below a given set-point) and thus also the electrical discharge between the conductive AFM tip and bottom nickel electrode [10]. It was assumed that further improvement of current stability during FE-MISPC would provide even smaller crystallites (below 10 nm).

In this work, the exposition current of the local FE-MISPC process is controlled and stabilized employing various regimes. The behavior of the electrical current and its effect on the formation of nanocrystals is analyzed and discussed. The effects of utilizing various types of AFM probes are characterized as well.

2. Method

The a-Si:H films are deposited by plasma-enhanced chemical vapor deposition in a thickness of 400 nm on a Corning 7059 glass substrate coated with 40 nm thin nickel film and 10 nm titanium interlayer for improved adhesion to glass. Substrate temperature of 50° C and 0.02% dilution of SiH_4 in helium result in a hydrogen content of 20–45 at.% in the films [11].

The FE-MISPC is accomplished by applying the electric field locally using a sharp conductive tip in atomic force microscope (AFM). Various types of tips are used: Pt/Cr-coated doped silicon, plain silicon, conductive diamond-coated silicon and bulk ultrananocrystalline

* Corresponding author. Tel.: +420 220 318 519; fax: +420 220 318 468.
E-mail address: verven@fzu.cz (E. Verveniotis).

0040-6090/$ – see front matter © 2010 Elsevier B.V. All rights reserved.
doi:10.1016/j.tsf.2010.05.107

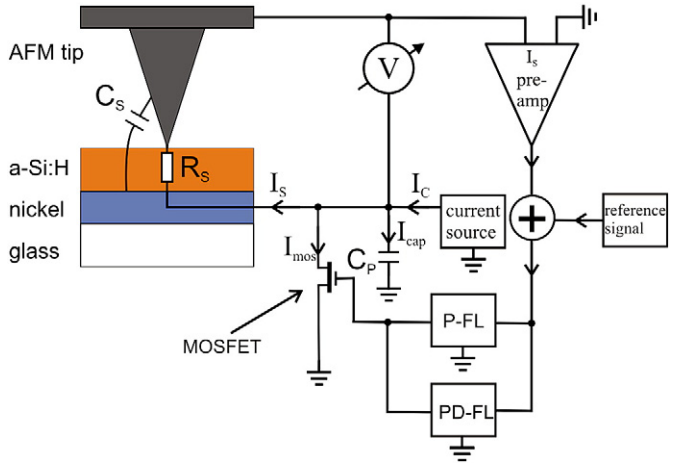

Fig. 1. Schematic drawing of the experimental setup and electrical circuit.

diamond (UNCD) tips. The typical tip radius is 10–70 nm depending on the type used. Spring constant of cantilevers, on which the tips are integrated, is between 0.2 Nm^{-1} and 22.5 Nm^{-1}. Using AFM the tips are put in contact with the a-Si:H film with the force of 10–500 nN.

Sample design and experimental set-up are shown schematically in Fig. 1. The FE-MISPC process is realized by applying a current I_s in the range of 100 pA to 3 nA, which is a part of the constant current I_c applied by an external source unit (100 nA–300 nA). The current source is connected to the bottom nickel electrode. The nickel electrode is negatively biased in order to facilitate the FE-MISPC process [4]. Oxidation of the silicon surface is thus of no concern as the AFM tip polarity cannot give rise to local anodic oxidation [12].

The current is stabilized to the I_s set-point using a metal-oxide-semiconductor field-effect transistor (MOSFET)-based regulator [10] at various regimes: current is allowed 1) to rise exponentially, where it typically reaches the target value after 1–5 s (proportional feedback loop, P-FL), 2) to rise rapidly up to the target value in the very beginning of the process (t<200 ms, proportional-derivative feedback loop, PD-FL) or 3) to rise by a ramp where it is increased steadily at a fixed rate, typically 0.01 nAs^{-1}–0.2 nAs^{-1}. The voltage V required to maintain the overall current I_c is monitored as a function of time t.

Note that the constant current I_c from the current source is not the desired value of the crystallization current (I_s set-point). The I_c current also charges the parallel capacitance C_p, which arises inherently from the wire leads and is typically 10–50 pF. Therefore, the sample current I_s is measured independently by an additional picoamperemeter (I_s preamplifier) in the tip-sample branch. The tip-sample capacitance C_s is in the order of aF and thus its influence is negligible compared to C_p.

Microscopic morphology and local conductivity of the films before and after the FE-MISPC process are characterized by current-sensing AFM, using contact forces of 10–500 nN (depending on the probe used) and sample bias voltage of −15 V to −60 V during scanning.

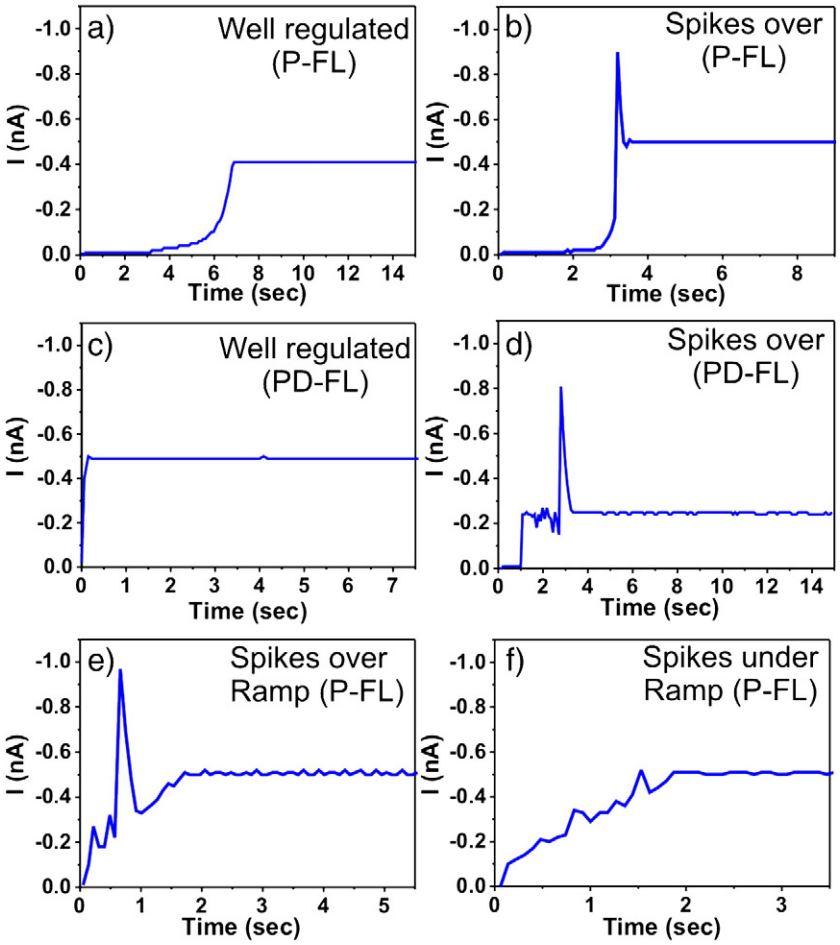

Fig. 2. Typical exposition current profiles corresponding to the following current control regimes: (a–b) Proportional feedback loop, (c–d) proportional-derivative feedback loop and (e–f) ramp. Curves (b) and (d) exhibit current spikes above the set-point current amplitude (I_s = 0.5 nA and 0.25 nA respectively). (e) Current rising by a ramp exhibiting a spike over the set-point. (f) Current profile with fluctuations below the current set-point.

Table 1
Statistics of current profiles obtained from 642 FE-MISPC experiments using different current control regimes. Percentages are calculated for each FL type (column).

Current behavior	P-FL	PD-FL	"Ramp"
Well regulated	116 (52%)	61 (26%)	65 (35%)
Spikes over	82 (37%)	85 (37%)	53 (29%)
Spikes under	26 (11%)	87 (37%)	67 (36 %)

Increased current detected in CS-AFM (current sensing-AFM) is a good indication of crystalline regions as corroborated previously by micro-Raman spectroscopy [10].

Scanning electron microscopy (SEM) and Energy Dispersive X-ray spectroscopy (EDX spectroscopy) were employed for the characterization of the AFM tips prior to and after the FE-MISPC process.

3. Results

Fig. 2 shows I_s profiles as a function of time during individual FE-MISPC experiments for the particular current control regimes. The profiles are typical and their character is independent of the actual I_s set-point value. Whereas Fig. 2(a) shows the well regulated P-FL regime where the current rises exponentially up to the set-point (−0.4 nA), in Fig. 2(b) one can see a "spike" well over the set-point (−1 nA vs. −0.5 nA), which appears shortly after the current starts rising, followed by stable current on the set-point value (−0.5 nA). Although the application of a faster PD feedback loop clearly made the current rise faster with quicker onset (Fig. 2(c)), the spikes still appeared (Fig. 2 (d)) with about the same probability (37%). The spikes were also observed when the current rise was slowed down by the ramp (Fig. 2(e)), albeit with somewhat smaller probability (29%). In addition to the current spikes over the set-point, we also encountered spikes and fluctuations below the set-point (spikes under, Fig. 2(f)).

In order to assess the progression of the crystallization process, statistically significant numbers of experiments were carried out. Table 1 summarizes the results of 642 FE-MISPC experiments using various current regulation regimes and current set-points. Note that even the application of the same experimental parameters can produce different types of current profiles. The current spikes over the set-point occur in about 1/3 of all experiments.

Fig. 3 then shows the typical current and voltage profiles during the spikes' occurrence. Note that while the sample current (I_s) is measured by a picoamperemeter (as shown in Fig. 1), the corresponding MOSFET and C_p currents (I_{mos} and I_{cap}) are calculated by the exposition software. The I_{mos} equals the source current minus the sum of the capacitance and the sample currents: $I_{mos} = I_c - (I_{cap} + I_s)$. The I_{cap} current equals the magnitude of the capacitance times the time derivative of the source voltage: $I_{cap} = C\, dV/dt$.

We can see that the bulk of the excess current (−220 nA), which is generated by the discharge of C_p, is shunt via the MOSFET (Fig. 3 (a)). Only a small part of this current makes it to the sample (−0,4 nA vs. −220 nA, 0,2%). Note that the current stabilizes after the spikes, but the voltage across the sample drops nearly to zero. Such a drop in the sample voltage as a consequence of the I_s spike can be seen in Fig. 3 (c). It indicates an increase of the local material conductivity (from 8 pS to 100 pS) and, at the same time, it effectively minimizes further energy transfer into the sample.

Fig. 4 gives several examples of how the current profiles modify the a-Si:H thin films, in this particular case using bulk diamond (UNCD) tips. The current spikes over the set-point were mainly (70% of the cases) causing "explosive" effect on the sample as shown in Fig. 4 (a). During the process, material is exerted from the sample and accumulates around the central pit (here 120 nm deep, 500 nm wide). Corresponding local current map in Fig. 4(c) reveals that a highly conductive area forms in that place.

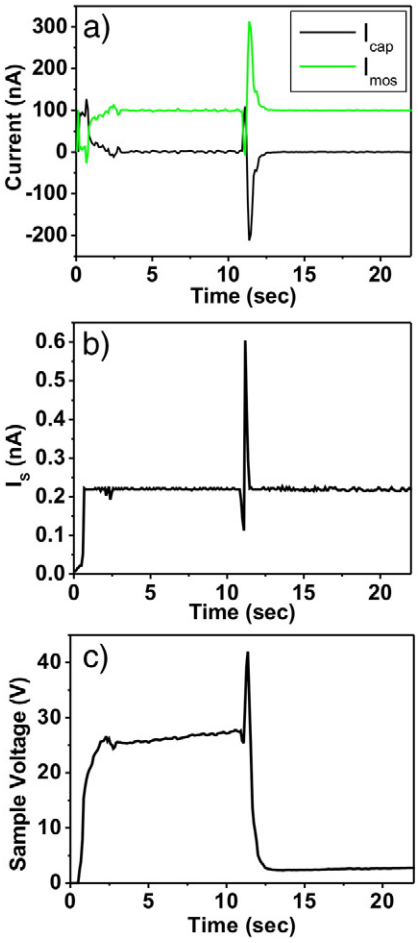

Fig. 3. (a) Calculated parallel capacitance and MOSFET currents (I_{cap} and I_{mos} respectively), (b) measured sample current, and (c) sample voltage during a FE-MISPC experiment ($I_c = 100$ nA).

When the current was stable (such as in Fig. 2(a) and 2(c)) we observed mainly (in 75%) the formation of well-defined pits (here 50 nm deep, 300 nm wide) not accompanied by an increase in the conductivity (Fig. 4(e) and 4(g)). Small fluctuations under the set-point resulted mostly in either non-conductive pits (49%) or had no effect on the thin film (34%).

Table 2 summarizes the above-described correlation of morphological effects and exposure current profiles. The numbers in brackets are related to instances where crystallization occurred as indicated by CS-AFM. The crystallization was achieved even when the current set-point was relatively low (100 pA) as long as the current was exhibiting spikes. On the other hand, stable currents of up to 3 nA did not produce crystallization most of the times. In addition, there was no correlation between the current set-point value and the size of the crystallized areas.

Table 3 analyzes correlation of the spike occurrence with the current set-point. We can see that spikes occur in about 2/3 of the total experiments for each set-point value. Also, the cases of well regulated current are statistically comparable for each set-point value. From the above we can say that the spike occurrence is independent of the actual current set-point.

A possible influence of the tip material and properties on the nanocrystallization process was investigated using four different kinds of AFM probes. No correlation was found. The character of current profiles and the process outcomes were similar regardless of the probe used. Nevertheless, the AFM probes themselves were affected. As we can see in SEM images before and after the FE-MISPC experiments (Fig. 5), after 18 expositions, the apex of the tips is

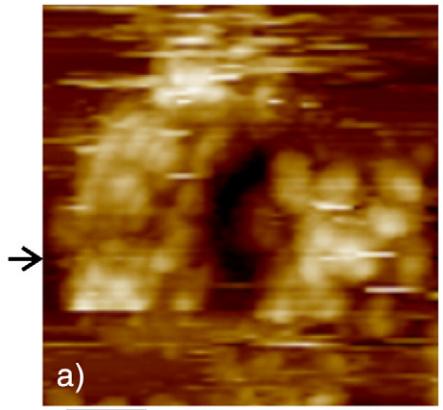
a)
400 nm
Z scale: 200nm

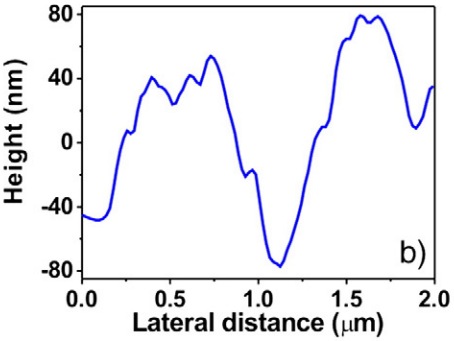
Height (nm)
80
40
0
-40
-80
0.0
0.5
1.0
1.5
2.0
Lateral distance (μm)
b)

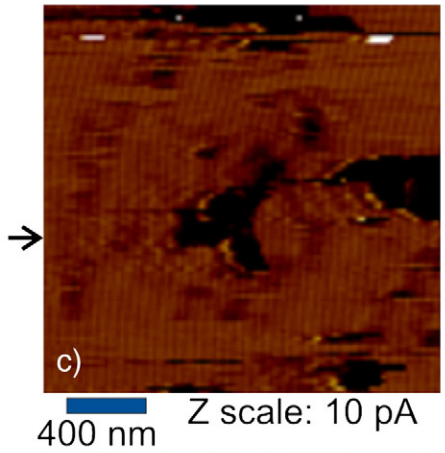
c)
400 nm
Z scale: 10 pA

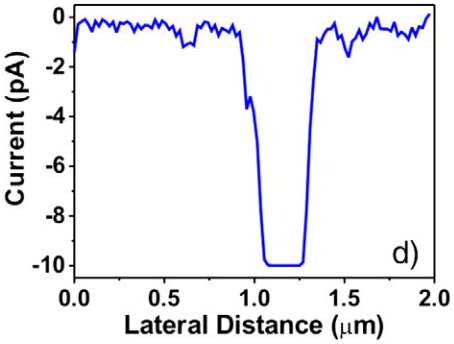
Current (pA)
0
-2
-4
-6
-8
-10
0.0
0.5
1.0
1.5
2.0
Lateral Distance (μm)
d)

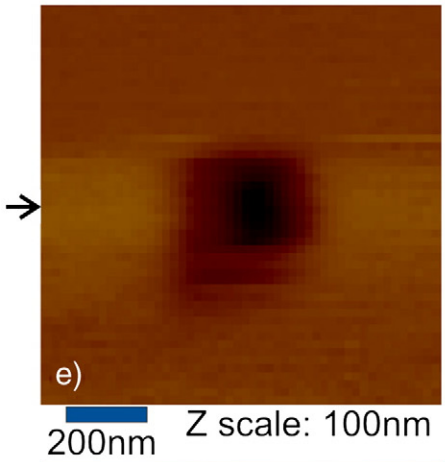
e)
200nm
Z scale: 100nm

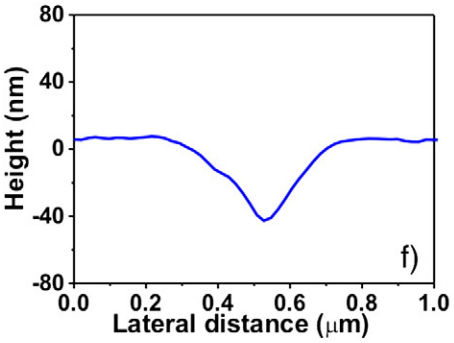
Height (nm)
80
40
0
-40
-80
0.0
0.2
0.4
0.6
0.8
1.0
Lateral distance (μm)
f)

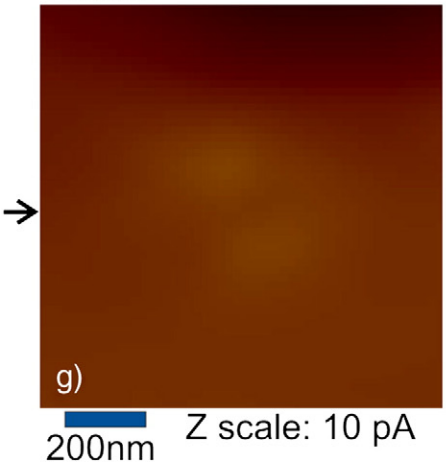
g)
200nm
Z scale: 10 pA

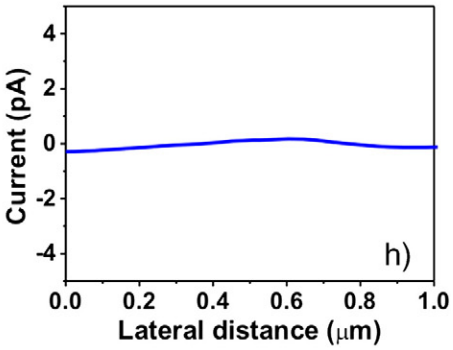
Current (pA)
4
2
0
-2
-4
0.0
0.2
0.4
0.6
0.8
1.0
Lateral distance (μm)
h)

Table 2
Topography after the experiment for the various current behavior cases. In parenthesis we show how many times out of the given number the enhancement of signal on the CS-AFM (crystallization) occurred. Percentages are calculated for each current profile type (column).

Topography	Well regulated	"Spikes" over	"Spikes" under
Clean	46 (0) 19%	20 (0) 9%	61 (0) 34%
Explosion	15 (11) 6% (5%)	171 (154) 78% (70%)	31 (26) 17 % (15%)
Pit	181 (0) 75%	29 (0) 13%	88 (0) 49%

Table 3
Spike occurrence with respect to the current set-point. In parenthesis we show how many times out of the total experiments for each set-point the enhancement of signal on the CS-AFM (crystallization) occurred. Percentages are calculated for each current set-point (row).

Setpoint (nA)	Well regulated	Spike occurrence
0.25	32 (0) 36%	58 (29) 64% (32%)
0.5	97 (8) 38% (3%)	157 (93) 62% (37%)
1	54 (3) 34% (2%)	107 (37) 66% (23%)
>1	59 (0) 43%	78 (21) 57% (15%)

modified: on the coated and bare silicon tips (Fig. 5 (a, b), (c, d) and (e, f) respectively) the modification of the apex is pronounced. EDX spectroscopy showed that for the coated tips the conductive coating (Pt/Cr, diamond) is mostly removed at the apex. UNCD tips (Fig. 5 (g) and 5 (h)) show better stability than the others most likely due to the durability of the material. EDX on the UNCD tip detected Si at the tip's apex, most likely transferred from the silicon thin film during the process. In all cases the probes used show wear which cannot be due to typical AFM scans. Thus, this effect is attributed to the FE-MISPC process itself.

4. Discussion

In this work, the current control was significantly improved compared to previous reports [9,10]. The current regulation was working well and the discharges from C_p (when they occur) were compensated from 99.8%. Nevertheless, the remaining 0.2% of the current discharge made it to the sample and appeared as spikes on the exposure current profiles. In the FL we use, the P component regulates proportionally to the error (distance from the set-point at a given time) and the D component does so by following the change rate in the output (generated by the P component). Obviously, such inherently imprecise P or PD feedback loops cannot fully compensate for the current spikes. Precise compensation would require the integration type of feedback but that is too slow for our purpose.

Analysis of the exposure current profiles and process outcomes shows that the current spikes are in fact necessary for achieving crystallization. Perfectly stabilized current profiles mostly resulted in non-conductive pits. Taking into consideration previous works, where FE-MISPC was employed, the current must be allowed to fluctuate either over [9] or under [10] the given threshold in order to achieve the crystallization. The process is more or less independent of the current set-point (in the range 100 pA–3 nA), although, the set-point values >1 nA appear somewhat less efficient for crystallization. This also evidences the independence of the spike occurrence on the actual current set-point under the employed current regulation regimes, as seen in Table 3.

Hence, we actually cannot control whether the current spike occurs or not. Varying current profiles for the same experimental parameters as well as random (1/3 of all cases) occurrence of spikes over the set-point may be attributed to various reasons: 1) local material properties of the sample which can affect the dielectric breakdown and therefore the crystallization process, 2) local properties of the tip-sample contact (including the tip's apex quality), which can affect the current flow as well as the dielectric breakdown, and 3) the randomness of the dielectric breakdown itself [13,14].

Concerning the local material properties, mapping of the electronic properties of pristine a-Si:H films by CS-AFM showed homogeneous background on the scale of μm (as shown for instance in Fig. 4(g)). As for local tip-sample properties, we obtained very similar results irrespectively of the AFM probe and contact force (10–500 nN) used. This shows that the destructive effect of FE-MISPC on the AFM tips may influence the consecutive AFM image quality but not the crystallization process itself. As mentioned above, the UNCD probes exhibited superior endurance in the FE-MISPC process compared to the coated/silicon tips. Even in that case, though, the crystallization process behaved in the same way in terms of current profiles and results. Hence, the responsible factor is most likely the randomness of the dielectric breakdown which cannot be controlled [14].

The key for improving this technique most likely lies in limiting the amplitude of the exposition current fluctuations (such as e.g. in [10]) rather than perfect current stabilization. Note that the current fluctuations observed in this work (Fig. 2(f)) are rather due to a "noise" of the tip-sample contact than to the crystallization such as in [10]. They can be attributed to the apex forming during the first few expositions when using a new coated or bare silicon tip. Similar forming of the AFM tips was reported also during CS-AFM on silicon thin films in ultra-high vacuum [15]. It was attributed to the removal of oxide from the silicon-based tips. Such forming mechanism is corroborated by the fact that the "noise" was not observed here when experimenting with the UNCD tips.

5. Conclusions

Application of diverse electric current profiles via a sharp conductive AFM tip through the a-Si:H films to the bottom nickel electrode was used to produce local microscopic FE-MISPC crystallization of amorphous films. CS-AFM at high spatial resolution identified the crystalline regions due to their higher conductivity. By performing large number of experiments (642) we found out that the local crystallization is in most cases (70%) initiated by exposition current spikes over the set-point current level, which cannot be controlled by inherently imprecise P or PD feedback loop. Various current control regimes, current set-points as well as different AFM probes and contact forces did not alter the results significantly. Such behavior was observed in spite of the fact that AFM tips underwent pronounced changes of their shape and coating (with bulk diamond (UNCD) being the most stable). Allowing for the current fluctuations is thus most likely the key for optimizing local nanocrystallization of silicon based on FE-MISPC process.

Acknowledgements

Financial support from the Fellowship J E Purkyně (ASCR) and research projects KAN400100701 (ASCR), LC06040 (MŠMT), LC510 (MŠMT), AV0Z10100521, SVV-2010-261307 and 202/09/H041 is gratefully acknowledged. We appreciate donation of bulk UNCD tips from Advanced Diamond Technologies Inc. (USA). We gratefully

Fig. 4. FE-MISPC with a bulk UNCD diamond tip. (a) Local topography and (c) CS-AFM images of the Si film after a typical "spike over" experiment (set-point = 0.5 nA) and their corresponding cross sections ((b) and (d), respectively). (e) Formation of a pit in the topography by well regulated current (set-point = 3 nA), (g) the corresponding CS-AFM image and their respective cross sections ((f) and (h), respectively). Cross sections are indicated by arrows.

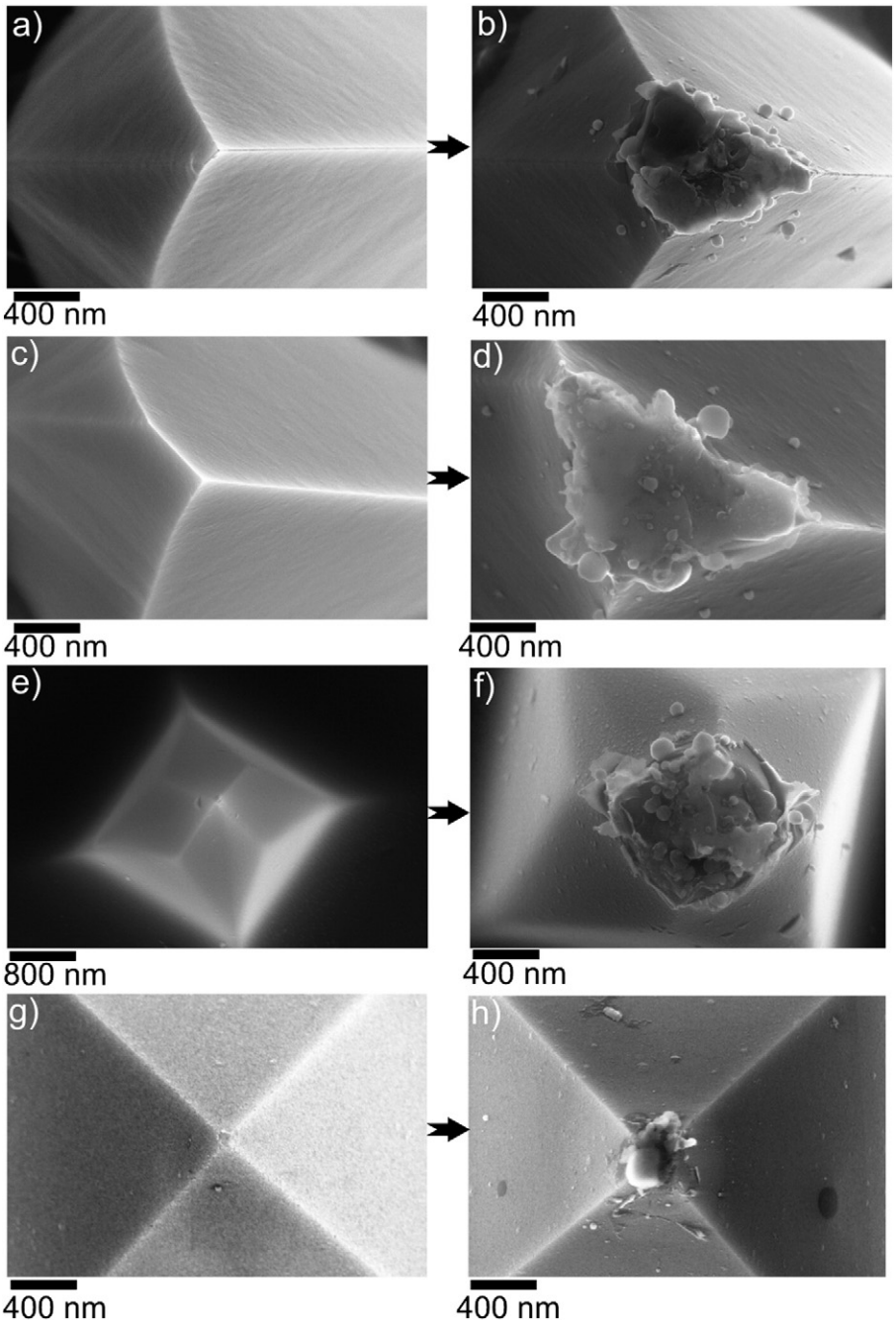

Fig. 5. AFM tips before (left) and after (right) 18 FE-MISPC experiments. Current set-point was 6 times equal to 0.5 nA, 6 times equal to 1 nA and 6 times equal to 1.5 nA for each tip shown. From top to bottom we see Pt/Cr coated, Silicon, Diamond-coated and bulk diamond (UNCD) tip, respectively. Events of crystallization for each tip were 12, 8, 10 and 10 respectively.

acknowledge K. Jurek for EDX spectroscopy, K. Hruska for SEM imaging and K. Kusová for English corrections.

References

[1] B. Rezek, C.E. Nebel, M. Stutzmann, Jpn. J. Appl. Phys. 38 (1999) L1083.
[2] K. Nakazawa, J. Appl. Phys. 69 (1991) 1703.
[3] L.K. Lam, S. Chen, D.G. Ast, Appl. Phys. Lett. 74 (1999) 1866.
[4] P. Fojtik, K. Dohnalová, T. Mates, J. Stuchlík, I. Gregora, J. Chval, A. Fejfar, J. Kočka, I. Pelant, Phil. Mag. B 82 (2002) 1785.
[5] S.Y. Yoon, S.J. Park, K.H. Kim, J. Jang, Thin Solid Films 383 (2001) 34.
[6] F. Trojánek, K. Neudert, M. Bittner, P. Malý, Phys. Rev. B 72 (2005) 075365.
[7] A. Fučíková, J. Valenta, I. Pelant, V. Březina, Acta Metall. Slovaca 13 (2007) 88.
[8] O. Bisi, S. Ossicini, L. Pavesi, Surf. Sci. Rep. 38 (2000) 1.
[9] B. Rezek, E. Šípek, M. Ledinský, P. Krejza, J. Stuchlík, J. Kočka, J. Non-Cryst. Solids 354 (2008) 2305.
[10] B. Rezek, E. Šípek, M. Ledinský, J. Stuchlík, A. Vetushka, J. Kočka, Nanotechnology 20 (2009) 045302.
[11] K. Luterová, I. Pelant, P. Fojtík, M. Nikl, I. Gregora, J. Kočka, J. Dian, J. Valenta, P. Malý, J. Kudrna, J. Štěpánek, A. Poruba, P. Horváth, Phil. Mag. B 80 (2000) 1811.
[12] B. Rezek, T. Mates, J. Stuchlík, J. Kočka, A. Stemmer, Appl. Phys. Lett. 83 (2003) 1764.
[13] X. Li, C.H. Tung, K.L. Pey, Appl. Phys. Lett. 93 (2008) 072903.
[14] F. Family, Y.C. Zhang, T. Vicsek, J. Phys. A: Math. Gen. 19 (1986) L733.
[15] B. Rezek, J. Stuchlík, A. Fejfar, J. Kočka, J. Appl. Phys. 92 (2002) 587.

3.2.2 Effect of secondary silicon deposition on FE-MISPC pits

In the article "Impact of AFM-induced nano-pits in a-Si:H films on silicon crystal growth" [96] we used FE-MISPC-induced features (both conductive and resistive) as interface for a secondary mixed-phase silicon deposition. The results showed that silicon nanocrystals are deposited preferentially in the pits and partially also in the pit vicinity. This is evidenced by the pronounced rise of conductivity exhibited in the previously resistive pits. We proved that this was not caused by the elevated temperature during the second deposition as the increase in conductivity is solely due to the newly grown nanocrystals. By this method we were able to further reduce the size of the crystalline regions to < 50 nm for the case of the originally resistive nano-pits. In addition, the features that were already crystalline after FE-MISPC show a 6x increase in their electrical conductivity, which evidences an increase in their crystallinity.

In the article "Generating ordered Si nanocrystals via atomic force microscopy" [99] we reviewed the progress done through the whole course of this continuous study [83, 84, 96], pointing out the most important findings and discussing the results as a whole.

Nanoscale Research Letters
a SpringerOpen Journal

NANO EXPRESS Open Access

Impact of AFM-induced nano-pits in a-Si:H films on silicon crystal growth

Elisseos Verveniotis*, Bohuslav Rezek, Emil Šípek, Jiří Stuchlík, Martin Ledinský, Jan Kočka

Abstract

Conductive tips in atomic force microscopy (AFM) can be used to localize field-enhanced metal-induced solid-phase crystallization (FE-MISPC) of amorphous silicon (a-Si:H) at room temperature down to nanoscale dimensions. In this article, the authors show that such local modifications can be used to selectively induce further localized growth of silicon nanocrystals. First, a-Si:H films by plasma-enhanced chemical vapor deposition on nickel/glass substrates are prepared. After the FE-MISPC process, yielding both conductive and non-conductive nano-pits in the films, the second silicon layer at the boundary condition of amorphous and microcrystalline growth is deposited. Comparing AFM morphology and current-sensing AFM data on the first and second layers, it is observed that the second deposition changes the morphology and increases the local conductivity of FE-MISPC-induced pits by up to an order of magnitude irrespective of their prior conductivity. This is attributed to the silicon nanocrystals (<100 nm) that tend to nucleate and grow inside the pits. This is also supported by micro-Raman spectroscopy.

Introduction

Crystallization of amorphous silicon (a-Si:H) films is traditionally employed as an alternative method for producing large-area electronics such as displays and solar cells. It is typically induced by laser [1] or high-temperature furnace annealing [2]. The presence of silicide-forming metals such as nickel [3] or the application of an electric field [4,5] was found to reduce the crystallization temperature.

Nowadays, the production of silicon nanocrystals has become increasingly important as they are attractive for nanoelectronic, optoelectronic, as well as biological applications [6]. Usually, they are produced in the form of the so-called micro-crystalline silicon thin films using chemical vapor deposition (CVD) [7,8] or by electrochemical etching of bulk monocrystalline silicon, yielding the so-called porous silicon [9]. Yet, producing the nanocrystals in well-defined locations or creating arranged microscopic patterns still remains a challenging task.

Recently, our previous studies have shown that field-enhanced [4,5] metal-induced [3] solid-phase crystallization (FE-MISPC) at room temperature can be used to achieve spatially localized current-induced crystallization of a-Si:H films using a sharp tip such as those employed in atomic force microscopy (AFM) [10]. This process resulted in the formation of microscopic crystalline rings and dots as well as resistive nano-pits at controlled positions in the a-Si:H thin films. The smallest sizes of the crystallized objects ranged from a few hundred nanometers to several micrometers due to electrical discharge from the inherently present parallel capacitance, caused by a drastic increase of local material conductivity (and hence a decrease of potential difference on the parallel capacitance) after the dielectric breakdown of the films. The process was then further miniaturized below 100 nm by limiting the passing current (which was fluctuating below a given set-point) and thus also the electrical discharge between the conductive AFM tip and bottom nickel electrode [11]. On the other hand, perfectly stabilized electrical current during FE-MISPC process produced mainly non-conductive pits [12].

In this study, how the FE-MISPC-induced features (conductive and non-conductive pits) affect further nucleation and growth of the secondary silicon thin film is investigated. For this purpose, the second silicon layer at the boundary condition of amorphous/micro-crystalline growth after local FE-MISPC modifications of the first fully amorphous layer is deposited. The effects of the second deposition on the crystallinity, conductivity, structure, and spatial localization of the features based

* Correspondence: verven@fzu.cz
Institute of Physics ASCR, Cukrovarnicka 10, 16253, Prague 6, Czech Republic

SpringerOpen

© 2011 Verveniotis et al; licensee Springer. This is an Open Access article distributed under the terms of the Creative Commons Attribution License (http://creativecommons.org/licenses/by/2.0), which permits unrestricted use, distribution, and reproduction in any medium, provided the original work is properly cited.

on their initial morphology and conductivity are discussed.

Method

The a-Si:H films are deposited by plasma-enhanced CVD in a thickness of 170 nm (±30 nm, measured by a stylus profilometer) on a Corning 7059 glass substrate coated with 40-nm-thin nickel film and 10 nm titanium interlayer for improved adhesion to glass. Substrate temperature of 50°C and 0.02% dilution of SiH_4 in helium result in a hydrogen content of 20-45 at.% in the films [13].

The FE-MISPC is accomplished by applying the electric field locally using a sharp conductive tip in AFM. Employed tips were either Pt/Cr-coated doped silicon (ContE, Budgetsensors) or conductive diamond-coated silicon (DCP11, NT-MDT). The typical tip radius is 10-70 nm depending on the type used. The tips are put in contact with the a-Si:H film with the force of 10-500 nN. The current source is connected to the bottom nickel electrode. The nickel electrode is negatively biased to facilitate the FE-MISPC process [4]. Oxidation of the silicon surface is thus of no concern as the AFM tip polarity cannot give rise to local anodic oxidation [14]. Details of the setup can be found in Refs. [11,12]. The FE-MISPC process is realized by a sample current of -0.5 nA, which is part of the constant current (-100 nA) applied by an external source unit (Keithley K237). Outcome of the exposition is determined by its temporal profile [12].

Microscopic morphology and local conductivity of the films before and after the FE-MISPC process are characterized by current-sensing AFM (CS-AFM) [15] using sample bias voltage of -25 V. Increased local current detected by CS-AFM is a good indication of crystallinity as corroborated previously by micro-Raman spectroscopy [11]. Such high sensing bias is used because of the amorphous nature (and hence the low conductivity) of the pristine film and additional tunneling barrier of the native oxide on the film interface [16].

After the FE-MISPC process, the second silicon layer is deposited on top of the initial film at 100°C in the thickness of about 200 nm (±30 nm). This deposition is done at the boundary conditions of amorphous and micro-crystalline silicon growth [17,18]. CS-AFM experiments are then again conducted on the previously processed areas for determining the impact of the second deposition on the FE-MISPC-induced features. Micro-Raman spectroscopy (diode laser, λ = 785 nm, P = 1 mW, objective 100×) is employed to characterize the crystallinity [19] of the FE-MISPC exposed spots after the second deposition.

In order to find the exposed areas after the second layer deposition, the samples were marked with a laser (HeCd laser, λ = 442 nm, P = 30 mW) prior to FE-MISPC process.

Results

Figure 1a shows the typical local topography after an FE-MISPC experiment exhibiting current spikes over the set-point [12]. The diameter of the pit is 300 nm, and it can be seen that some material is accumulated around the hole. The cross section plotted in Figure 1b shows that the depth of the pit is 100 nm. The full-width-at-half-maximum (FWHM) is 200 nm. In Figure 1e is shown the local conductivity map of the same area obtained at the sample bias voltage of -25 V. The conductive region is mainly focused in the pit. The cross section plotted in Figure 1f shows the spatial profile of electrical current inside the pit. Peak current is 100 pA, and FWHM is 60 nm.

Figure 1c,g, shows the local topography and conductivity map obtained at the sample bias voltage of -25 V in exactly the same area as in Figure 1a,e after the second layer was deposited. AFM topography shows an accumulation of typical silicon micro- and nano-crystals [15] around the pit. CS-AFM shows conductive regions localized within the pit. Note that the individual silicon crystals present due to the second deposition do not appear conductive because the current pre-amplifier setting (sensitivity = 1 nA/V) was adjusted to the magnitude of the current in the pit. Scanning the same area with higher current sensitivity (1 pA/V) showed conductivity on every single crystal seen in the topography. Cross sections plotted in Figure 2d,h, respectively, show that the pit depth is now 175 nm (FWHM is 200 nm) and that the conductive region exhibits an electrical current peak of 670 pA (FWHM is 30 nm).

Figure 2a illustrates the local topography of an area after three separate FE-MISPC experiments exhibiting stable current. The pits this time are non-conductive as seen in the corresponding CS-AFM image and its cross section (see Figure 2e,g). Their diameter is about 300 nm for all the pits. Their depth is 40-50 nm as shown by the spatial profile in Figure 2c. FWHM is about 200 nm (middle pit).

Topography of the same spot after second deposition (see Figure 2b) shows several small silicon nano-crystals scattered across the area. The depth of the pits increased to 50-60 nm as shown by the spatial profile in Figure 2d. FWHM is 180 nm (middle pit). In the CS-AFM image after the second deposition (see Figure 2f), it can be seen that the previously non-conductive pits now exhibit pronounced difference in conductance. Corresponding current spatial profile in Figure 3h shows a peak current up to 65 pA at -25 V. FWHM is 40 nm (middle pit).

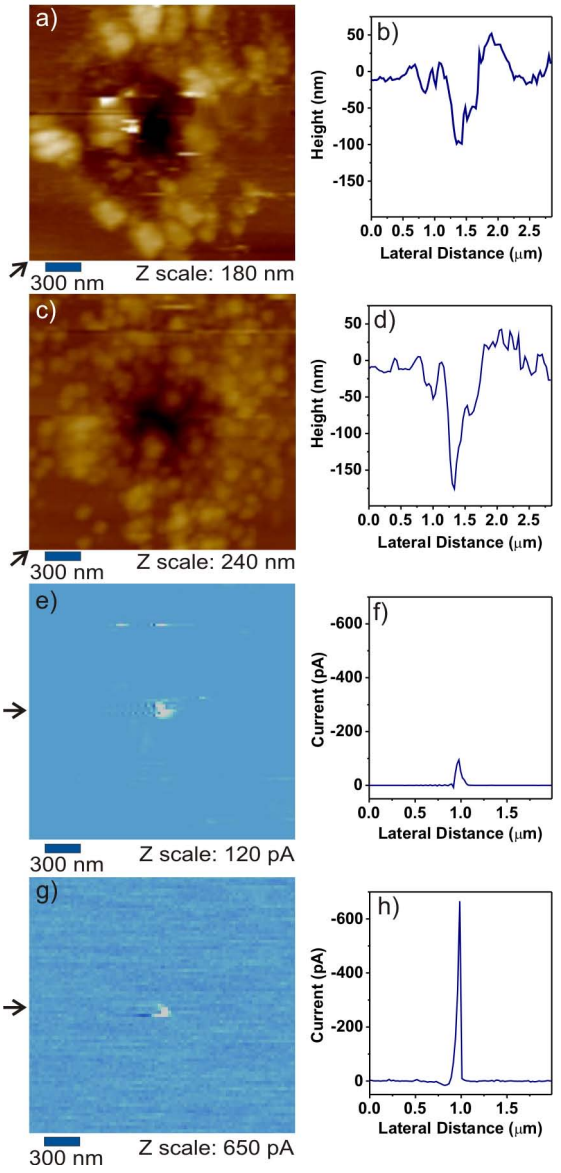

Figure 1 Local topography images after. **(a)** the FE-MISPC process and **(c)** the second deposition of the same spot. Their cross sections are plotted in **(b, d)**, respectively. **(e, g)** CS-AFM images corresponding to **(a)** and **(c)**, respectively. Their cross sections are plotted in **(f, h)**, respectively. Positions of the cross sections are indicated by arrows next to the images.

Figure 3 shows the middle pit of Figure 2 in three-dimensional representation before (a) and after (b) the second deposition. Besides the growth-induced depth change, modifications in the local morphology inside the pit can also be seen. The bottom of the pit turns from smooth to rough. Note that the images of Figure 3a,b are optimized to emphasize on the features of the pit in the *z*-direction, and consequently their real aspect ratio is not maintained.

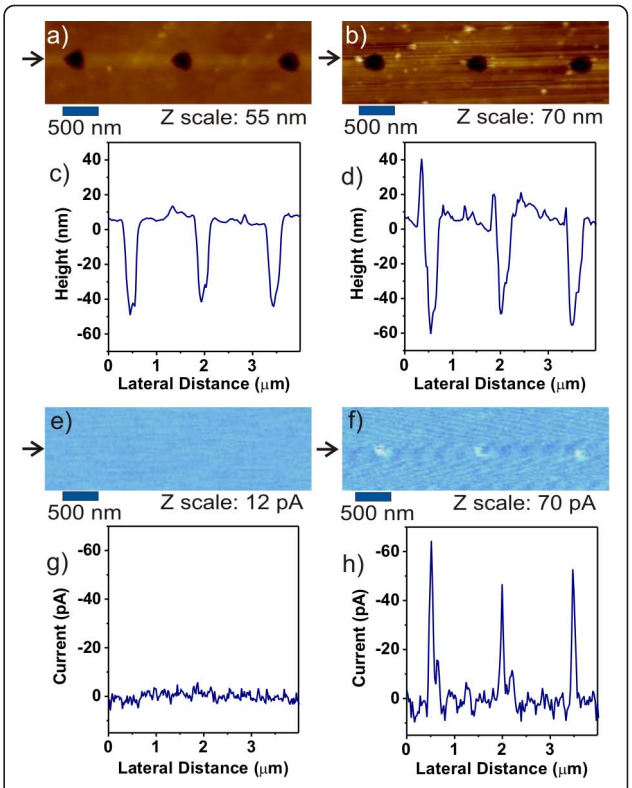

Figure 2 Local morphology images after FE-MISPC resulting in non-conductive pits. **(a)** AFM topography; **(e)** CS-AFM of the same spot, and their corresponding cross sections **(c, g)**; **(b)** AFM topography of the same area after the second deposition; **(f)** CS-AFM and the respective cross sections **(d, h)**. The cross sections are indicated by arrows next to the AFM images.

Figure 4 shows the micro-Raman spectrum measured on the conductive pit after second deposition (AFM topography is shown in the inset image). The crystalline silicon peak at 521 cm^{-1} is well resolvable, even though it is superimposed with much more pronounced amorphous band. This is because most of the material in the focus of the Raman is amorphous. Accounting for Raman focus diameter of about 700 nm (objective 100×, λ = 785 nm) and crystalline region diameter of 100 nm, crystalline fraction makes only 2% of the detection area.

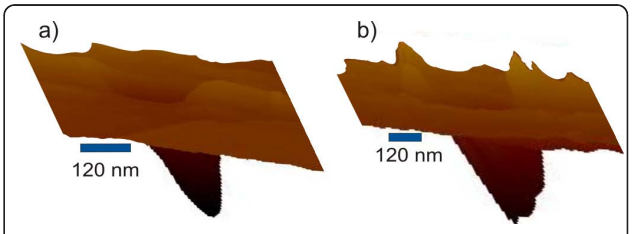

Figure 3 Three-dimensional AFM topography of the middle pit in Figure 2: **(a)** after FE-MISPC process, **(b)** after the second silicon deposition.

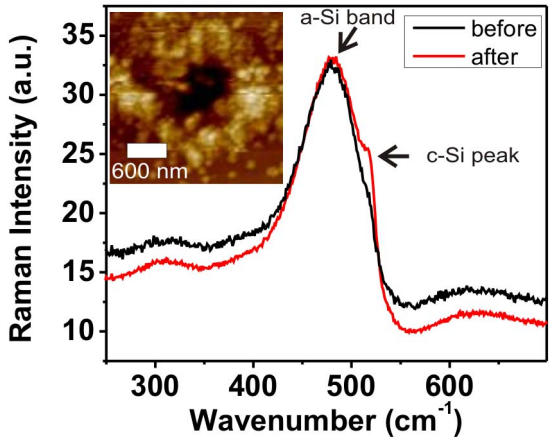

Figure 4 Raman spectra of FE-MISPC induced conductive features before and after the second deposition process. The inset shows the topography of the measured area corresponding to the spectrum "after". The spectrum was measured in the central part of the pit. Spectra are normalized to the amorphous band.

Raman measurements, before the second deposition on various FE-MISPC-exposed spots, showed only broad amorphous band (typical spectrum shown in Figure 4), obviously because the crystalline phase amount was below the detection threshold.

Discussion

The critical factor controlling the outcome of FE-MISPC is the AFM tip. When it is new, in the first few expositions, it produces larger, conductive pits irrespective of the exposition current. During those expositions, the tip is being "formed." After tip "forming," the use of exposition currents in the range of 0.05-0.15 nA results always in non-conductive pits as also reported previously [10]. Producing small conductive pits relies on current limitation [11] while allowing for current fluctuations [11,12]. The typical yield is 70% so far [12].

By correlating increased local conductivity [15] and crystalline silicon peak or at least a shoulder (because of <2% fraction of the detection area) in micro-Raman spectra, it can be concluded that silicon nanocrystals are formed inside the pits after the second deposition. This conclusion is also supported by the change of local morphology. As illustrated in Figure 3, the bottom of the pit changes from smooth to rough. Furthermore, the increase in the pit depth after the second deposition is smaller than the thickness of the deposited layer (changed by 75 nm in the case of conductive pits or by 10 nm the case of non-conductive pits vs. 200 nm of the second film thickness). This indicates that there must be some growth occurring inside the pits as well. This effect can be in particular pronounced because the second silicon deposition is performed at the boundary of amorphous and microcrystalline growth where silicon crystals typically protrude above the amorphous film because of their faster growth [15].

Under the boundary deposition conditions, silicon nanocrystals and their aggregates (the so-called microcrystalline columns) nucleate at random positions in otherwise uniform a-Si:H [15,17]. Upon using the localized FE-MISPC process, the nucleation became focused into the processed regions. In the case of initially conductive pits, the nanocrystal density is increased also around the pit compared to farther surroundings. This may be due to topographical as well as structural modification of the first a-Si:H film, because, e.g., some additional local stress and/or atomic scale defects may be induced around the processed area [20].

In the case of non-conductive pits, the overall density of nanocrystals remained uniform, i.e., nanocrystals are randomly scattered across the surface, except for the perfectly focused growth inside the pits. Formation of non-conductive pits introduces most likely less stress and defects in the local structure of the film, thus not enhancing crystal nucleation around the pit. The non-conductive pits exhibit pronounced increase in conductivity after the second deposition compared to the initial resistive state (see Figure 3). As the background exhibits conductivity of <5 pA (due to current pre-amplifier noise at the selected current range), the increase from the second deposition is of one order of magnitude or more. This indicates that new silicon nanocrystals are formed and localized in the pits. The non-conductive pits are thus the most promising candidates for selective growth of Si micro- and nano-crystals.

Note that the nanocrystals, which are scattered randomly across the surface or just around the pit, are also conductive compared to the a-Si:H background, in agreement with previous reports [15]. However, their conductivity is two orders of magnitude lower compared to the center of the pit. Hence, they do not appear as brighter dots in the current images. This is most likely because they are grown on the a-Si:H film (with possibly additional amorphous incubation layer [17]). It can be assumed that the much higher conductivity of the nanocrystals inside the pits is because they nucleate more readily without amorphous stage and are also better connected to the bottom electrode, e.g., via the conductive path made by the FE-MISPC process that may be further improved by the elevated temperature during the second deposition.

There are several possible factors that can promote nucleation and growth of silicon nanocrystals inside both types of the pits created by local FE-MISPC process. First, growth precursors during the second CVD deposition may become more localized inside the pits. Second, density of a-Si:H defects can be increased inside

the pits due to local heating and/or evolution of hydrogen as in the case of laser annealing that also can promote further growth of crystalline silicon [20]. Third, local stress or strain may be increased inside the pits and may increase the nucleation probability. Fourth, crystal growth may proceed on the already existing crystals in the case of conductive pits. Fifth, the elevated temperature during second deposition (100°C) may also affect the crystallinity of the features. To resolve this, thermal annealing of a FE-MISPC-exposed sample was performed. The annealing conditions were identical to the second deposition conditions described above, but without the plasma. We noticed some increase in the local currents after the annealing only on the previously conductive pits. Since this temperature is not enough to promote Si deposition, this effect is merely thermal. In the case of non-conductive pits, there was no effect on the structural or electronic properties detected. The last two factors thus cannot explain the growth in non-conductive pits. The other factors may all contribute to certain extent, and the main contribution cannot be presently resolved.

Conclusions

This study demonstrated that the deposition of a second silicon layer at the boundary condition of amorphous/micro-crystalline growth on top of the a-Si:H film could increase the conductivity of areas previously processed by the local FE-MISPC using AFM. The following effects were observed: (i) conductivity of conductive features (pits) was increased by up to six times, and (ii) new sub-100 nm conductive spots were generated in non-conductive pits. The increase in the local conductivity was attributed to the formation of silicon nanocrystals (<100 nm) inside the pits as evidenced by CS-AFM profiles. It was also corroborated by changes of morphology and by micro-Raman spectra. The process is the most defined in the case of non-conductive pits. This study thus opens perspectives for the growth of Si nanocrystals in predefined positions with nanoscale precision using the secondary deposition process. Such procedure, for instance, could be used to adjust the preferred properties of the nanocrystals by the deposition parameters.

Abbreviations

AFM: atomic force microscopy; CS-AFM: current-sensing AFM; CVD: chemical vapor deposition; FE-MISPC: field-enhanced metal-induced solid phase crystallization; FWHM: full-width-at-half-maximum.

Acknowledgements

Financial support from research projects KAN400100701 (ASCR), LC06040 (MŠMT), LC510 (MŠMT), SVV-2010-261307, 202/09/H041, AV0Z10100521, and the Fellowship J E Purkyně (ASCR) is gratefully acknowledged.

Authors' contributions

EV carried out the AFM/CS-AFM measurements and drafted the manuscript. BR participated in the design and coordination of the study, and edited the manuscript. EŠ designed and materialized the exposition circuit and the control software. JS performed the CVD deposition of the silicon thin films. ML performed the Raman meaurements. JK concieved the study and participated in its coordination.

Competing interests

The authors declare that they have no competing interests.

Received: 24 September 2010 Accepted: 15 February 2011
Published: 15 February 2011

References

1. Rezek B, Nebel CE, Stutzmann M: **"Polycrystalline Silicon Thin Films Produced by Interference Laser Crystallization of Amorphous Silicon".** *Jpn J Appl Phys* 1999, **38**:L1083.
2. Nakazawa K: **"Recrystallization of amorphous silicon films deposited by low-pressure chemical vapor deposition from Si_2H_6 gas".** *J Appl Phys* 1991, **69**:1703.
3. Lam LK, Chen S, Ast DG: **"Kinetics of nickel-induced lateral crystallization of amorphous silicon thin-film transistors by rapid thermal and furnace anneals".** *Appl Phys Lett* 1999, **74**:1866.
4. Fojtik P, Dohnalová K, Mates T, Stuchlík J, Gregora I, Chval J, Fejfar A, Kočka J, Pelant I: **"Rapid crystallization of amorphous silicon at room temperature".** *Philos Mag B* 2002, **82**:1785.
5. Yoon SY, Park SJ, Kim KH, Jang J: **"Metal-induced crystallization of amorphous silicon".** *Thin Solid Films* 2001, **383**:34.
6. Trojánek F, Neudert K, Bittner M, Malý P: **"Picosecond photoluminescence and transient absorption in silicon nanocrystals".** *Phys Rev B* 2005, **72**:075365.
7. Fejfar A, Mates T, Čertík O, Rezek B, Stuchlík J, Pelant I, Kočka J: **"Model of electronic transport in microcrystalline silicon and its use for prediction of device performance".** *J Non-Cryst Solids* 2004, **338**:303.
8. Tan YT, Kamiya T, Durrani ZAK, Ahmed H: **"Room temperature nanocrystalline silicon single-electron transistors".** *J Appl Phys* 2003, **94**:633.
9. Bisi O, Ossicini S, Pavesi L: **"Porous silicon: a quantum sponge structure for silicon based optoelectronics".** *Surf Sci Rep* 2000, **38**:1.
10. Rezek B, Šípek E, Ledinský M, Krejza P, Stuchlík J, Kočka J: **"Spatially localized current-induced crystallization of amorphous silicon films".** *J Non-Cryst Solids* 2008, **354**:2305.
11. Rezek B, Šípek E, Ledinský M, Stuchlík J, Vetushka A, Kočka J: **"Creating nanocrystals in amorphous silicon using a conductive tip".** *Nanotechnology* 2009, **20**:045302.
12. Verveniotis E, Rezek B, Šípek E, Stuchlik J, Kočka J: **"Role of current profiles and AFM probes in electric crystallization of amorphous silicon".** *Thin Solid Films* 2010, **518**:5965.
13. Luterová K, Pelant I, Fojtík P, Nikl M, Gregora I, Kočka J, Dian J, Valenta J, Malý P, Kudrna J, Štěpánek J, Poruba A, Horváth P: **"Visible photoluminescence and electroluminescence in wide-band gap hydrogenated amorphous silicon".** *Philos Mag B* 2000, **80**:1811.
14. Rezek B, Mates T, Stuchlík J, Kočka J, Stemmer A: **"Charge storage in undoped hydrogenated amorphous silicon by ambient atomic force microscopy".** *Appl Phys Lett* 2003, **83**:1764.
15. Rezek B, Stuchlík J, Fejfar A, Kočka J: **"Microcrystalline silicon thin films studied by atomic force microscopy with electrical current detection".** *J Appl Phys* 2002, **92**:587.
16. Vetushka A, Feifar A, Ledinský M, Rezek B, Stuchlik J, Kočka J: **"Comment on "Current routes in hydrogenated microcrystalline silicon"".** *Phys Rev B* 2010, **81**:237301.
17. Kim SK, Lee HH: **"Intrinsic phase boundary between amorphous and crystalline structures for chemical vapor deposition".** *J Cryst Growth* 1995, **151**:200.
18. Kočka J, Fejfar A, Mates T, Fojtík P, Dohnalová K, Luterová K, Stuchlík J, Stuchlíková H, Pelant I, Rezek B, Stemmer A, Ito M: **"The physics and technological aspects of the transition from amorphous to microcrystalline and polycrystalline silicon".** *Phys Status Solidi C* 2004, **1**:1097.

19. Ledinský M, Vetushka A, Stuchlík J, Mates T, Fejfar A, Kočka J, Štěpánek J: **"Crystallinity of the mixed phase silicon thin films by Raman spectroscopy".** *J Non-Cryst Solids* 2008, **354**:2253.
20. Ivlev G, Gatskevich E, Cháb V, Stuchlík J, Vorlíček V, Kočka J: **"Dynamics of the excimer laser annealing of hydrogenated amorphous silicon thin films".** *Appl Phys Lett* 1999, **75**:498.

doi:10.1186/1556-276X-6-145
Cite this article as: Verveniotis *et al.*: Impact of AFM-induced nano-pits in a-Si:H films on silicon crystal growth. *Nanoscale Research Letters* 2011 **6**:145.

Submit your manuscript to a SpringerOpen journal and benefit from:

► Convenient online submission
► Rigorous peer review
► Immediate publication on acceptance
► Open access: articles freely available online
► High visibility within the field
► Retaining the copyright to your article

Submit your next manuscript at ► springeropen.com

Journal of Non-Crystalline Solids 358 (2012) 2118–2121

Contents lists available at SciVerse ScienceDirect

Journal of Non-Crystalline Solids

journal homepage: www.elsevier.com/ locate/ jnoncrysol

Generating ordered Si nanocrystals via atomic force microscopy

Elisseos Verveniotis *, Emil Šípek, Jiří Stuchlík, Jan Kočka, Bohuslav Rezek

Institute of Physics ASCR, Cukrovarnicka 10, 16200, Prague 6, Czech Republic

ARTICLE INFO

Article history:
Received 20 August 2011
Received in revised form 22 November 2011
Available online 28 December 2011

Keywords:
AFM
CS-AFM
a-Si:H
Electric crystallization
Nickel

ABSTRACT

We describe two successful routes for generating ordered arrays of Si nanocrystals by using atomic force microscopy (AFM) and amorphous silicon thin films (200–400 nm) on Ti/Ni coated glass substrates. First, we show that field-enhanced metal-induced solid phase crystallization at room temperature can be miniaturized to achieve highly spatially localized (below 100 nm) current-induced crystallization of the amorphous silicon films using a sharp tip in AFM. In the second route, resistive nano-pits are formed at controlled positions in the amorphous silicon thin films by adjusting (lowering and/or stabilizing) the exposure currents in the AFM process. Such templated substrates are further used to induce localized growth of Si nanocrystals in plasma-enhanced chemical vapor deposition process. In both cases the crystalline phase is identified in situ as features of enhanced current in current-sensing AFM maps.

© 2011 Elsevier B.V. All rights reserved.

1. Introduction

Production of silicon nanocrystals has become increasingly important as they are attractive for nanoelectronic, optoelectronic [1,2], as well as biological applications [3,4]. Usually they are produced in a form of so-called micro-crystalline silicon thin films using chemical vapor deposition (CVD) [5,6] or by electrochemical etching of bulk monocrystalline silicon [7] via formation of porous silicon [8]. Yet producing nanocrystals in well-defined locations or creating arranged microscopic patterns as desired for optical and electronic applications still remains a challenge.

Field-enhanced [9,10] metal-induced [11] solid phase crystallization (FE-MISPC) at room temperature can be used to achieve spatially localized current-induced crystallization of amorphous silicon films using a sharp tip such as those employed in atomic force microscopy (AFM) [12]. This process results in the formation of microscopic crystalline rings and dots as well as resistive nano-pits at controlled positions in the amorphous silicon thin films. The smallest sizes of the crystallized objects ranged from several hundreds of nanometers to several micrometers. Such relatively large size was due to electrical discharge from the inherently present parallel capacitance, caused by a drastic increase of local conductivity during the process. Limiting of the maximum current level by using a MOSFET with a feedback circuit enabled to localize crystallization below 100 nm [13]. However, perfectly stabilized electrical current during the FE-MISPC process produced rather non-conductive pits [14]. Although current-sensing AFM (CS-AFM) and micro-Raman spectroscopy proved the crystalline character of FE-MISPC features, material purity is questionable due to Nickel silicide being involved in the FE-MISPC process.

Compared to FE-MISPC, CVD process can produce more defined nanocrystalline material [5,6] with the possibility to tailor its structural and electronic properties, e.g. by doping. Recently, we have demonstrated that both conductive and non-conductive pits created by FE-MISPC can be utilized to induce selective nucleation and growth of Si nanocrystals on a-Si:H substrates by CVD [15].

In this paper, we review the above two routes with the focus on generating ordered arrays of Si nanocrystals in amorphous silicon thin film matrix by using AFM with electrical current application and sensing. We discuss factors influencing nanocrystal formation and possibilities for further improvements.

2. Materials and methods

The a-Si:H films are deposited by plasma-enhanced chemical vapor deposition in a thickness of 170–400 nm (±30 nm, measured by a stylus profilometer) on a Corning 7059 glass substrate coated with 40 nm thin nickel film and 10 nm titanium interlayer for improved adhesion to glass. Substrate temperature of 50 °C and 0.02% dilution of SiH_4 in helium result in a hydrogen content of 20–45 at.% in the films [16]. The relatively high hydrogen content is essential for enabling the FE-MISPC process [9].

AFM is used to position conductive tips in controlled locations and in electrical contact with the a-Si:H film. Various types of tips are used: Pt/Cr-coated doped silicon, plain silicon, conductive diamond-coated silicon and bulk ultrananocrystalline diamond (UNCD) tips. UNCD tips did exhibit superior durability when compared to Si or metal/diamond-coated Si tips but the crystallization results were very similar irrespective of the type used. In addition we found that FE-MISPC is destructive for all kinds of tips since they lose their

* Corresponding author. Tel.: +420 220 318 433.
E-mail address: verven@fzu.cz (E. Verveniotis).

0022-3093/$ – see front matter © 2011 Elsevier B.V. All rights reserved.
doi:10.1016/j.jnoncrysol.2011.12.018

apex after a small number of expositions [14]. All tips are produced and available commercially. Typical tip radius is 10–70 nm depending on the type used. Spring constant of cantilevers, on which the tips are integrated, is between 0.2 Nm^{-1} and 22.5 Nm^{-1}. The contact force is thus between 10 and 500 nN.

Configuration of the experimental setup with various current control options is shown in Fig. 1. Electrical current is applied to the bottom Ni/Ti electrode in the range of −50 pA to −3 nA. The Ni/Ti electrode is negatively biased in order to facilitate the FE-MISPC process [9]. Anodic oxidation of the silicon film is thus excluded under such conditions [17,18]. The constant current I_c supplied by the current source (Keithley K237) does not directly correspond to the sample current I_s. The I_c charges also a parallel capacitance C_p which arises inherently from the wire leads and is typically 10–50 pF. Vice versa, when sample resistivity decreases (e.g. due to the crystallization process) the charge on parallel capacitance contributes to I_s so that it can considerably exceed the I_c value. Therefore, the sample current I_s is measured independently by an additional picoamperemeter (I_s preamplifier) in the tip-sample branch of the circuit. The tip-sample capacitance C_s is in the order of aF and thus its influence is negligible compared to C_p.

The setup can drive electrical current for the FE-MISPC process in three different regimes: A) the current is controlled by the current source unit so that I_c corresponds to the current set-point value and the pre-amp output is used only to monitor the process and total energy dose [12], B) the current is controlled by an additional regulation circuit composed of a metal-oxide-semiconductor field-effect transistor (MOSFET) and proportional feedback loop (P-FL, shown in brown) which adjusts MOSFET gate to keep actual sample current I_s below the set-point value by using the pre-amp output [13], C) for the highest precision and speed the current is controlled by the regulation circuit with derivative feedback loop (PD-FL), a reference signal generator, and an adder for summing the pre-amp output with the reference (all these components are shown in green) [14]. FE-MISPC process is characterized by temporal current profile (bias voltage is adjusted correspondingly by the current source unit) and total energy dose [14].

After the FE-MISPC process a second silicon layer was deposited in some cases on the top of processed film in the thickness of about 200 nm (±30 nm). This deposition is done at 100 °C at the boundary condition of amorphous and micro-crystalline silicon growth [19,20].

Microscopic morphology and local conductivity of the films before and after the FE-MISPC process are characterized by CS-AFM [21] using sample bias voltage of −25 V. Increased local current as detected by CS-AFM is a good indication of crystallinity as corroborated previously by micro-Raman spectroscopy [12,13,15]. We are using such high bias voltage due to low conductivity of the a-Si:H film and additional tunneling barrier of the native oxide on the film surface [18].

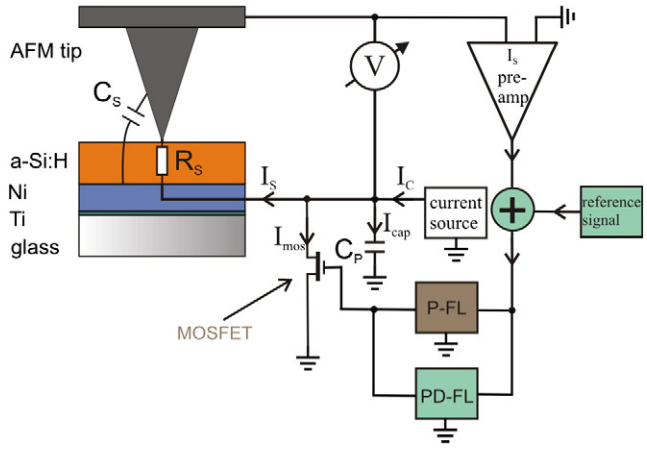

Fig. 1. Schematic drawing of the experimental setup with various current control options.

3. Results

In Fig. 2(a, b) we can see the typical outcome of a FE-MISPC experiment when the setup was utilized in regime A (without MOSFET regulation). A micron sized irregular pit was formed in the a-Si:H film. The current map (Fig. 2(b)) indicates that there are regions of increased conductivity exhibiting electrical current up to −15 pA vs. few hundreds of fA of the amorphous surroundings. However, these regions are not confined nor cover all the formed pit area as they extend on various places in its vicinity. Conductivity of these regions is related with crystalline silicon as corroborated by CS-AFM [21] and micro-Raman spectroscopy [12,13,15]. Constant current was set to $I_c = -250$ pA. The I_s profile during exposition (Fig. 2(c)) shows that the actual sample current is below this value but suddenly exceeds I_c by up to a factor of 6. This sample current spike is caused by discharges from the parasitic parallel capacitance C_p and thus cannot be controlled by the current source.

Fig. 3(a, b) shows an array of crystallized features created using control regime B where the MOSFET protection with P-FL is enabled. Constant current was set to $I_c = -200$ pA. The regulation circuit assisted in shunting random C_p discharges and thereby limited the sample current so that it fluctuated under the I_c set-point [typical profile in Fig. 3(c)]. This improved reproducibility of the features generated by FE-MISPC is seen in topography as well as current maps in Fig. 3(a, b). The current limitation also consistently reduced the size of the features to sub-μm dimensions and in some instances the crystalline features were as small as 60 nm [13].

Results of the experiments utilizing the full setup (regime C) can be seen in the AFM/CS-AFM images in Fig. 4(a, c). Source current was set to $I_c = -100$ nA. We can see that the sample current temporal profile is well stabilized to the set-point value (−0.5 nA) without fluctuations (Fig. 4(g)). Yet pits formed by the process do not exhibit increased conductivity and thus represent only deformations on the amorphous tissue (diameter 300 nm, depth 50 nm). Such features were reported before [12] when the sample current set-point (−50 pA) and energy transfer rate (0.5 nJ/s) were low. However, here the reason is not the low sample current but rather perfectly stabilized exposition current at a predefined set-point as shown in the temporal profile in Fig. 4(g).

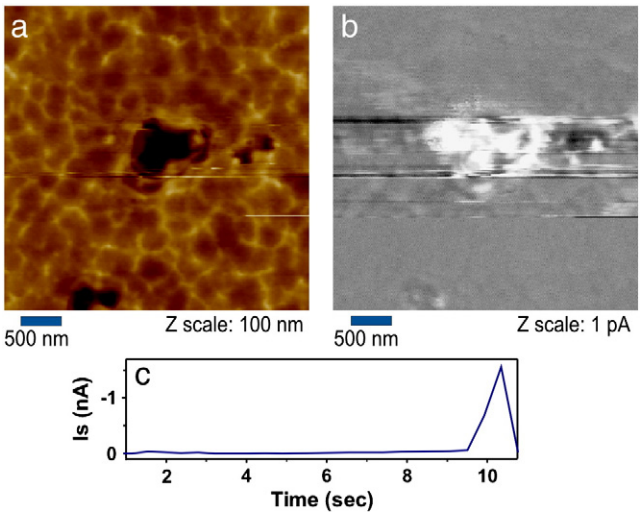

Fig. 2. (a) AFM topography and (b) current map after a FE-MISPC experiment without current regulation. (c) Typical sample current temporal profile during FE-MISPC experiments. Current set-point was −250 pA.

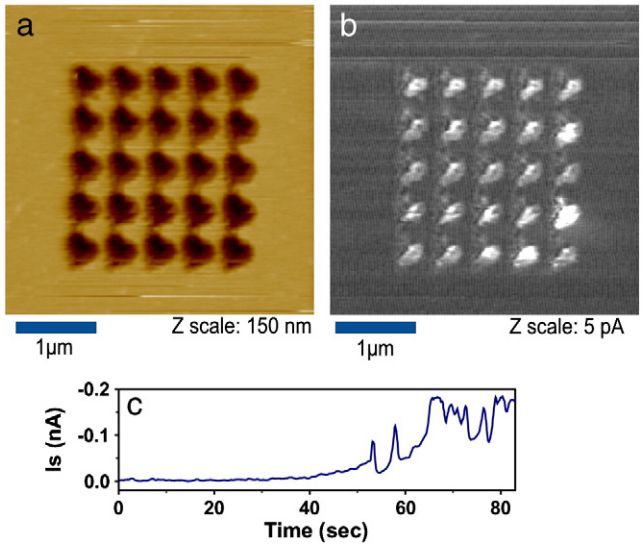

Fig. 3. (a) AFM topography and (b) current map of a 5×5 array made by consecutive FE-MISPC experiments utilizing the P-FL component of the MOSFET regulator. (c) Typical sample current profile for $I_c = -200$ pA. Source current for the nanocrystal array was −300 pA.

Thus we took advantage of the much better controllable nano-pit formation effect and used the array of well-defined and ordered but non-conductive nano-pits as nucleation sites for growth of silicon nanocrystals by CVD. Fig. 4(b, d) shows AFM and CS-AFM images of the above pits after deposition of the 2nd silicon layer by CVD at the boundary conditions of micro-crystalline/amorphous growth [respective cross sections in Fig. 4(e, f)]. The originally non-conductive pits then exhibited increased conductivity by an order of magnitude. This effect is focused in the pits where the crystals grew preferentially as detected by both AFM topography and CS-AFM current maps (Fig. 4(b, d)). This can be attributed to deposition of silicon nano- or micro-crystals inside the pits. Their dimensions are <50 nm as estimated by FWHM of the peaks in the local current profile.[Fig. 4(f)]. Depth of the pits also increased after second deposition but the

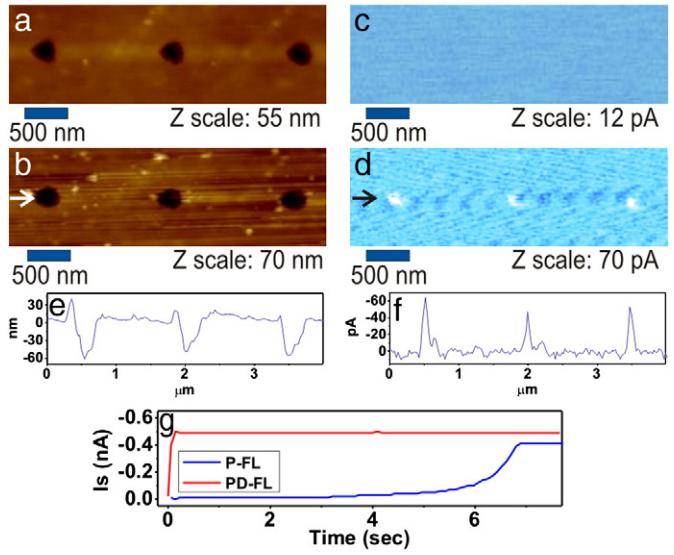

Fig. 4. (a) AFM topography and (c) current map after 3 FE-MISPC experiments utilizing the full regulation circuit. (b, d) Maps of the same features after the 2nd CVD deposition. (e, f) cross sections of the topography and current, respectively after the 2nd CVD deposition (indicated by arrows). (g) Typical sample current profiles for the different rise regimes. $I_s = 0.4$ nA (P-FL) and 0.5 nA (PD-FL). Source current in both cases was 100 nA.

alteration is smaller than the thickness of the deposited layer (10 nm vs. 200 nm). This indicates that there must be some growth occurring inside the pits as well. Note that the crystallinity of these features could not be confirmed by μ-Raman due to their small size. Given that the Raman focus is 700 nm, the crystalline regions are only a small fraction of it (0.5% at most) making them undetectable.

4. Discussion

When working with the initial experimental setup I_s was clearly unstable since C_p discharges were random and of varying magnitude. Thus the results were evaluated as a function of average transfer of energy rate [12]. The energy delivered to the work area is a function of the voltage developed in the current source (which is somehow controllable and depends to the source current value) and the sample current. The average transfer rate is thus defined as the total, preset energy dose delivered to the work area over the time that it took to deliver it. We experimented with various rates each yielding different results. Low energy transfer rates (0.5 nJ/s) resulted in small, non-conductive pits such as those of Fig. 4(a) while medium (6 nJ/s) generated larger, conductive areas (Fig. 2(a)). Further increase in the transfer rate (30 nJ/s) resulted in larger morphological deformations (~3 μm pits) with the conductive region forming a ring around the work area [12]. Note that higher energy transfer rates produced features both larger in diameter and deeper, with the experiments conducted at the highest setting (30 nJ/s) yielding pits which go through the whole silicon film [12].

Utilization of the MOSFET regulator (P-FL) clearly improved the reproducibility of the process due to the limitation of I_s which was not allowed to exceed the predefined set value [13]. Nevertheless the actual crystallized area slightly differs from spot to spot according to the current map (Fig. 3(b)) which shows variations in amplitude and dimensions of the conductive spots. This can be attributed to differences in fluctuations of the sample current during crystallization.

The nanocrystal formation by FE-MISPC is influenced by many factors such as properties of microscopic electrical contact in AFM, thermodynamics of crystallization, local cooling and silicide formation as preliminary described in Ref. [13]. With the aim to even better reproduced and smaller crystalline features as well as to study the local FE-MISPC process we employed the setup with further improved current control, regime C.

It is clear that PD-FL enables faster current rise to the current set-point compared to P-FL (200 ms vs. 7 s). By performing large number of experiments with stabilized current we found that in most cases (95%) they resulted in non-conductive pits (or nothing at all) regardless of the employed current control regime, current set-point (−0.1 nA to −3 nA), and energy transfer rate (up to 50 nJ/s) [14]. Hence allowing some fluctuations in the sample current, preferably with amplitude limitation such as in regime B, is necessary for crystallization by the FE-MISPC process. It is also noteworthy that even in the control regime C the sample current was not always stabilized. Spikes above the set-point current (in similarity to regime A) were observed in about 1/3 of all experiments [14]. This behavior can be most likely attributed to the randomness of the dielectric breakdown occurring during FE-MISPC process, which is hard to control to 100%. We detected crystallized features even when the current spike occurred in the very beginning of the process and overall delivered energy and/or set-point current was smaller than usual.

There are several factors that can promote nucleation and growth of silicon nanocrystals inside the previously non-conductive pits created by local FE-MISPC in regime C. First, growth precursors during the 2nd CVD deposition may become more localized inside the pits. Second, density of a-Si:H defects can be increased inside the pits due to local heating and/or evolution of hydrogen as in the case of laser annealing that also can promote further growth of crystalline silicon [22]. Third, local stress or strain may be increased inside the

pits and increase the nucleation probability. All these reasons can contribute to the observed effect but the impact of each of them in the process has yet to be elucidated. One could argue that the elevated temperature during 2nd deposition (100 °C) may also affect the crystallinity of the features. To resolve this effect we performed thermal annealing of a FE-MISPC-exposed sample. The annealing conditions were identical to the 2nd deposition conditions described above but without the plasma. We did not notice any effects on the structural or electronic properties of the previously resistive pits after annealing.

Electric crystallization relies on metal-silicide species which are formed either by elevated annealing temperature (MISPC) or by the application of an electric field (FE-MISPC). This means that contamination by Ni of the Si crystals formed immediately after exposition (Figs. 2, 3) is possible. Even though this could enhance the conductivity of the crystalline regions, the presence of spots exhibiting electrical current on CS-AFM images solely due to metal contamination can be excluded since 1) presence of Si crystals has been confirmed by Raman and 2) volume of the contaminant is most likely very small to be able to produce conductive regions by itself. In addition, the methodology with the secondary CVD deposition on initially a-Si pits (thus not contaminated) showed that the conductivity observed is solely due to the crystalline Si phase. Note that heavy contamination from metal-coated AFM tips can be excluded since FE-MISPC results are systematically consistent irrespective of the type of tip used [14].

One could critically point out the utilization of Transmission Electron Microscopy (TEM) as another confirmation of crystallinity. TEM data could be extremely useful, especially in the case of features produced by the secondary CVD deposition since μ-Raman is not sensitive enough to detect them due to their small size. However, the sample preparation for TEM makes impossible to find the FE-MISPC-induced features afterwards. Furthermore, given the small size of the crystalline features, it would be extremely difficult to thin the sample exactly on or at least very near the exposed regions.

Sources of errors in our methods and results are limited to: 1) modifications of the apex during FE-MISPC due to the destructive effect of the process on AFM tips [14], 2) randomness of the dielectric breakdown during FE-MISPC which does not allow for 100% result reproducibility [14] and 3) in situ changes in the tip-surface junction size and quality during CS-AFM scans, especially when scanning corrugated regions (e.g. inside the processed pits) [21]. We eliminate the first error factor by performing the post-FE-MISPC CS-AFM scans with a fresh tip and not with the one used for the actual exposition. Factor number two cannot be controlled and is the main reason for exposition current (I_s) instabilities observed in 62% of the experiments despite PD-FL utilization. Detailed statistical analysis can be found in Ref. [14]. Finally, the third possible error source could potentially influence the CS-AFM images due to: the non-constant tip-sample contact area when scanning corrugated surfaces, natural tip abrasion during scans, and imperfections in the FL of the microscope. Selecting low scan rates for CS-AFM (we typically use 0.1 Hz) and employing diamond-coated or UNCD tips can almost fully compensate for the slow FL and tip condition issues. Yet, even metal-coated tips showed remarkable durability in CS-AFM measurements of a-Si:H samples as long as scan speed and loading forces are kept reasonably low (<5 μm/s and few tens of nN, respectively). Problems with varying contact area can be minimized by using ultra-sharp AFM tips (radius<10 nm), thus keeping the effective contact size comparable in smooth and corrugated areas.

5. Conclusions

We showed that silicon nanocrystals can be generated in a-Si:H films with nanoscale precision by using two routes. In the first route the nanocrystals are created directly by FE-MISPC process via electrical current in AFM. It is noteworthy that so far the nanocrystals were characterized only from top. Their morphology and shape in the film volume where they are embedded is still unknown. Revealing of true shape and detailed composition of the crystallized features may bring more understanding of the local FE-MISPC process itself. Results of the FE-MISPC process do not depend on the type of employed AFM tips. Current fluctuations either over or under the exposition current set-point are necessary to initiate crystallization. In the case of perfectly stabilized current we observed mainly non-conductive (and thus non-crystalline) features in the form of nanoscale pits in a-Si:H film. In the second route, those pits were used as templates for CVD of nanocrystals. We have evidenced that both routes can produce arrays of crystalline features at predefined positions down to sub-100 nm sizes and accuracy. This opens prospects for ordered growth of silicon nanocrystals (and nanostructures in general) with demanded quality and properties.

Acknowledgements

Financial support from research projects KAN400100701 (ASCR), LC06040 (MŠMT), LC510 (MŠMT), SVV-2011-263307, 202/09/H041, AV0Z10100521, and the Fellowship J E Purkyně (ASCR) is gratefully acknowledged.

References

[1] J. Kočka, H. Stuchlíková, J. Stuchlík, B. Rezek, V. Švrček, P. Fojtík, I. Pelant, A. Fejfar, Solid State Phenom. 80–81 (2001) 213.
[2] N. Daldosso, L. Pavesi, Laser Photonics Rev. 3 (6) (2009) 508.
[3] P. Ji-Ho, G. Luo, G. von Maltzahn, R. Erkki, S.N. Bhatia, M.J. Sailor, Nat. Mater. 8 (2009) 331.
[4] F. Trojánek, K. Neudert, M. Bittner, P. Malý, Phys. Rev. B 72 (2005) 075365.
[5] A. Fejfar, T. Mates, O. Čertík, B. Rezek, J. Stuchlík, I. Pelant, J. Kočka, J. Non-Cryst. Solids 338 (2004) 303.
[6] Y.T. Tan, T. Kamiya, Z.A.K. Durrani, H. Ahmed, J. Appl. Phys. 94 (2003) 633.
[7] K. Kúsová, O. Cibulka, K. Dohnalová, I. Pelant, J. Valenta, A. Fučíková, K. Žídek, J. Lang, J. Englich, P. Matějka, P. Štěpánek, S. Bakardjieva, ACS Nano 4 (2010) 4495.
[8] O. Bisi, S. Ossicini, L. Pavesi, Surf. Sci. Rep. 38 (2000) 1.
[9] P. Fojtik, K. Dohnalová, T. Mates, J. Stuchlík, I. Gregora, J. Chval, A. Fejfar, J. Kočka, I. Pelant, Philos. Mag. B 82 (2002) 1785.
[10] S.Y. Yoon, S.J. Park, K.H. Kim, J. Jang, Thin Solid Films 383 (2001) 34.
[11] L.K. Lam, S. Chen, D.G. Ast, Appl. Phys. Lett. 74 (1999) 1866.
[12] B. Rezek, E. Šípek, M. Ledinský, P. Krejza, J. Stuchlík, J. Kočka, J. Non-Cryst. Solids 354 (2008) 2305.
[13] B. Rezek, E. Šípek, M. Ledinský, J. Stuchlík, A. Vetushka, J. Kočka, Nanotechnology 20 (2009) 045302.
[14] E. Verveniotis, B. Rezek, E. Šípek, J. Stuchlik, J. Kočka, Thin Solid Films 518 (2010) 5965.
[15] E. Verveniotis, B. Rezek, E. Šípek, J. Stuchlik, M. Ledinský, J. Kočka, Nanoscale Res. Lett. 6 (2011) 145.
[16] K. Luterová, I. Pelant, P. Fojtík, M. Nikl, I. Gregora, J. Kočka, J. Dian, J. Valenta, P. Malý, J. Kudrna, J. Štěpánek, A. Poruba, P. Horváth, Philos. Mag. B 80 (2000) 1811.
[17] B. Rezek, T. Mates, J. Stuchlík, J. Kočka, A. Stemmer, Appl. Phys. Lett. 83 (2003) 1764.
[18] A. Vetushka, A. Feifar, M. Ledinský, B. Rezek, J. Stuchlik, J. Kočka, Phys. Rev. B 81 (2010) 237301.
[19] S.K. Kim, H.H. Lee, J. Cryst. Growth 151 (1995) 200.
[20] J. Kočka, A. Fejfar, T. Mates, P. Fojtík, K. Dohnalová, K. Luterová, J. Stuchlík, H. Stuchlíková, I. Pelant, B. Rezek, A. Stemmer, M. Ito, Phys. Status Solidi C 1 (2004) 1097.
[21] B. Rezek, J. Stuchlík, A. Fejfar, J. Kočka, J. Appl. Phys. 92 (2002) 587.
[22] G. Ivlev, E. Gatskevich, V. Cháb, J. Stuchlík, V. Vorlíček, J. Kočka, Appl. Phys. Lett. 75 (1999) 498.

3.3 Combination of diamond nanocrystals with a-Si:H

For combination of diamond nanocrystals with amorphous or crystalline silicon thin films we took advantage of the knowledge obtained from the work described above. So far the research in this field has focused on boron-doped monocrystalline (BDD) or polycrystalline diamond (PCD) for heterojunction fabrication with a-Si:H [100-102] and SOD technology for heat dissipation [36]. Substituting BDD or PCD for intrinsic NCD could generally reduce fabrication cost and enable large area processing. In addition, implementation of nanocrystals may open novel prospects for sensing, biological or optoelectronic applications where isolated crystals play a fundamental role [103, 104].

3.3.1 Nucleation and growth of NCD on a-Si

As substrates for diamond nanocrystal growth we used the a-Si:H samples described in section 3.2. The substrates were untreated prior to NCD growth. This was unlike the samples used for diamond charging which were seeded by diamond nanopowder. The untreated substrates were preferred because they result in spontaneous nucleation (i.e. in formation of individual crystals) rather than in continuous films. NCD was deposited in the linear plasma reactor at 250-750 ^{o}C. Deposition time was 24 h. Pressure was 0.1-1 mbar and CH_4:CO_2:H concentrations 5:20:200 sccm. Nucleation density as well as nanocrystal size and geometry were evaluated by SEM. Micro-Raman spectroscopy was used to detect diamond and determine the phase (crystalline or amorphous) of the underlying silicon after NCD deposition. AFM/KFM measurements were implemented for further microscopic evaluation of nanocrystals undetectable by micro-Raman.

Figure 3.1 (a) shows an SEM micrograph of NCD deposited at 250 ^{o}C, 0.1 mbar. We used such growth temperature to avoid metal-induced solid phase crystallization. The crystals are essentially 100 nm or smaller clusters composed of several smaller nanocrystalites. Micro-Raman was unable to detect diamond or graphitic phase on such samples. However, the simultaneous AFM topography/phase measurements shown in Figure 3.1 (b, c) indicate that the deposited nanocrystals

exhibit phase contrast different from the substrate. This means that the substrate and the nanocrystals are essentially different materials.

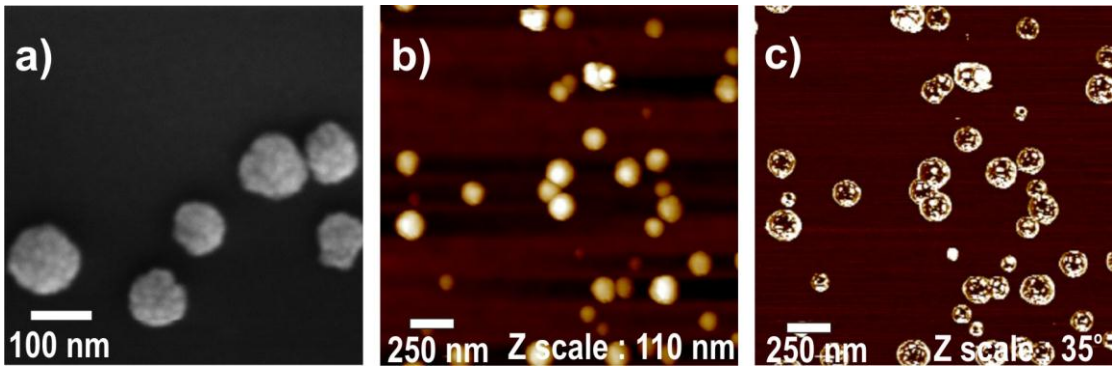

Figure 3.1 (a) SEM micrograph of NCD grown on a-Si:H at 250 ^{o}C, 0.1 mbar. (b, c) AFM topography and phase on the same sample.

Micro-Raman was unable to provide direct evidence of diamond phase most likely due to resolution limitations: an isolated nanocrystal is four times (or more) smaller than the available micro-Raman focus (wavelength 442 nm, spot size ~400 nm) meaning that it occupies at best only 6% of the probed spot size. In addition, the nanocrystals are on a silicon substrate 200-400 nm thick while their height is around 100 nm (from AFM topography). Given that the Raman signal is obtained by the full sample thickness (theoretical characterization limit is ~1 μm) and assuming that the signal is collected from a cylinder with the radius of the Raman laser and height of the film thickness, a diamond nanocrystal comprises at best only 1.5-3 % of the total volume.

With the above in mind we used the samples with the small nanocrystals as substrates for another deposition of NCD in order to enlarge the crystals to Raman-detectable sizes (nanocrystals already present act as nucleation sites). The results can be seen in the SEM micrographs in Figure 3.2 (a, b). Deposition parameters were 350 ^{o}C, 0.1 mbar and 750 ^{o}C, 1 mbar, respectively. In both cases the nanocrystal enlargement of the initial deposited features was successful. The crystals deposited in the pressure of 0.1 mbar appear irregular with fine, "cauliflower-like" structure. Their 1 mbar counterparts exhibit more homogeneous, spherical structure. Note that the geometrical differences are mostly attributed to the pressure [105] and not

temperature [58]. Size of each crystal (or cluster) is around 400 nm. Despite their larger size, those crystals are also comprised of small nanocrystalites.

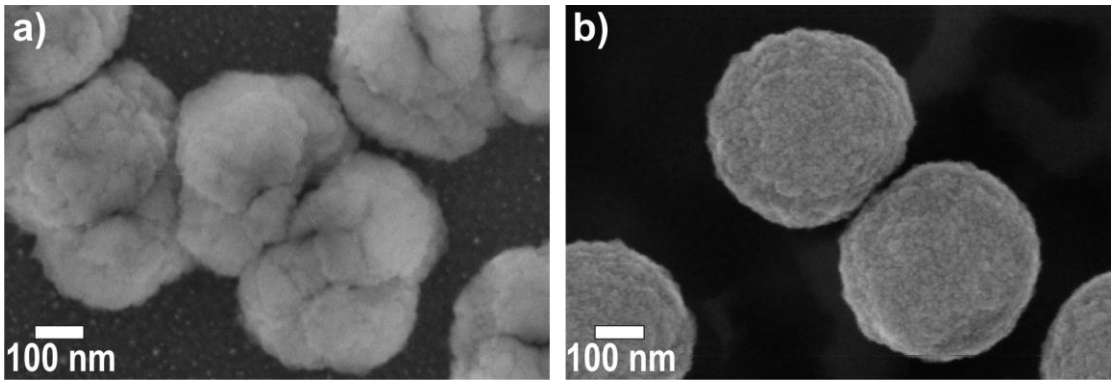

Figure 3.2 SEM micrographs of NCD grown on a-Si:H at (a) 350 ^{o}C, 0.1 mbar and (b) 750 ^{o}C, 1 mbar.

Micro-Raman spectroscopy measured on the samples illustrated in Figure 3.2 can be seen in Figure 3.3. Both specimens show clear peaks evidencing the presence of diamond and graphite. Nevertheless, the sample deposited at lower temperature exhibits sharper sp^3 peak in agreement with previous results [80]. It is noteworthy that at 750 ^{o}C the amorphous silicon substrate was fully crystallized. On the contrary, deposition at 350 ^{o}C preserved the amorphous nature of the film which indicates that the initial deposition at 250 ^{o}C also left the substrate amorphous.

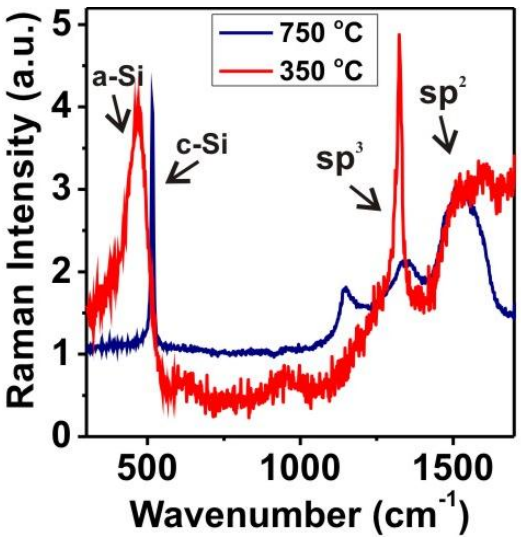

Figure 3.3 Raman spectra measured on the samples illustrated in Figure 3.2.

Figure 3.4 (a, b, c) shows SEM micrographs of NCD grown on untreated a-Si (i.e. without the prior deposition at 250 ^{o}C as before) after CVD at 250 ^{o}C, 350 ^{o}C and 750 ^{o}C, respectively. Pressure was kept at 0.1 mbar for all three separate depositions. We can see that as the temperature rises, nucleation density declines. This is explained by nucleation kinetics. Since the growth here is merely spontaneous (clean substrates before CVD), there are no nucleation sites for the carbon atoms to bond to. Elevated temperature causes the etching agents in the reaction (atomic H and also O from CO_2) to be more active. This has pronounced impact in the very first nucleation steps as the newly deposited carbon species are more likely to be etched away before additional carbon atoms have the chance to bond on them. This is clearly evidenced in Figure 3.4 where the highest nucleation density is observed at 250 ^{o}C.

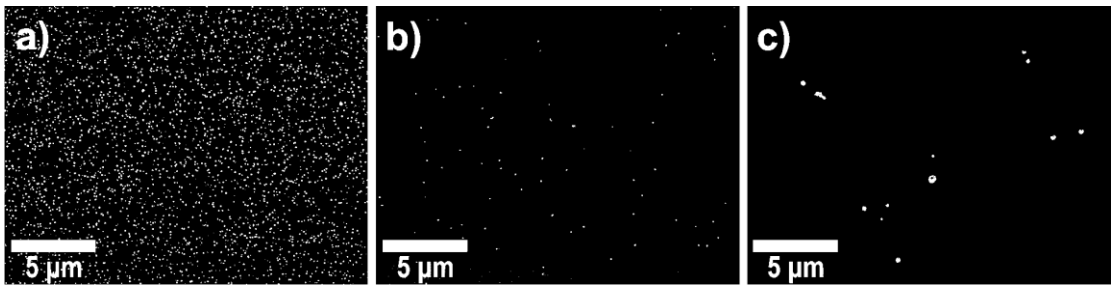

Figure 3.4 (a, b, c) SEM micrographs of NCD grown on untreated a-Si after CVD at 250 ^{o}C, 350 ^{o}C and 750 ^{o}C, respectively.

The findings in Figure 3.4 also evidence that dense packing of grains in Figure 3.2 is not due to the adjusted deposition conditions but due to the previous deposition at 250 ^{o}C. Hence, the nanocrystals deposited initially at 250 ^{o}C are indeed carbon species because they acted as nucleation sites for the second diamond deposition. It is obvious that carbon atoms are more strongly bound to each other than to the substrate during CVD (Volmer-Weber island growth) [45].

3.3.2 Selective growth of diamond nanocrystals

With all the above in mind we used an amorphous silicon sample from those in chapter 3.2.2 for selective diamond deposition in FE-MISPC-induced features. The whole processing of the sample can be seen in Figure 3.5. The a-Si:H sample was

used for FE-MISPC in AFM. The results are shown in the topography and current map in Figure 3.5 (a, b). The pronounced electrical current in the exposed areas vs. the substrate clearly demonstrates the effectiveness of the silicon nanocrystallization process [83]. After that we performed the 2nd silicon deposition (mixed-phase film). The AFM topography in Figure 3.5 (c) after the secondary deposition shows the accumulation of nanocrystalline silicon grains around the pits. The corresponding C-AFM image shown in Figure 3.5 (d) indicates a vast increase in the electrical current in the pits (nA vs. pA) in agreement with the results presented in chapter 3.2.2.

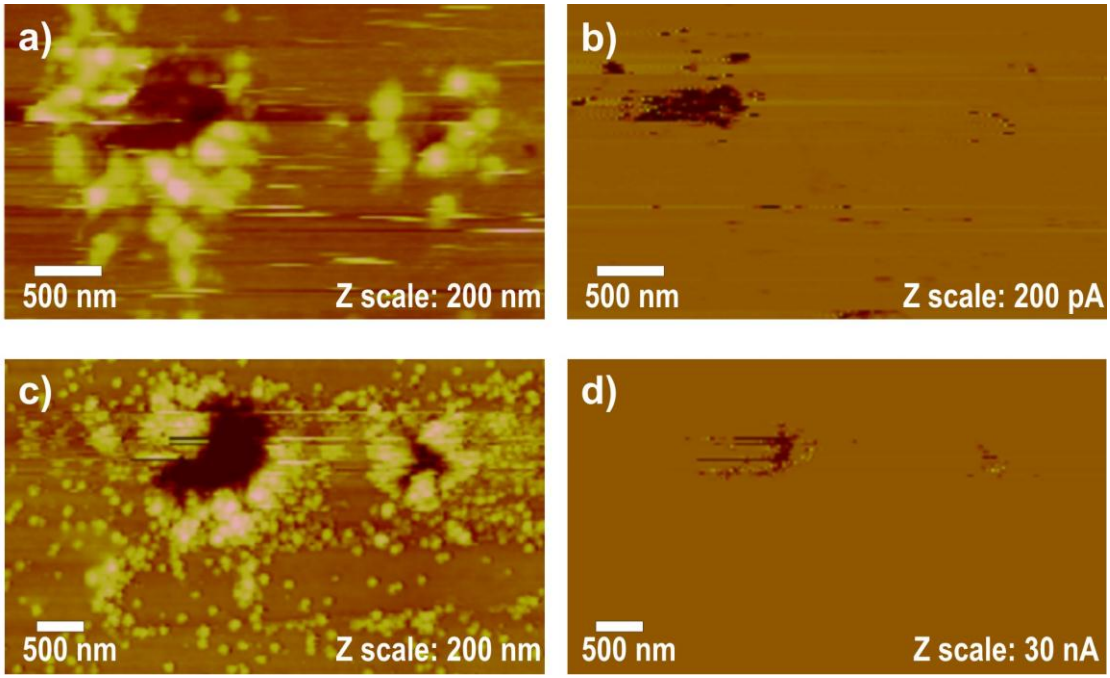

Figure 3.5 (a, b) AFM topography and current map, respectively measured on a-Si:H after two FE-MISPC experiments. (c, d) AFM topography and current map, respectively measured on the same spot after the mixed phase silicon film CVD.

After the silicon processing we performed a 3rd CVD for diamond deposition. Based on the results in Figure 3.4, we deposited the diamond at 250 ^{o}C due to the better crystal size (~ 100 nm) and nucleation density it exhibits as seen in Figure 3.4. Topography after the diamond CVD shown in Figure 3.6 (a) looks similar like before [Figure 3.5 (c)], as if no additional species were deposited. Nevertheless, AFM measurements far away from the FE-MISPC-induced features (i.e. several tens of μm away) evidenced the deposition of diamond with structure similar as in Figure 3.1.

C-AFM measurements on such samples do not provide evidence for diamond growth as the differences in conductivity can occur for various reasons, such as presence of graphite, diamond crystals or local phase transitions of silicon due to the elevated deposition temperature. For this reason we preferred KFM evaluation after the diamond deposition.

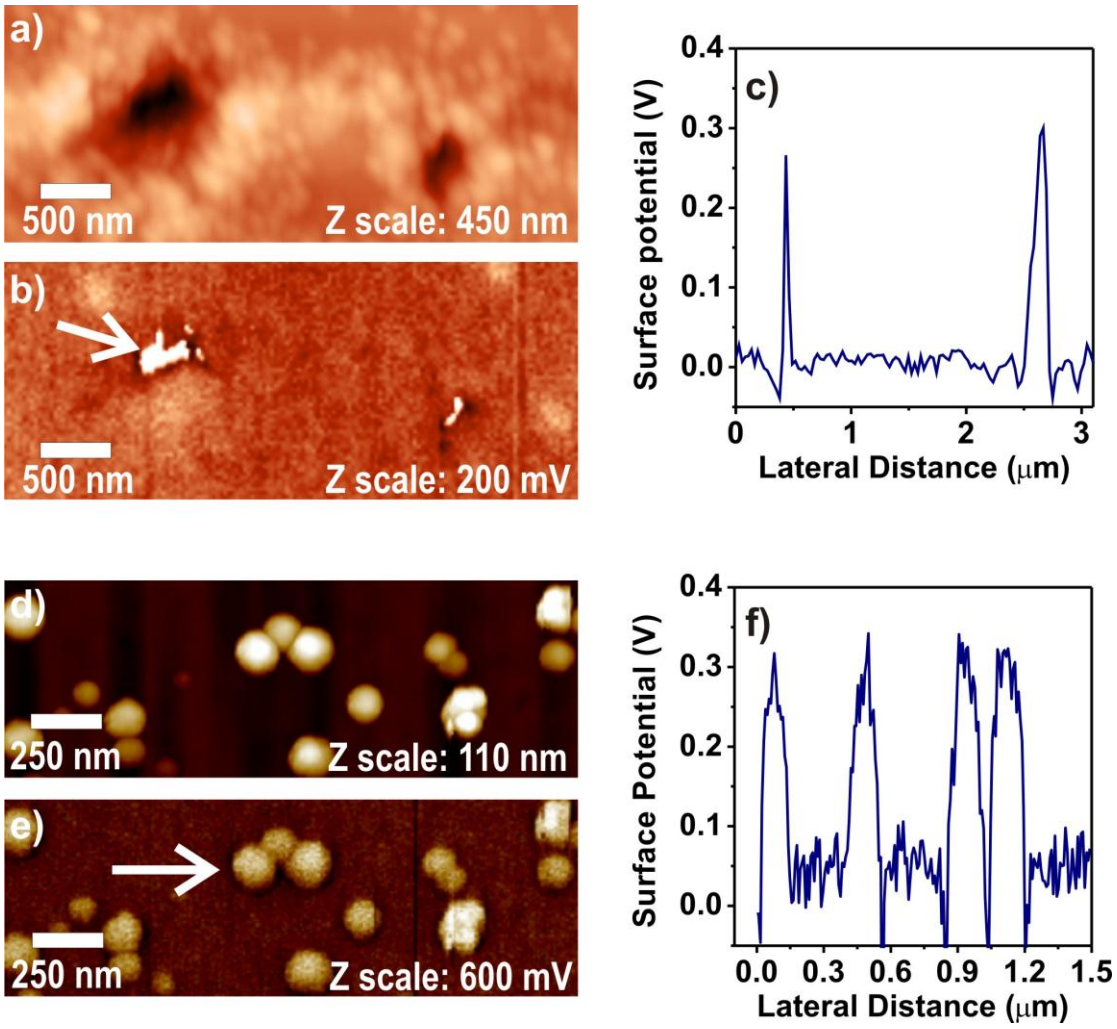

Figure 3.6 (a, b) AFM topography and KFM after the diamond CVD on the FE-MISPC-templated a-SI:H sample shown in Figure 3.5 (c, d). (c) Spatial profile measured on the KFM map as indicated by the arrow on it. (d, e) AFM topography and KFM after the diamond CVD on pristine a-Si:H. (f) Spatial profile measured on the KFM map as indicated by the arrow on it.

The pronounced signal in the KFM image shown in Figure 3.6 (b) [corresponding topography is in Figure 3.6 (a)] indicates that there is some material

accumulated inside the pits which is different than the a-/μc-Si surroundings. The surface potential difference of that material vs. the surroundings is around 300 mV, as seen in the spatial profile indicated by the arrow in the KFM image, plotted in Figure 3.6 (c).

Surface potential map of the diamond grains deposited at 250 ^{o}C on a clean a-Si sample (without FE-MISPC processing and/or secondary silicon deposition) can be seen in Figure 3.6 (e) [corresponding topography is in Figure 3.6 (d)]. The corresponding spatial profile from this KFM image, shown in Figure 3.6 (f), indicates that surface potential difference of the diamond grains vs. the substrate is also around 300 mV. This provides indirect evidence of deposited carbon species inside the pits. Nevertheless, micro-Raman could not detect diamond phase, in agreement with the previous measurements on samples deposited at 250 ^{o}C. With that in mind we performed an additional CVD at 250 ^{o}C in order to increase the diamond crystals to sizes detectable by Raman.

Micro-Raman spectra in figure 3.7 were measured after the 2nd diamond deposition. The red spectrum indicates the presence of diamond nanocrystals with pronounced graphitic content inside the larger pit. Measurements performed far from the FE-MISPC-induced features, however, evidence a strong sp^3 bonded carbon signal which corresponds to diamond (blue spectrum). This means that the mechanism of CVD deposition in FE-MISPC-induced features is different for silicon and diamond. While silicon nanocrystals nucleate selectively within and around the pits, diamond appears to prefer pristine surfaces. We speculate that diamond nanocrystals prefer to grow on less stress/strained surfaces as opposed to silicon nanocrystals that prefer the exact opposite. Nevertheless, by examining the vicinity of the pits, we saw that the diamond growth was well localized inside the pits.

In summary, we showed that it is possible to control spontaneous nucleation of diamond nanocrystals on a-Si:H at 250 ^{o}C. The low temperature preserves the amorphous silicon substrate and results in sub-100 nm grains. The geometry and material composition of the diamond can be tailored by the deposition conditions. We also showed that FE-MISPC-induced pits in a-Si:H can be used to guide the selective growth of nanocrystals with pronounced graphitic content inside the pits. Further work is still needed to elucidate the mechanism of diamond growth in such features, for instance by using pristine pits without Si nanocrystal deposition, or by further

experimentation with the diamond deposition parameters (CH_4 dilution, pressure, temperature).

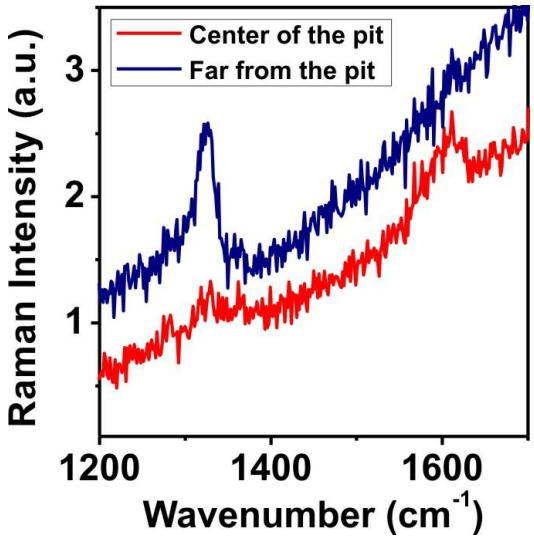

Figure 3.7 Raman spectra measured on the sample illustrated in Figure 3.6 (a, b) after the secondary diamond deposition. The red spectrum mas measured in the center of the large pit while the blue spectrum was measured in a place far away from the FE-MISPC features.

4. Conclusions

This thesis summarizes the research conducted towards fabrication, characterization and control of local (down to nanoscale) structural, electronic and chemical properties of silicon and nanocrystalline diamond. This was achieved by a range of methods such as atomic force microscopy, micro-Raman spectroscopy and chemical vapor deposition. The two mainly investigated systems were:

1. *Nanocrystalline diamond for local electrostatic charging and nanoparticle/nanodevice assembly.*
2. *Hydrogenated amorphous silicon for local nanocrystallization via FE-MISPC and ordered formation of nanocrystals by CVD.*

The study of NCD charging provided us with the means for an in-depth investigation of its electronic properties. We resolved that electronic transport in NCD occurs predominantly due to the presence of grain boundaries and thus sp^2 bonded carbon. Graphitic phase within the diamond is also responsible for the charges that become trapped within the material during the application of an electric field.

With the above in mind we used NCD films with high graphitic content in order to trap as many charges in the material as possible. We found that when the electrostatic field exerted by those charges is high enough, the NCD becomes a functional interface for self-assembly of nanoparticles via electrostatic attraction/repulsion. The minimum field strength needed for such assembly is at least 3 times smaller than reported before on dielectric materials [41]. This has the potential to enable assembly of nanostructures, nanosensors and nanodevices that will benefit from the unique properties of the underlying diamond substrate.

Pronounced fluctuations in the amplitude of NCD charging were resolved by close correlation between material properties (morphology and chemical composition) and the rest of the experimental parameters (AFM tips, bias voltage and electrical current). We identified tip-surface junction quality instabilities as the main factor behind sudden contrast changes within a single experiment and the initially poor reproducibility between similar experiments.

The issue above was solved by employing charging with constant current, which showed consistent and remarkably reproducible results between experiments. This was due to the exposure of the sample to similar number of charge carriers in spite of overall conductivity fluctuations due to material properties and tip-surface junction instability. Nevertheless, field-induced detrapping was identified as another factor influencing the charging process. It indicates that the experimental parameters have to be selected with mind in keeping the applied voltage low to limit the effects of detrapping. However, this inherently limits both diamond polarization and the number of states that can be occupied.

Concerning silicon nanocrystallization, we identified the crucial role and necessity of local dielectric breakdown which is expressed through current fluctuations during exposition for the local (nanoscale) crystallization of a-Si:H by electrical current (FE-MISPC process). This was provided by advanced control of local currents during FE-MISPC by exploring the various process parameters (current amplitude, surface treatment, material of AFM probes) and by thorough statistical analysis over a large number of experiments. We also showed that common, commercial AFM probes are not durable during the process (novel, bulk diamond probes were the most durable), yet this is not detrimental for successful nanocrystallization.

Finally, we demonstrated selective CVD growth of silicon and diamond nanocrystals within the FE-MISPC-induced nanoscale templates in a-Si:H. By this method we were able to further reduce the size of the crystalline silicon regions to < 50 nm for the case of the originally resistive nano-pits. In addition, the features that were already crystalline after FE-MISPC show a 6x increase in their electrical conductivity which evidences an increase in their crystallinity.

Diamond nanocrystals with pronounced graphitic content have been grown selectively inside crystalline silicon pits as measured by micro-Raman. These results can be used for systematic preferential growth of nanocrystals from diverse materials on pre-patterned a-Si:H templates. Such approach can be beneficial for nanoelectronic, optoelectronic and biological applications which require nanoscale precision in the positioning of nanocrystals on the substrate.

This work accomplished the aim of local structural, electronic and chemical characterization and modification of silicon and diamond. This was a necessary and important step towards the use and combination of silicon and diamond as functional

interfaces for assembly of nanodevices and fabrication of nanostructures. To that end, we:

- Self-assembled nanoparticles on microscopic, functionalized diamond surfaces by resolving the fine details in terms of material properties and experimental parameters which are necessary for such task.
- Performed selective growth of silicon nanocrystals in microscopic amorphous/crystalline silicon templates.
- Deposited selectively diamond nanocrystals with pronounced graphitic content in silicon thin film templates.

The progress reported here may provide important piece of knowledge for future research and applications of diamond and silicon nanostructures.

The author's contribution

The author participated in the designing of the samples used in this work. He performed all AFM, KFM and C-AFM measurements together with the subsequent image analysis and interpretation. He also did all the macroscopic electronic characterization and the occasional thermal evaporation. The author collected all the other data presented in this work and participated in their processing, evaluation and interpretation. The author is first and corresponding author in all articles enclosed in this thesis. He drafted the manuscripts and wrote the majority of the texts.

Bibliography

[1] M. Madou, Fundamentals of Microfabrication and Nanotechnology, CRC press (2012), ISBN 978-1-4200-5511-5.

[2] F. Laeri, F. Schüth, U. Simon and Wark, M. (eds), Host-Guest-Systems Based on Nanoporous Crystals, Wiley-VCH Verlag GmbH & Co. KGaA (2003), ISBN 978-3-5273-0501-8.

[3] M. Faraday, Researches in Electricity (1839).

[4] J. Kilby, Trans. Electron Devices, 23 (1976), 678.

[5] E. Ververiotis, Hyper-Threading Technology and its applications, Bachelor's thesis Technological Educational Institute of Larisa (2006).

[6] M. Ieong, B. Doris, J. Kedzierski, K. Rim and M. Yang, Science 306 (2004) 2057.

[7] F. Felgenhauern, M. Begoin and W. Mathis, Int. J. Numer. Model., 18 (2005) 313.

[8] H. Gottlob, T. J. Echtermeyer, M. Schmidt, T. Mollenhauer, T. Wahlbrink, M. C. Lemme and H. Kurz, Electrochem. Solid-State Lett. 11(2008) G12.

[9] J. Lau, Flip Chip Technologies, McGraw-Hill Professional (1995), ISBN 978-0-0703-6609-1.

[10] H. H. Lee; S.K. Kim, J. Cryst. Growth, 151 (1995) 200.

[11] A.T. Voutsas and M.K. Hatalis, Appl. Phys., 76 (1994) 777.

[12] J. Kočka , T. Mates, H. Stuchlíková, J. Stuchlík and A. Fejfar, Thin Solid Films, 501 (2006) 107.

[13] B. Rezek, J. Stuchlík, A. Fejfar, and J. Kočka, J. Appl. Phys., 92 (2002) 587

[14] J. Červenka, M. Ledinský, J. Stuchlík, H. Stuchlíková, S. Bakardjieva, K. Hruška, A. Fejfar and J. Kočka, Nanotechnology, 21 (2010) 415604.

[15] J. Červenka, M. Ledinský, H. Stuchlíková, J. Stuchlík, Z. Výborný, J. Holovský, K. Hruška, A. Fejfar and J. Kočka, Phys. Stat. Sol. RRL, 4 (2010) 37.

[16] B. Aufray, A. Kara, S. Vizzini, H. Oughaddou, C. Léandri, B. Ealet, G. Le Lay, Appl. Phys. Lett., 96 (2010) 183102.

[17] Th. Stelzner, G Andrä, E. Wendler, W. Wesch, R. Scholz, U. Gösele and S. Christiansen, Nanotechnology, 17 (2006) 2895.

[18] C. Leandri , G. Le Lay, B. Aufray, C. Girardeaux, J. Avila, M. E. Dávila, M. C. Asensio, C. Ottaviani and A. Cricenti, Surf. Sci., 574 (2005) L9.

[19] Si Chen and Shi-Li Zhang, J. Vac. Sci. Technol. A, 29 (2011) 011022.

[20] M. Ledinský, A. Fejfar, A. Vetushka, J. Stuchlík, B. Rezek, and J. Kočka, Phys. Stat. Sol. RRL, 5 (2011) 373.

[21] S. Koizumi, C. Nebel and M. Nesládek (eds), Physics and applications of CVD diamond, Wiley-VCH Verlag GmbH & Co. KGaA (2008) ISBN 978-3-5274-0801-6.

[22] C. E. Nebel, Nature Mater., 2 (2003) 431.

[23] S. Koizumi, M. Kamo, Y. Sato, H. Ozaki, and T. Inuzuka, Appl. Phys. Lett., 71 (1997) 1065.

[24] O.A. Williams, Diamond Relat. Mater., 20 (2011) 621.

[25] D. Ho (ed), Nanodiamonds: Applications in Biology and Nanoscale Medicine, Springer (2009), ISBN 978-1-4419-0530-7.

[26] B. Rezek, D. Shin, H. Uetsuka and C. E. Nebel, Phys. Stat. Sol. (a), 204 (2007) 2888.

[27] B. Rezek, L. Michalíková, E. Ukraintsev, A. Kromka and M. Kalbačova, Sensors, 9 (2009) 3549.

[28] A. Kromka, B. Rezek, Z. Remeš, M. Michalka, M. Ledinský, J. Zemek, J. Potměšil, and M. Vanecek, Chem. Vap. Deposition, 14 (2008) 181.

[29] H. Kozak, A. Kromka, O. Babchenko and B. Rezek, Sensor Lett. 8 (2010) 482.

[30] O. Babchenko, E. Verveniotis, K. Hruska, M. Ledinsky, A. Kromka and B. Rezek, Vacuum, 86 (2012) 693.

[31] A. Kromka, O. Babchenko, B. Rezek, M. Ledinský, K. Hruška, J. Potměšil and M. Vaněček Thin Solid Films, 518 (2009) 343.

[32] B. Rezek, M. Kratka, A. Kromka and M. Kalbacova, Biosens. Bioelectron., 26 (2010) 1307.

[33] H. Kawarada, M. Aoki and M. Ito, Appl. Phys. Lett., 65 (1994) 1563.

[34] D. A. J. Moran, D. A. MacLaren, S. Porro, H. McLelland, P. John, J. I. B. Wilson, Microelectron. Eng. 88 (2011) 2691.

[35] M. Rabarot, J. Widiez, S. Saada, J.-P. Mazellier, C. Lecouvey, J.-C. Roussin, J. Dechamp,P. Bergonzo, F. Andrieu, O. Faynot, S. Deleonibus, L. Clavelier, J. P. Roger, Diamond Relat. Mater., 19 (2010) 796.

[36] C. Hu and R. V. Mahajan, United States Patent No. US 7.126.822 B2, Oct. 24, 2006.

[37] E. Verveniotis, Fabrication of sub-100 nm electrodes for organic electronics, Master's Thesis, Bangor University (2007).

[38] A. T. Hubbard (ed), The Handbook of Surface Imaging and Visualization, CRC press (1995), ISBN 978-0-8493-8911-5.

[39] J. A. Zasadzinski, R. Viswanathan, L. Madsen, J. Garnaes and D. K. Schwartz, Science, 263 (1994) 1726.

[40] H. Fudouzi, M. Kobayashi, and N. Shinya, Adv. Mater. 14, 1649 (2002).

[41] P. Mesquida and A. Stemmer, Microelectron. Eng. 61, 671 (2002).

[42] E. Verveniotis, A. Kromka, M. Ledinský, J. Čermák and B. Rezek, Nanoscale Res. Lett., 6 (2011) 144.

[43] L. Ondič, K. Dohnalová, M. Ledinský, A. Kromka, O. Babchenko and B. Rezek, ACS Nano, 5 (2011) 346.

[44] F. Trojánek, K. Neudert, M. Bittner and P. Malý, Phys. Rev. B, 72 (2005) 075365.

[45] G. Cao, Nanostructures and Nanomaterials: Synthesis, Properties and Applications, Imperial College Press (2004), ISBN 978-1-8609-4480-2.

[46] J. Bloem, Proc. Seventh Conf. CVD, ECS PV 79-3, (1979) 41.

[47] J. J. Hajjar, R. Reif, and D. Adler, J Electron. Mater. 15 (1986) 279.

[48] K. F. Jensen and W. Kern, Thin Film Processes II, Academic Press (1991), ISBN 978-0-1272-8251-0.

[49] K. L. Choy, Prog. Mater. Sci. 48 (2003) 57.

[50] P. Ser, P. Kalck, and R. Feurer, Chem. Rev. 102 (2002) 3085.

[51] R. A. Street, Hydrogenated Amorphous Silicon, Cambridge University Press (2005), ISBN 978-0-5210-1934-7.

[52] D. L. Staebler and C. R. Wronski, Appl. Phys. Lett. 31 (1977) 292.

[53] D. L. Staebler and C. R. Wronski, J. Appl. Physics, 51 (1980) 3262.

[54] K. Luterová, I. Pelant, P. Fojtík, M. Nikl, I. Gregora, J. Kočka, J. Dian, J. Valenta, P. Malý, J. Kudrna, J. Štěpánek, A. Poruba, P. Horváth, Philos. Mag. B, 80 (2000) 1811.

[55] J. J. Gracio, Q. H. Fan and J. C. Madaleno, J. Phys. D: Appl. Phys., 43 (2010) 374017.

[56] M. Füner, C. Wild, and P. Koidl, Appl. Phys. Lett., 72 (1998) 1149.

[57] N. Neykova, H. Kozak, M. Ledinsky and A. Kromka, Vacuum 86 (2012) 603.

[58] A. Kromka, O. Babchenko, T. Izak, K. Hruska and B. Rezek, Vacuum 86 (2012) 776.

[59] P. W. May, Phil. Trans. R. Soc. Lond. A, 358 (2000) 473.

[60] M. Krátká, N. Neykova, E. Ukraintsev, A. Kromka and B. Rezek, Proc. of the XII. Workshop of Physical Chemists and Electrochemists (2012) 110, ISBN 978-80-7375-618-5.

[61] M. Morita, T. Ohmi, E. Hasegawa, M. Kawakami, and M. Ohwada, J. Appl. Phys. 68 (1990) 1272.

[62] A. Vetushka, A. Fejfar, M. Ledinský, B. Rezek, J. Stuchlík, J. Kočka, Phys. Rev. B 81 (2010), 237301.

[63] U. Kafader, H. Sirringhaus and H. von Känel, Appl. Surf. Sci., 90 (1995) 297.

[64] C. E. Nebel, B. Rezek, D. Shin, H. Watanabe, and T. Yamamoto, J. Appl. Phys. 99, (2006) 03371.

[65] M. Krátká, A. Kromka, E. Ukraintsev, A. Brož, M. Kalbacova and B. Rezek, Sens. Actuators B, 20 (2012) 239.

[66] B. Rezek, D. Shin, H. Watanabe and C. E. Nebel, Sens. Actuators B, 122 (2007) 596.

[67] H. Kawarada, Surf. Sci. Rep., 26, (1996) 205.

[68] F. Maier, M. Riedel, B. Mantel, J. Ristein, and L. Ley, Phys. Rev. Lett., 85 (2000) 3472.

[69] V. Chakrapani, J. C. Angus, A. B. Anderson, S. D. Wolter, B. R. Stoner, G. U. Sumanasekera, Science 318 (2007) 1424.

[70] B. Rezek, H. Watanabe and C. E. Nebel, Appl. Phys. Lett., 88 (2006) 042110.

[71] M. C. Rossi, F. Spaziani, S. Salvatori, G. Conte, Phys. Stat. Sol. (a), 199 (2003) 71.

[72] D. Takeuchi, H. Kato, G. S. Ri, T. Yamada, P. R. Vinod, D. Hwang, C. E. Nebel, H. Okushi, and S. Yamasaki, Appl. Phys. Lett., 86 (2005) 152103.

[73] P. Bergonzo , D. Tromson and C. Mer, Semicond. Sci. Technol., 18 (2003) S105.

[74] Y. Koide, M. Liao, and J. Alvarez, Diam. Relat. Mater., 15 (2006) 1962.

[75] M. Stallhofer, M. Seifert, M. V. Hauf, G. Abstreiter, M. Stutzmann, J. A. Garrido, and A. W. Holleitner, Appl. Phys. Lett., 97 (2010) 111107.

[76] Y. Sumikawa, T. Banno, K. Kobayashi, Y. Itoh, H. Umezawa, and H. Kawarada, Appl. Phys. Lett., 85, 139 (2004).

[77] J. Čermák, A. Kromka, and B. Rezek, Phys. Stat. Sol. (a), 205 (2008) 2136.

[78] B. Rezek, T. Mates, J. Stuchlík, J. Kočka, and A. Stemmer, Appl. Phys. Lett., 83 (2003) 1764.

[79] E. Verveniotis, J. Čermák, A. Kromka, and B. Rezek, Phys. Stat. Sol. (b), 246 (2009) 2798.

[80] E. Verveniotis, J. Čermák, A. Kromka, M. Ledinský, Z. Remeš and B. Rezek, Phys. Stat. Sol. (a) 207 (2010) 2040.

[81] E. Verveniotis, A. Kromka, M. Ledinský and B. Rezek, Diamond Relat. Mater., 24 (2011) 39.

[82] P. Fojtik, K. Dohnalová, T. Mates, J. Stuchlík, I. Gregora, J. Chval, A. Fejfar, J. Kočka and I. Pelant, Phil. Mag. B 82 (2002) 1785.

[83] B. Rezek, E. Šípek, M. Ledinský, P. Krejza , J. Stuchlík and J. Kočka, J. Non-Cryst. Solids 354 (2008) 2305.

[84] B. Rezek, E. Šípek, M. Ledinský, J. Stuchlík, A. Vetushka and J. Kočka, Nanotechnology 20 (2009) 045302.

[85] L. de Broglie, Recherches sur la théorie des quanta, PhD Thesis, Sorbonne University (1924).

[86] Y. Zhu, H. Inada, K. Nakamura and J. Wall, Nature Mater., 8 (2009) 808.

[87] J. Goldstein, D. E. Newbury, D. C. Joy, C. E. Lyman, P. Echlin, E. Lifshin, L. Sawyer and J. R. Michael, Scanning Electron Microscopy and X-Ray Microanalysis, Springer (2003), ISBN 978-0-3064-7292-3.

[88] J. B. Cui, J. Ristein, M. Stammler, K. Janischowsky, G. Kleber and L. Ley, Diamond Relat. Mater., 9 (2000) 1143.

[89] M. Park, W. B. Choi, S. K. Streiffer, J. J. Hren, and J. J. Cuomo, Appl. Phys. Lett., 72 (1998) 2580.

[90] Y. Sugimoto, P. Pou, O. Custance, P. Jelinek, M. Abe, R. Perez and S. Morita, Science, 322 (2008) 413.

[91] G. Binning and H. Rohrer, Surf. Sci., 126 (1983) 236.

[92] M. Nonnenmacher, M. P. O'Boyle, and H. K. Wickramasinghe, Appl. Phys. Lett., 58 (1991) 2921.

[93] B. Rezek, J. Čermák and A. Kromka, Int'l patent No. WO2009/10602209.

[94] B. Rezek, E.Šípek, J. Stuchlík, J. Kočka, Czech Patent No. 301824.

[95] E. Verveniotis, B. Rezek, E. Šípek, J. Stuchlík and J. Kočka, Thin Solid Films, 518 (2010) 5965.

[96] E. Verveniotis, B. Rezek, E. Šípek, J. Stuchlik and J. Kočka, Nanoscale Res. Lett., 6 (2011) 145.

[97] Y. Sugimoto, P. Pou, M. Abe, P. Jelinek, R. Pérez, S. Morita and Ó. Custance, Nature, 443 (2007) 64.

[98] E. Verveniotis, A. Kromka and B. Rezek, Nanotechnology, to be submitted

[99] E. Verveniotis, E. Šípek, J. Stuchlík, J. Kočka and B. Rezek, J. Non-Crystal. Solids 358 (2012) 2118

[100] Y. G. Chen, M. Ogura, M. Kondo, and H. Okushi, Appl. Phys. Lett.. 85 (2004) 2110

[101] M. Boutchich, J. Alvarez, D. Diouf, P. i Cabarrocas, M. Liao, I. Masataka, Y. Koide and J.-P. Kleider, J. Non-Cryst. Solids, 358 (2012) 2110

[102] H. Kiyota, H. Okushi, K. Okano, Y. Akiba, T. Kurosu, and M. Iida, Appl. Phys. Lett., 61 (1992) 1808

[103] K. Kůsová, O. Cibulka, K. Dohnalová, I. Pelant, J. Valenta, A. Fučíková, K. Žídek, J. Lang, J. Englich, P. Matějka, P. Štěpánek and S. Bakardjieva, ACS Nano, 4 (2010) 4495.

[104] V. Petráková, A. J. Taylor, I. Kratochvílová, F. Fendrych, J. Vacík, J. Kučka, J. Štursa, P. Cígler, M. Ledvina, A. Fišerová, P. Kneppo and M. Nesládek, Adv. Funct. Mater. 22 (2012) 812

[105] T. Izak, O. Babchenko, M. Varga, S. Potocky and A. Kromka, Phys. Stat. Sol. (b), 249 (2007) 2600

Further extensive references in the enclosed articles

About the Author

Curriculum Vitae

Personal information

Name:	Elisseos Verveniotis
Date of birth:	October 24th 1981
Place of Birth:	Athens, Greece
Nationality:	Hellenic
Email:	verven@fzu.cz

Education

2008-2012	Doctoral studies in the Faculty of Mathematics and Physics, Charles University in Prague, Czech Republic. Study branch: Physics of Nanostructures. PhD Thesis topic: Structuring and study of electronic and chemical properties of semiconductor surfaces.
July 2008	Graduated from the School of Electronic engineering University of Wales, Bangor, United Kingdom. Master of Science (M.Sc.) in Nanotechnology and Microfabrication. Master's Thesis topic: Fabrication of sub-100 nm electrodes for organic electronics.
September 2006	Graduated from the School of Technological Applications, Technological Educational Institute (T.E.I.) of Larissa, Greece. Bachelor of engineering (B.Eng.) in Informatics and Telecommunications technology. Bachelor's Thesis topic: Hyper-Threading technology and its applications.

Research interests

SPM and its advanced modes of operation
Hybrid semiconductor electronics involving diamond
Electronic properties of dielectric materials

Languages

Greek, English, Czech, German (passive)

List of publications and conference contributions

Peer-reviewed scientific journals

1. **E. Verveniotis**, J. Čermák, A. Kromka and B. Rezek
   "AFM induced electrostatic charging of nanocrystalline diamond on silicon"
   Physica Status Solidi (b) 246, (2009), 2798. doi:10.1002/pssb.200982305

2. **E. Verveniotis**, J. Čermák, A. Kromka and B. Rezek
   "Local Electrostatic Charging of Semiconductor Thin Films"
   Proc. of the 17th Annual Conference of Doctoral Students - WDS, F-13, pp. 213–217, 2008, ISBN 978-80-7378-103-3

3. **E. Verveniotis**, J. Čermák, A. Kromka and B. Rezek
   "AFM induced electrostatic charging of nanocrystalline diamond on silicon"
   Proc. of DINAS 2009 workshop, 5.-7.10. 2009, Prague, Czech Republic, pp. 83, 2009, ISBN 978-80-254-5782-5

4. **E. Verveniotis**, B. Rezek, E. Šípek, J. Stuchlík and J. Kočka
   "Role of current profiles and AFM probes in electric crystallization of amorphous silicon"
   Thin Solid Films, 518 (2010) 5965, doi:10.1016/j.tsf.2010.05.107

5. **E. Verveniotis**, J. Čermák , A. Kromka, M. Ledinský, Z. Remeš and B. Rezek
   "Differences in local electrostatic charging of sub-100 nm nanocrystalline diamond on silicon"
   Physica Status Solidi (a), 207 (2010) 2040, doi:10.1002/pssa.201000014

6. **E. Verveniotis**, J. Čermák , A. Kromka, M. Ledinský and B. Rezek
   "Electrostatic Charging Differences in Ultrathin Nanocrystalline Diamond
   Proc. of the 18th Annual Conference of Doctoral Students - WDS, F-13, pp. 86–90, 2010, ISBN 978-80-7378-141-5

7. **E. Verveniotis**, A. Kromka, M. Ledinský, J. Čermák and B. Rezek
   "Guided assembly of nanoparticles on electrostatically charged nanocrystalline diamond thin films"
   Nanoscale Res. Lett. 6 (2011) 144, doi:10.1186/1556-276X-6-144

8. **E. Verveniotis**, B. Rezek, E. Šípek, J. Stuchlik, M. Ledinský and J. Kočka
   "Impact of AFM-induced nano-pits in a-Si:H films on silicon crystal growth"
   Nanoscale Res. Lett. 6 (2011) 145, doi:10.1186/1556-276X-6-145

9. **E. Verveniotis**, A. Kromka, M. Ledinský and B. Rezek
   "Electrostatic assembly of alumina nanoparticles on nanocrystalline diamond films"
   Proc. of the 19th Annual Conference of Doctoral Students - WDS, F-13, pp. 93–98, 2011, ISBN 978-80-7378-186-6

10. **E. Verveniotis**, A. Kromka, M. Ledinský and B. Rezek:
"How nanocrystalline diamond films become charged in nanoscale"
Diam. Relat. Mater. 24 (2012) 39-43, doi:10.1016/j.diamond.2011.10.002

11. **E. Verveniotis**, E. Šípek, J. Stuchlík, J. Kočka and B. Rezek:
"Generating ordered Si nanocrystals via atomic force microscopy"
J. Non-Crystal. Solids 358 (2012) 2118 doi:10.1016/j.jnoncrysol.2011.12.018

12. O. Babchenko, **E. Verveniotis**, K. Hruska, M. Ledinsky, A. Kromka and B. Rezek:
"Direct growth of sub-micron diamond structures"
Vacuum 86 (2012) 693-695, doi: 10.1016/j.vacuum.2011.08.011

13. T.Izak, A. Kromka, O. Babchenko, M. Ledinsky, K. Hruska and **E. Verveniotis**
"Comparative study on dry etching of polycrystalline diamond thin films"
Vacuum 86 (2012) 799-802, doi: 10.1016/j.vacuum.2011.07.023

14. **E. Verveniotis**, A. Kromka and B. Rezek
"Charged micro-patterns on nanocrystalline diamond are well defined by electrical current application"
Acta Universitatis Carolinae. Mathematica et Physica 2013, accepted

15. **E. Verveniotis**, A. Kromka and B. Rezek
"Persistent microscopic charging of oxidized nanocrystalline diamond by constant currents in atomic force microscope"
Nanotechnology, to be submitted

Conference contributions

1. **E. Verveniotis**, J. Čermák, A. Kromka and B. Rezek
"AFM induced electrostatic charging of nanocrystalline diamond on silicon"
Poster presentation at IWEPNM 2009, 7-14.3.2009, Kirchberg, Austria

2. **E. Verveniotis**, J. Čermák, A. Kromka and B. Rezek
"Local Electrostatic Charging of Semiconductor Thin Films"
Oral presentation at WDS 2009, 2–5.6.2009, Prague, Czech Republic

3. **E. Verveniotis**, B. Rezek, E. Šípek, J. Stuchlík and J. Kočka
"Nanocrystallization of amorphous silicon by conductive AFM probes"
Poster presentation at ICANS23, 23-28.8.2009, Utrecht, Netherlands

4. **E. Verveniotis**, J. Čermák, A. Kromka and B. Rezek
"AFM induced electrostatic charging of nanocrystalline diamond on silicon"
Oral presentation for DINAS 2009 workshop, 5.-7.10.2009, Prague, Czech Republic.

5. **E. Verveniotis**, J. Čermák, A. Kromka and B. Rezek
   "Local Electrostatic Charging of Semiconductor Thin Films"
   Oral presentation for the bilateral project between ASCR and Uppsala University, Fall 2009

6. **E. Verveniotis**, J. Čermák , A. Kromka, M. Ledinský, Z. Remeš and B. Rezek
   "Differences in local electrostatic charging of sub-100 nm nanocrystalline diamond on silicon"
   Poster presentation at SBDD XV, 22-24.2.2010, Hasselt, Belgium

7. **E. Verveniotis**, J. Čermák , A. Kromka, M. Ledinský and B. Rezek
   "Electrostatic Charging Differences in Ultrathin Nanocrystalline Diamond"
   Oral presentation at WDS 2010, 1–4.6.2010, Prague, Czech Republic

8. **E. Verveniotis**, B. Rezek, E. Šípek, J. Stuchlik, M. Ledinský and J. Kočka
   "Impact of AFM-induced nano-pits in a-Si:H films on silicon crystal growth"
   Poster presentation at E-MRS Fall, 13-17.9.2010, Warsaw, Poland

9. **E. Verveniotis**, A. Kromka, M. Ledinský, J. Čermák and B. Rezek
   "Electronic and material contributions to local electrostatic charging of nanocrystalline diamond films on silicon"
   Oral presentation at E-MRS Fall, 13-17.9.2010, Warsaw, Poland

10. O. Babchenko, **E. Verveniotis**, K. Hruska, M. Ledinsky, A. Kromka and B. Rezek:
    "Direct growth of sub-micron diamond structures"
    Poster presentation at JVC 13, 20-24.6.2010, Štrbské Pleso, Slovakia

11. T.Izak, A. Kromka, O. Babchenko, M. Ledinsky, K. Hruska and **E. Verveniotis**
    "Comparative study on dry etching of polycrystalline diamond thin films in different plasma systems"
    Poster presentation at JVC 13, 20-24.6.2010, Štrbské Pleso, Slovakia

12. B. Rezek, O. Babchenko, A. Vetushka, **E. Verveniotis**, M. Ledinský and A. Kromka:
    "Surface related 2D conductivity of NCD in-plane nanowires"
    Poster presentation at IWEPNM 27.2-4.3.2011, Kirchberg, Austria

13. B. Rezek, **E. Verveniotis** and A. Kromka
    "How charge-patterned nanocrystalline diamond orders nanoparticles"
    Oral presentation at NDNC 2011, 16–20.5.2011, Matsue, Japan

14. **E. Verveniotis**, J. Čermák , A. Kromka, M. Ledinský and B. Rezek:
    "Electrostatically-Guided Assembly of Alumina Nanoparticles on Ultra-Thin Nanocrystalline Diamond Films"
    Oral presentation at WDS 2011, 31.5–3.6.2011, Prague, Czech Republic

15. B. Rezek, **E. Verveniotis**, E. Šípek, J. Stuchlik, M. Ledinský and J. Kočka
"Generating Ordered Si Nanocrystals via Atomic Force Microscopy"
Oral presentation at ICANS24, 21-26.8.2011, Nara, Japan

16. B. Rezek, O. Babchenko, A. Vetushka, **E. Verveniotis**, M. Ledinský and A. Kromka:
"Growth and surface conductivity of diamond in-plane nanowires"
Poster presentation at Diamond2011, 4-8.9.2011, Garmish-Partenkirchen, Germany

17. **E. Verveniotis**, A. Kromka and B. Rezek
"Microscopic correlation of material properties and electrostatic charging in ultra-thin nanocrystalline diamond films"
Poster presentation at Diamond2011, 4-8.9.2011, Garmish-Partenkirchen, Germany

18. **E. Verveniotis**, A. Kromka and B. Rezek
"Localized charging of nanocrystalline diamond by electrical current application"
Oral presentation at WDS 2012, 29.5–1.6.2012, Prague, Czech Republic

19. **E. Verveniotis**, A. Kromka and B. Rezek,
"Nanocrystalline diamond growth on a-Si:H"
Oral presentation at IUMRS-ICEM 2012, 23-28.9.2012, Yokohama, Japan